792

A Thesis Entitled

ABSORPTION SPECTRA OF ATOMIC OXYGEN IN THE VACUUM ULTRAVIOLET

by

MALCOLM DAVID DREW

Submitted for the degree of
Doctor of Philosophy
of the University of London

Department of Physics
Imperial College
London S.W.7.

September 1978

CONTENTS

CHAPTER I INTRODUCTION AND REVIEW OF EXISTING DATA

PART I - PHOTOGRAPHY OF THE ABSORPTION SPECTRUM OF ATOMIC OXYGEN BETWEEN 600 Å AND 350 Å AND THE NEW ABSORPTION SERIES

CHAPTER II EXPERIMENTAL

CHAPTER III NEW ABSORPTION SERIES OF ATOMIC OXYGEN IN THE VACUUM ULTRAVIOLET

CONTENTS (Continued)

Page

CHAPTER IV CALCULATION OF THE $1s^2\,2s2p^4(^4P)np\ ^3D^o$, $^3S^o$ and $^3P^o$ TERMS OF ATOMIC OXYGEN

CHAPTER V THE RADIOFREQUENCY DISCHARGE IN NITROGEN

PART II MEASUREMENTS OF THE RELATIVE PHOTOABSORPTION CROSS SECTION OF ATOMIC OXYGEN IN THE EXTREME VACUUM ULTRAVIOLET

CHAPTER VI EXPERIMENTAL

CHAPTER VII ATOMIC OXYGEN PHOTOABSORPTION CROSS SECTION RESULTS

CONTENTS (Continued)

ABSTRACT

Apparatus is described which was constructed to investigate the absorption spectra of atomic oxygen at wavelengths less than 600 Å. Atomic oxygen was created by running a radiofrequency discharge through a molecular sample of the gas contained in a windowless system. The background light source employed was the Balloffet, Romand and Vodar continuum source.

The absorption spectrum of atomic oxygen was photographed with the Kodak 101-01 emulsion from 600 Å to 350 Å. Three new absorption series from the atomic oxygen ground state $2p^4\ {}^3P$, with upper states $2s\ 2p^4({}^4P)np\ {}^3D^o$, $({}^4P)np\ {}^3S^o$ and $({}^4P)np\ {}^3P^o$, all converging to the ${}^4P$ term of the ion O^+ at 435.3 Å, were observed and identified. The theoretical separations of the ${}^3D^o$, ${}^3S^o$ and ${}^3P^o$ upper state terms were calculated, for several values of n, by the Hartree Fock self-consistent field technique. Results of these computations were employed in the classification of the observed series.

The radiofrequency discharge was also found to create atomic nitrogen and the absorption spectrum was photographed from 600 Å to 350 Å. No new absorption series could be positively identified.

The relative continuous photoabsorption cross section curve of atomic oxygen from 830 Å to 430 Å was obtained with the same apparatus by photographic photometry. These measurements were put onto an absolute scale by comparison with existing absolute cross section data at a number of wavelength values from 830 Å to 450 Å.

ACKNOWLEDGEMENTS

I wish to thank Professor W.R.S. Garton, FRS, for the use of the facilities of his laboratory and for his supervision during the course of the project.

I am indebted to Dr. R.C.M. Learner for his constant advice throughout and for reading the manuscript of this thesis.

Thanks are also due to Dr. J.P. Connerade for providing me with the Froese Fischer multiconfiguration Hartree-Fock computer program and for many useful discussions.

The assistance of the glassblower and the staff of the Workshops at Imperial College in the construction of the apparatus for the experiments is acknowledged.

I am grateful to Mrs. Wright for the excellent typing of this thesis.

Finally I wish to thank the Royal Society for the financial support of the project.

CHAPTER I

INTRODUCTION AND REVIEW OF EXISTING DATA

1.1 Introduction

The photoabsorption properties of atomic oxygen are of great importance in the physics of the upper atmosphere. Atomic oxygen is a major constituent in the ionosphere above 160 kms from the earth's surface. Solar radiation of photon energy higher than its first ionization potential (corresponding to wavelengths of less than 910 Å) photoionizes the atoms either directly or through an autoionization channel. Photoionization of atomic oxygen is well established as one of the most important mechanisms for the production of energetic electrons and ions in the upper atmosphere.

The cross section for photoionization can vary rapidly with wavelength near transitions for which the upper level is allowed to autoionize. If such transitions in atomic oxygen should coincide with solar emission they could have a strong influence on the rate of electron and ion production in the upper atmosphere. The observation of autoionizing transitions in the absorption spectrum, and the measurement of the photoionization cross section of atomic oxygen below 910 Å are therefore of considerable interest in the field of atmospheric physics as well as steps towards an improved understanding of the atom's structure.

By 1973, the wavelength region down to 600 Å had been quite well explored (see next section) but very little data had been obtained at lower wavelengths. The purpose of this investigation was to extend the region of observation to wavelengths which had been unaccessible hitherto i.e. below 600 Å. It was hoped in particular to observe the excitation of an inner subshell 2s electron in series converging to excited states of O II. In the experiment which will be described in Part I of this thesis the absorption spectrum of atomic oxygen has been photographed for the first time between 600 Å and 350 Å. Three new series were observed and identified as transitions from the O I ground state $1s^2\ 2s^2\ 2p^4\ {}^3P_{2,1,0}$

to the upper states $2s2p^4(^4P)np\ {}^3D^o$

$^3S^o$

$^3P^o$ respectively.

i.e. transitions involving an inner subshell 2s electron. These series converge to the $2s2p^4\ {}^4P$ term of O II at 435 Å.

New measurements of the relative photoabsorption cross section of atomic oxygen from 650 Å to 430 Å have also been obtained and these will be reported in Part II of the thesis. In the experiments a continuum light source was used and the technique of photographic photometry employed to determine the intensity ratios. The wavelength region from 830 Å to 430 Å was recorded on the photographic plates so that absolute values could be ascribed to the data by comparison with the absolute cross section values obtained at a number of wavelengths above 650 Å in three previous measurements (1,2,3). These three experiments will be included in a brief review of the photoabsorption data existing prior to this investigation on atomic oxygen below 910 Å which is given in the next section.

1.2 Review of existing data

An extensive investigation of the absorption spectrum of atomic oxygen from 1050 Å to 600 Å was reported by Huffman, Larrabee and Tanaka in 1966 (4). They photographed and identified nine allowed Rydberg series from the ground state converging to the three lowest O II terms

$^4S^o_{3/2}$ at 910.4 Å

$^2D_{5/2,3/2}$ at 731.8 Å

and $^2P^o_{3/2,1/2}$ at 665.3 Å

The series are summarised in Table 1.2.1. In the experiment, atomic oxygen was created in a microwave discharge through helium containing a trace (0.25%) of molecular oxygen. The Hopfield helium continuum discharge served as the background light source (lower limit 600 Å).

This apparatus was also used by the same authors in 1967(5) to observe and classify eight series with metastable O I $^1D_2$ or $^1S_0$ as the lower state. These series are summarised in Table 1.2.2.

The first absolute cross section work on atomic oxygen below 910 Å was reported by Cairns and Samson in 1965(1). They obtained the photoabsorption cross section at 22 wavelengths in the 900 Å to 500 Å wavelength region by using a microwave discharge through a gaseous mixture consisting of 80% helium and 20% molecular oxygen. Their results are discussed in detail in Chapter VII but briefly they obtained values between 4.7 and 17.3 Megabarns (1 Mbn = 10^{-18} cm^2) with an estimated accuracy of ± 30%.

In 1968, Comes, Speier and Elzer(2) reported values for the photoionization cross section at about 30 wavelengths between 910 Å and 450 Å with an estimated uncertainty of ± 10%. Most of these were in the range 2 to 10 Mbns (see Chapter VII). The most recent absolute cross section data has been obtained by Kohl, Lafyatis, Palenius and Parkinson(3). Atomic oxygen was created by heating a mixture consisting of 99% neon and 1% molecular oxygen in a shocktube. Values at five wavelengths between 900 Å and 760 Å were reported for the photoabsorption cross section all between 4 and 5.5 Mbns. The estimated uncertainty was ± 7%.

The relative photoionization cross section for atomic oxygen was measured from 920 Å to 650 Å by Dehmer, Berkowitz and Chupka in 1973(6). The sample was produced by applying a 3 kV 60 Hz a.c. discharge through a mixture of 75% molecular oxygen and 25% argon. All the terms above the first ionization limit were observed to autoionize including the $^3P^o$ terms below the $^2D^o$ limit for which the process is Russell-Saunders forbidden. Indeed the two transitions for which the photoionization

TABLE 1.2.1(1)

A Summary of the Atomic Oxygen Series 910 Å to 650 Å

O II Level	Term value from O I ground state(2) (cm^{-1})	Convergence limit (Å)	O I Series(3)
$2s^2\ 2p^3(^4S^o_{3/2})$	109837.03	910.440	$(^4S^o)ns\ ^3S^o$ $(^4S^o)nd\ ^3D^o$
$2s^2\ 2p^3(^2D^o_{5/2})$	136645.4	731.821	$(^2D^o)ns'\ ^3D^o$
$(^2D^o_{3/2})$	136666.4	731.709	$(^2D^o)nd'\ ^3S^o$ $(^2D^o)nd'\ ^3P^o$ $(^2D^o)nd'\ ^3D^o$
$2s^2\ 2p^3(^2P^o_{3/2})$	150303.9	665.319	$(^2P^o)ns''\ ^3P^o$
$(^2P^o_{1/2})$	150305.4	665.312	$(^2P^o)nd''\ ^3P^o$ $(^2P^o)nd''\ ^3D^o$
$2s\ 2p^4$			$2s\ 2p^5\ ^3P^o$

1. From reference 4.
2. Lower state is the O I ground state $1s^2\ 2s^2\ 2p^4\ ^3P_2$.
3. The single and double prime on the running electron designates terms converging to O II ^2D and ^2P respectively.

TABLE 1.2.2 (1)

A Summary of the Atomic Oxygen Rydberg Series with $2p^4\ {}^1D_2$ or $2p^4\ {}^1S_0$ Metastable States as the Lower Level

Lower State	O II Limit	Convergence limit (cm^{-1})	Convergence limit (Å)	O I Series
O I($^1D_2$)	O II($^2D^o_{5/2}$)	120777.5	827.969	$(^2D^o)ns'\ {}^1D^o_2$
O I($^1D_2$)	O II($^2D^o_{3/2}$)	120798.5	827.825	$(^2D^o)ns'\ {}^3D^o_2$
				$(^2D^o)nd'\ {}^1F^o_3$
				$(^2D^o)nd'\ {}^1D^o_2$
				$(^2D^o)nd'\ {}^1P^o_1$
O I($^1D_2$)	O II($^2P^o_{3/2}$)	134436.0	743.848	$(^2P^o)ns''\ {}^1P^o_1$
O I($^1D_2$)	O II($^2P^o_{1/2}$)	134437.5	743.840	$(^2P^o)nd''\ {}^1F^o_3$(2)
				$(^2P^o)nd''\ {}^1D^o_2$
				$(^2P^o)nd''\ {}^1P^o_1$(2)
O I($^1S_0$)	O II($^2P^o_{3/2}$)	116511.3	858.286	$(^2P^o)ns''\ {}^1P^o_1$(2)
O I($^1S_0$)	O II($^2P^o_{1/2}$)	116512.8	858.275	$(^2P^o)nd''\ {}^1P^o_1$

1. From reference 5.
2. Not observed in reference 5.

cross section was 1st and 2nd highest - ground state to $2s2p^5\ {}^3P^o_{2,1,0}$ and ground state to $2s2p^3(^2P^o)3s''\ {}^3P^o_{2,1,0}$ should both be stable. These as well as the other autoionization forbidden lines were observed in emission by Huffman, Larrabee and Tanaka(4).

The competition of autoionization and emission processes was also reported for the upper states $2s^22p^3(^2D^o)3d'\ {}^3P^o$, $2s^22p^3(^2P^o)3s''\ {}^3P^o$ and $2s2p^5\ {}^3P^o$ by Samson and Petrosky in 1974(7). The emission spectrum of atomic oxygen was first produced by adding a trace (1/2%) of molecular oxygen to a dc helium glow discharge. Secondly, atomic oxygen produced in a microwave discharge was photoionized with a helium lamp and the photoelectrons energy analyzed.

A common feature of the experiments which have been described in this section is that an inert gas, usually helium, was added to the oxygen in the absorption cell. Its purpose was to inhibit the recombination of oxygen atoms. This technique is not applicable for spectroscopy at wavelengths shorter than the He II $^2S_{1/2}$ limit at 504 Å as the helium is opaque. A sample of pure atomic oxygen is therefore required and this was the most serious of the problems encountered in the experiments below 504 Å described in this thesis.

PART I - PHOTOGRAPHY OF THE ABSORPTION SPECTRUM OF ATOMIC OXYGEN BETWEEN 600 AND 350 Å AND THE NEW ABSORPTION SERIES

CHAPTER II

EXPERIMENTAL

2.1 Introduction

The apparatus designed to record photographically the absorption spectrum of a gas or vapour may be divided into the following components:

a) a background light source yielding an emission continuum in the spectral region of interest.

b) a means of introducing the absorbant into the light path; a process which entails firstly, the creation of the sample and secondly, its containment.

c) a dispersing instrument and photographic emulsion suitable for radiation in the spectral range concerned.

All three requirements have been met in order to obtain the absorption spectrum of atomic oxygen at wavelengths greater than 600 Å, but several technical problems have, in the past, hindered investigations at shorter wavelengths.

In the following sections of this chapter, the methods used to extend the region of observation below 600 Å are described in detail.

2.2 The discharge tubes

The creation of a pure sample of atomic oxygen of sufficient integrated number density was the most difficult problem in this experiment. The integrated number density required for unit optical depth for a gas of cross section 5 Mbns is 2.10^{17} atoms/cm^2. For a perfect gas, in thermal equilibrium, at room temperature contained in an absorption tube 100 cms long this corresponds to a partial pressure of 0.062 Torr. None of the techniques employed in the previous experiments mentioned in

Chapter I were applicable for work below 504 Å because of their use of helium.

The photoabsorption cross section of molecular oxygen is both non-uniform and higher than that of the atom in this wavelength region. It varies between 20 and 30 Mbns(12). It is particularly important if the atomic sample is to be created from the molecular gas in a rapid flow discharge to achieve a high degree of dissociation so that the integrated number density of the atom is at least two orders of magnitude greater than the molecule. If the degree of dissociation is not sufficient, the transmitted intensity will be reduced in regions of high molecular cross section through the exponential factor in the Lambert-Beer formula and molecular absorption bands and continua will degrade the spectrum.

Pure samples of atomic oxygen were created in the experiment by running an electrodeless radiofrequency discharge through molecular oxygen flowing rapidly through a quartz tube. Radiofrequency current was passed through an induction coil consisting of copper tube of outer diameter 6 mm wound loosely around the outside of the absorption cell with a spacing of approximately 5 cms between turns. Cooling water was passed through the induction coil and the discharge tube endplates. The generator of radiofrequency power was a Radyne C155/P power unit. This had a self-oscillating Colpitts-type output circuit using two air-cooled silica enveloped triodes in parallel. The oscillating circuit comprised the induction coil and the tank capacitance which together determined the operating frequency. This was in the range 2 to 7 MHz. Initialisation of the discharge required no special procedures.

Two discharge tubes were tried in the course of the experiment. The first was 30 cms in length, 10 cms in diameter and the second was 100 cms in length, 6 cms in diameter. The integrated number density, at a particular temperature, depends on the product of the pressure of the gas and the path length through the absorbing medium. The atomic oxygen pressure in the 100 cm tube could thus be one third of that in the 30 cm tube to produce an equivalent integrated number density. Better results were obtained with the long tube (filled to a pressure of 100 microns with molecular oxygen before initialisation of the discharge) as will be described in Section 2.7.

Both discharge tubes were quartz and were fitted to the brass endplates with demountable vacuum 'O' ring seals. The endplates are described in detail in Section 2.4. Quartz was chosen as a material for the tubes in preference to pyrex as its high melting point (over 1000 °C) made it more likely to withstand the thermal shock of the discharge forming and because of its lower coefficient of thermal expansion. It was felt that these advantages of using quartz outweighed the disadvantages of its cost and the difficulty in glassblowing. Experience showed that the 30 cm long tube could withstand the radio-frequency discharge for up to 15 minutes before the quartz became red hot. An air blower was used to keep down the temperature of the tubes especially at the ends near the vacuum 'O' rings.

The recombination rate of atomic oxygen was expected to be highest close to the interior surface of the quartz. The diameter of both discharge tubes (10 cms and 6 cms) was therefore made quite large in comparison with previous workers (for example, the tube in reference 4 was 1.3 cms in diameter). This achieved a higher volume to surface area ratio and kept the region of rapid recombination away from the axis along which the beam from the continuum light source passed.

2.3 The containment system

The atmospheric gases have high, non-uniform photoabsorption cross sections below 600 Å. To avoid degradation of the spectrum it was therefore important to maintain all parts of the apparatus away from the discharge tube itself under high vacuum. This made it necessary firstly to place a transparent containment device at both ends of the discharge tube to ensure that recombined oxygen could not reach the rest of the system and secondly to evacuate the continuum source and the spectrograph with diffusion pumps. (The continuum source used for the experiment - see Section 2.5, required high vacuum anyway).

It was not possible to use windows as containment devices in this experiment. Lithium fluoride has a short wavelength transmission limit of 1040 Å and is therefore inapplicable. Metallic or plastic films, a few thousand angstroms thick, are very fragile and would not have withstood contact with the hot discharge. The technique of protecting (or 'buffering') the window from contact with a reactive absorbing medium by using a transparent layer of an inert gas such as helium, cannot be used at wavelengths lower than 504 Å.

The containment problem was solved in this experiment by using a differential pumping section at both ends of the absorption cell. These have the great advantage that no windows or buffer gases are needed. Each differential pumping section consists of a series of vacuum chambers (or 'stages') individually pumped, and separated from their neighbours (or neighbour) by a gas flow impedance consisting of either a thin flange with a small hole in the centre or a flange in which is mounted a small bore tube.

The principle of operation is that if the speed (S_i) of the pump evacuating a particular chamber is much greater than the conductance (C_i) of the 'upstream' impedance device through which gas is entering the chamber, then the pressure (P_i) in the chamber is very much less than that (P_{i-1}) in the 'upstream' stage. This can be seen as follows.

We know that

$$S_i = \frac{Q_i - Q_{i+1}}{P_i} \tag{3.2.1}$$

and $$C_i = \frac{Q_i}{P_{i-1} - P_i} \tag{2.3.2}$$

if $$S_i \gg C_i$$

then $$\frac{Q_i - Q_{i+1}}{P_i} \gg \frac{Q_i}{P_{i-1} - P_i}$$

assuming that $Q_{i+1} > 0$

then $$P_i \ll P_{i-1}$$

and $$Q_i \gg Q_{i+1}$$

In this experiment, the gas pressure in the first stages had to be 1 micron or less to ensure that if the oxygen had recombined by then, the molecular integrated number density in the light beam would be negligible. From equation 2.3.1

if $$Q_i \gg Q_{i+1}$$

then $$S_i = \frac{Q_i}{P_i} = \frac{C_i\,(P_{i-1} - P_i)}{P_i}$$

and $$\frac{P_{i-1}}{P_i} = 1 + \frac{S_i}{C_i} \approx \frac{S_i}{C_i} \tag{2.3.3}$$

i.e. as the pressure in the discharge tube had to be about 100 microns and that in the first stages had to be 1 micron, S_i had to be two orders of magnitude greater than C_i.

In the design of the differential pumping sections, the diameter of the holes or tubes had to strike a balance between the need for optical transmission and ease of alignment, favouring a large diameter, and for high gaseous impedance favouring a small one. Long tubes as the first impedances between the absorption cell and the first stages were not used in case the oxygen flowing through them (at slightly less than cell pressure) had recombined. A small hole as the first impedance was therefore preferred and the minimum diameter for reasonable optical transmission was judged to be about 2 mm. The 2 mm hole was treated as a 'tube' of length equal to its diameter in the calculation of its conductance.

The flow of gases through tubes is divided into three well known regions. These are characterized by a dimensionless parameter, known as the Knudsen number, defined as the ratio of the mean free path λ of the gas to the diameter D of the tube. The three regions are

$$\frac{\lambda}{D} < 0.01 \qquad \text{viscous flow}$$

$$\frac{\lambda}{D} > 1.0 \qquad \text{molecular flow}$$

$$0.01 < \frac{\lambda}{D} < 1.0 \qquad \text{transition flow}$$

The mean free path is given approximately by the formula

$$\lambda = \frac{1}{\sqrt{2}\,\pi\, d^2 n} \qquad (2.3.4)$$

where d is the 'effective' diameter of the atom or molecule (any other atom or molecule whose centre is within a distance d will touch it) and n is the number of atoms or molecules per cc. In a discharge tube 100 cms long, the density of oxygen atoms which gives unit optical depth at 600 Å is about 2.10^{15} atoms per cc.

$$\text{Taking} \quad d = 10^{-8} \text{ cms}$$

$$\text{this gives} \quad \lambda = 1.125 \text{ cm.}$$

With an impedance of diameter a few mm, the flow is therefore in the molecular region.

The theory relevant to the flow of gases through orifices and tubes has been reviewed by Del Bianco and Boridy (8), who summarize the literature on the subject. The conductance of a tube C_t in the molecular flow region may be written as the conductance of an orifice C_o times a correction factor K_c (the 'Clausing correction factor') that is

$$C_t = K_c C_o \tag{2.3.5}$$

where $$C_o = 1/4 \pi D^2 (RT/M)^{1/2} \Gamma_k \tag{2.3.6}$$

and $$\Gamma_k = (2\pi)^{-1/2} = 0.399$$

Here, R is the gas constant, T the temperature and M the atomic or molecular weight of the gas respectively. The Clausing correction factor depends on the ratio of the length of the tube to its diameter L/D. Del Bianco and Boridy list the values of K_c for several values of the ratio L/D and these are reproduced in Table 2.3.1. From equations (2.3.5) and (2.3.6), the conductance of a 'tube' of diameter 2 mm and length 2 mm is given by (T = 300 ^{o}K, M = 16)

$$C_t^1 = 2.52 \quad 10^{-1} \ \ell \ \text{sec}^{-1}$$

The performance of a differential pumping section depends not only on the conductance of the impedance devices but also on the speed of the vacuum pumps. The Edwards models EM2 and EO2 diffusion pumps have a high pumping speed (150 ℓ sec^{-1} for molecular oxygen) and are reasonably

TABLE 2.3.1

Clausing Correction Factors(1) K_c(2) (Molecular flow)

L/D	0.1	0.2	0.5	1.0	2.0	5.0	10	20	30	40	50
K_c	0.91	0.83	0.67	0.51	0.36	0.20	0.11	0.061	0.042	0.032	0.026

1. From reference 8.
2. K_c = (Conductance of tube of length L and diameter D)/ Conductance of orifice of diameter D).

compact and inexpensive. With a liquid nitrogen trap and a short length of connecting piping placed in series the effective pumping speed is reduced to about $40\ \ell\ \sec^{-1}$.

From Equation (2.3.3) with $S_i = 40\ \ell\ \sec^{-1}$ and $C_i = 2.52\ 10^{-1}\ \ell\ \sec^{-1}$

$$\frac{P_{i-1}}{P_i} = 1.6\ \ 10^2$$

i.e. a reduction of two orders of magnitude in pressure. The combination of a 2 mm hole and the $40\ \ell\ \sec^{-1}$ effective pumping speed is therefore calculated to perform as required for the first stages.

It can be seen from Table 2.3.1 that the conductance of a long tube can be very much less than an orifice of equal diameter in the molecular flow region. If $L/D = 10$, for example, $K_c = 0.11$ and the conductance of the tube is an order of magnitude less than the orifice. Since the pressure in the first stage was only about 1 micron a tube could be used as the second impedance (between the first and second stages) without fear that molecular oxygen of sufficient integrated number density to cause degradation of the spectrum would enter the light path.

Tubes of diameter 5 mm and length 50 mm were used as the second impedances. For these dimensions

$$C_t^2 = 3.51\ \ 10^{-1}\ \ell\ \sec^{-1} (T = 300\ {}^{o}K,\ \ M = 16)$$

and for $S_2 = 40\ \ell\ \sec^{-1}$.

$$\frac{P_1}{P_2} = 1.15\ \ 10^2$$

so if $$\frac{P_o}{P_1} = 1.6\ \ 10^2$$

$$\frac{P_o}{P_2} = 1.82\ \ 10^4$$

and if $$P_o = 10^{-1}\ \text{mm}$$

$$P_2 = 5.46\ \ 10^{-6}\ \text{mm}$$

This was perfectly adequate as the final pressure for the continuum light source and the spectrograph.

Two differential pumping sections were constructed, one for each end of the discharge tube. These can be seen on Plates 2.3.1, 2.3.2 and 2.3.3, which are photographs of the apparatus. Note that the length of pipework connecting the diffusion pumps to the stages (and the length of the chambers along the axis of the apparatus) was kept to a minimum. No butterfly valves were used in series with the pumps for the first stages. These would have reduced the effective pumping speed by 50%. Edwards model EM2's, containing mercury as the pumping fluid, were used for the first stages since these continue to operate at maximum speed at a slightly higher pressure than the E02 which is charged with oil. This was important for the first stages where the pressure (1 mn) is getting near that at which diffusion pumps cease to be effective.

For the second stage at the source end an E02 was used charged with Santovac 5 oil. This is a polyphenyl ether fluid of very low vapour pressure and so a liquid nitrogen trap was not required. A butterfly valve could therefore be inserted in series without reducing the effective pumping speed below 40 ℓ sec^{-1}. A sliding airtight valve was incorporated to cover the tube between the first and the second stages at the source end. This allowed air to be admitted into the B.R.V. source chamber for changing the electrodes.

The differential pumping section at the spectrograph end consisted of three stages. This is illustrated schematically in Figure 2.3.1. The spectrograph slit served as the gas flow impedance between the second and third stages. As will be described in more detail in Section 2.6, the commercial Jobin Yvon vacuum spectrograph was designed with a separately pumped chamber, in front of the slit, with electrodes for spectrochemical analysis. The diffusion pump serving this chamber was, unfortunately,

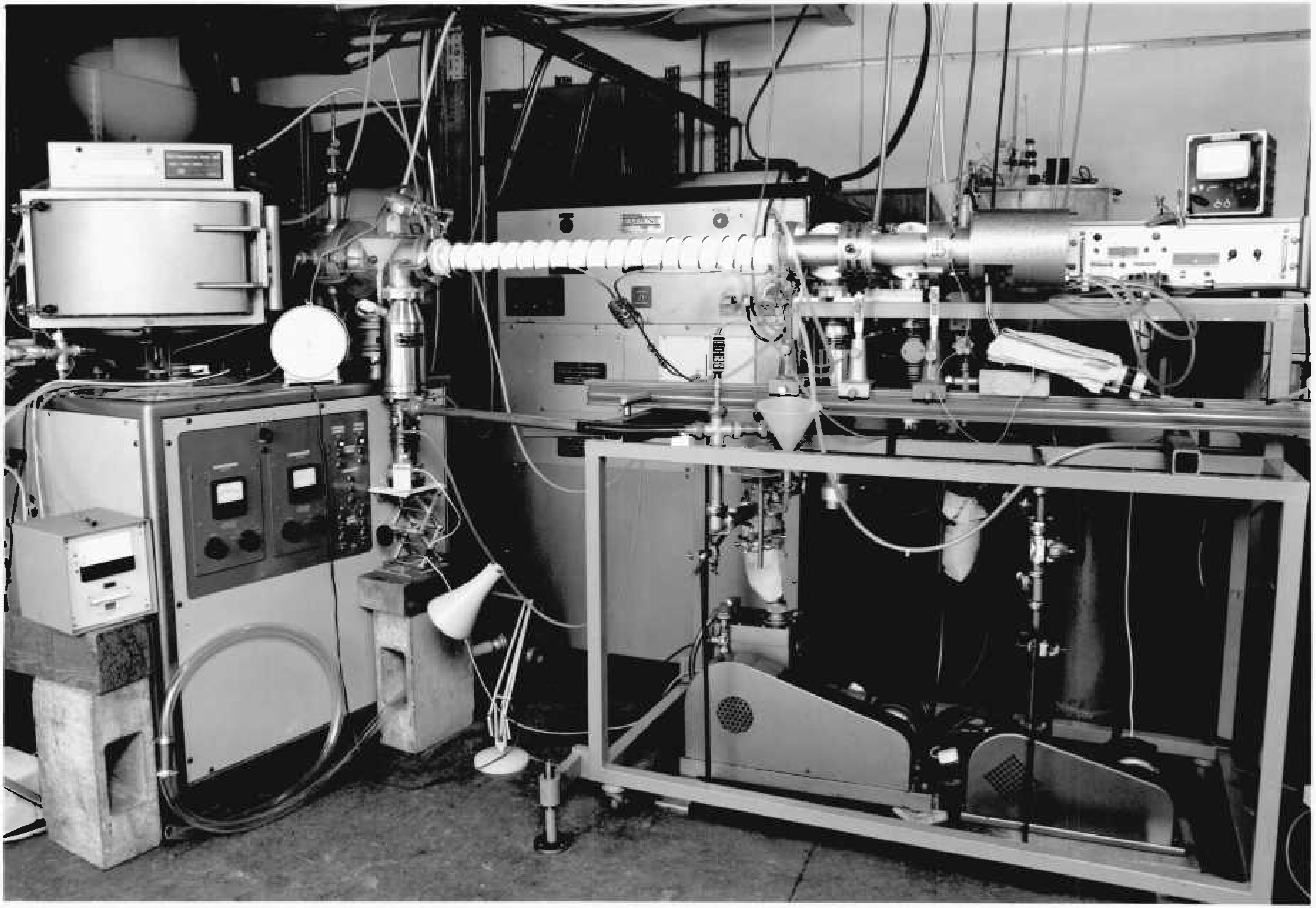

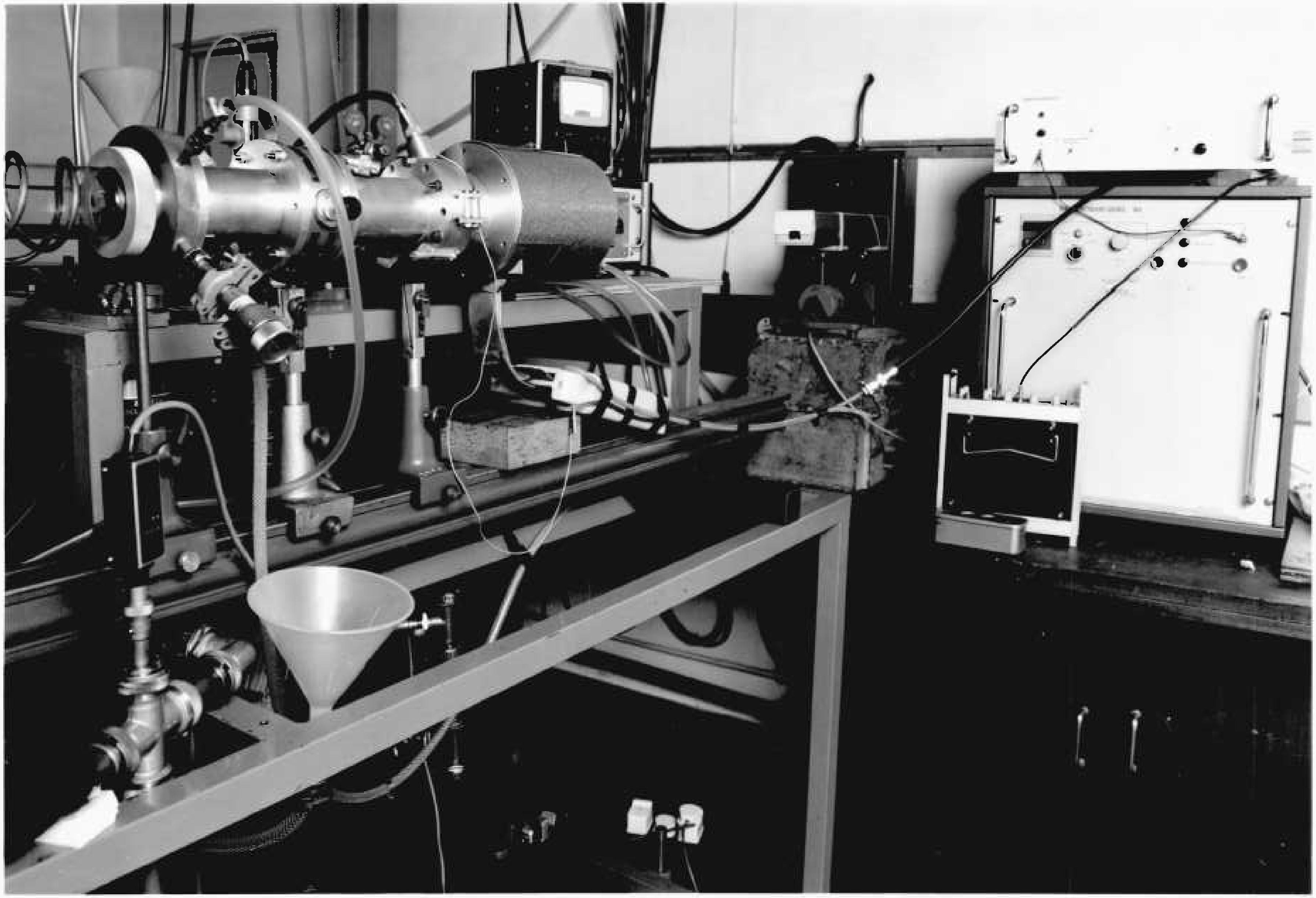


SPECTROGRAPHE SOUS VIDE
IONIVAC
CGR
IONIVAC
CGR
PP1
PP2
PS1
PS2
SPEEDI
MERCURY

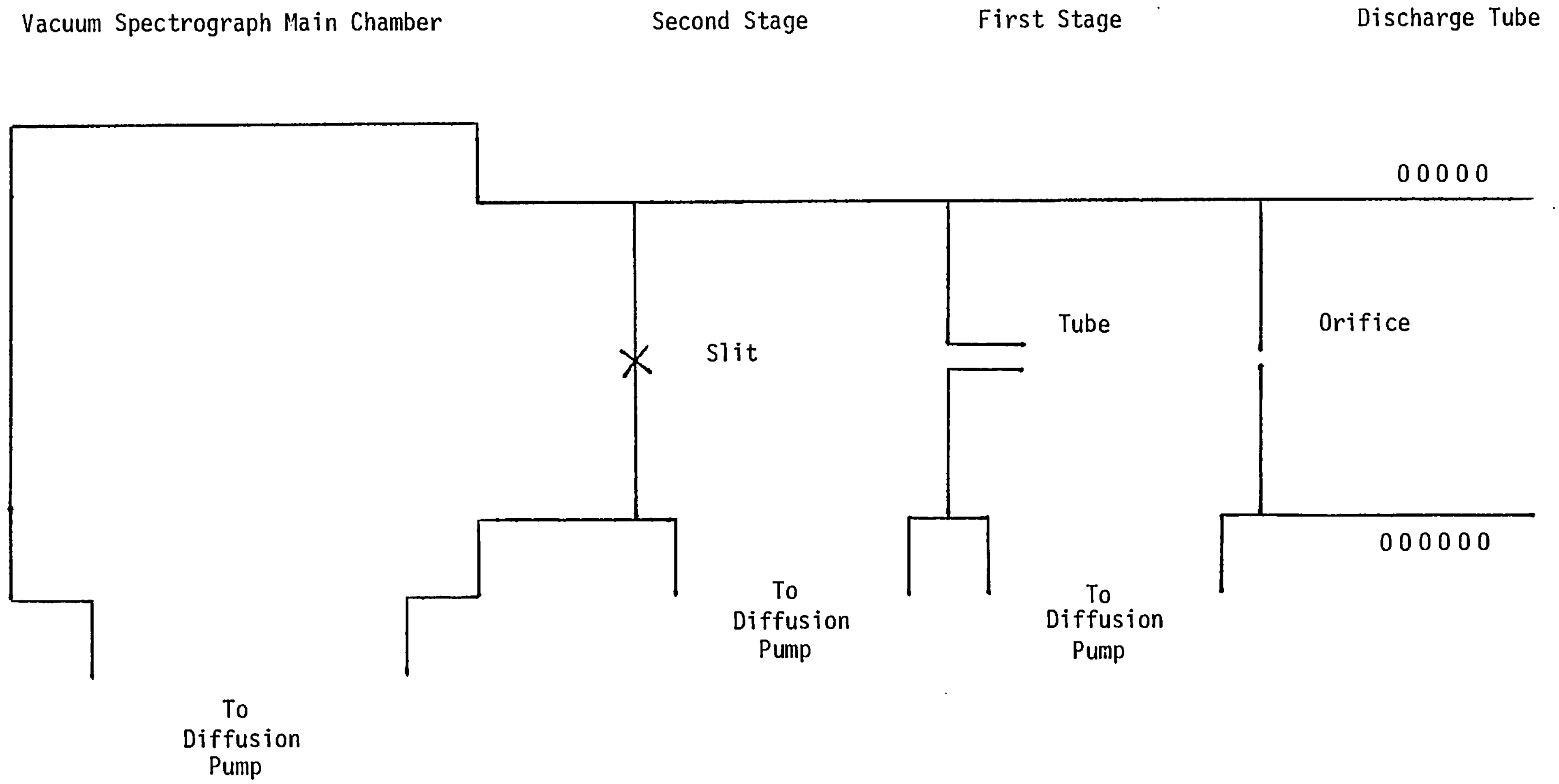

FIGURE 2.3.1 - Schematic Diagram of the Spectrograph End Containment System

insufficiently powerful to serve the important first differential pumping stage of the spectrograph end containment system. At the spectrograph S_2 was probably only 25 $\ell\,\mathrm{sec}^{-1}$ but $\frac{P_c}{P_3}$ was greater than 10^4.

On filling the discharge tubes with molecular oxygen and switching on the radio frequency oscillator, the containment system was found to perform at least as well as had been predicted by the above calculations. The temperature in the discharge was certainly higher than the value used in the calculations of this section (300 $^{\circ}$K), increasing the conductance of the impedances through equation 2.3.6. This is compensated by higher effective pumping speeds for a hot gas.

2.4 The discharge tube endplates

In this investigation, spectra were obtained using two quartz discharge tubes. This section describes the design of the endplates connecting the quartz cylinder to the differential pumping stages, and in which the first gas flow impedances were mounted. The original system consisted of a tube approximately 30 cms long and 10 cms in diameter, and incorporated the provision for adjustment of the absorption path length as follows. The first differential pumping stages consisted of a stainless steel "T" section of 7.5 cm bore connected via a flange and demountable vacuum coupling to one end of an auxiliary quartz tube 20 cms long and 3 cms in diameter. The far end of this auxiliary tube was drawn down by the glassblower to form the 2 mm orifice for gas flow impedance, and was supported at any desired point along the axis of the main cylinder by a demountable joint in the discharge tube endplates. The absorption path length could thus be set at any value between 30 and 0 cms. This is illustrated in Figure 2.4.1.

A cross section of the discharge tube endplates is shown in Figure 2.4.2. Brass is a dense metal (8.6 g'cc) and, to reduce weight, the water cooling cavity was made as large as possible. This also increases

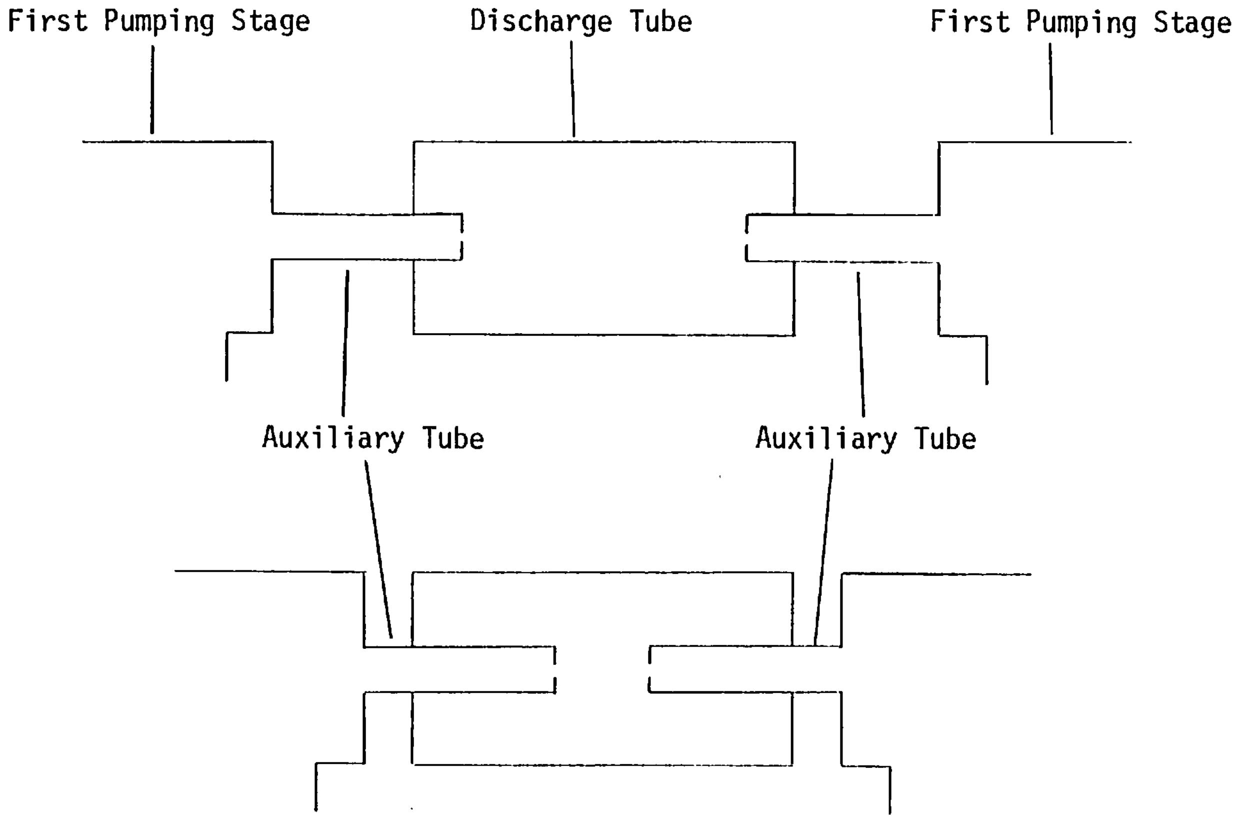

FIGURE 2.4.1

The Adjustment of the Absorption Path Length by the use of Auxiliary Quartz Tubes

FIGURE 2.4.2 - 30 cm Discharge Tube Endplates

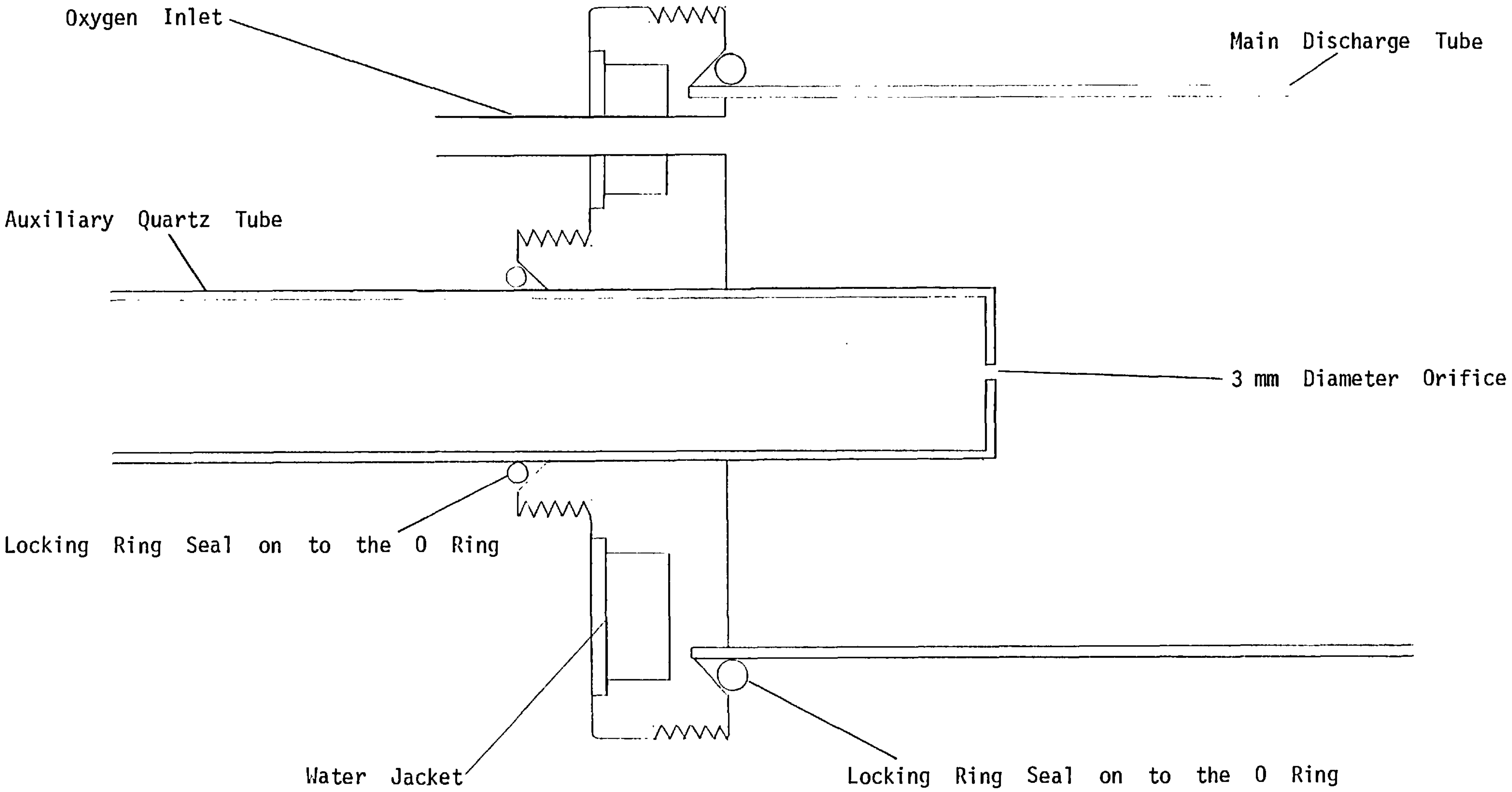

the surface area of the metal directly exposed to the coolant. The 6 mm OD copper oxygen inlet pipe was silver soldered to the brass superstructure. The vacuum seals were all demountable and Edward Viton O rings, offering increased thermal stability (up to 200 °C) were specified. Each endplate was supported on mounts clamped to an optical bench. During operation, it was observed that the discharge hardly extended beyond the induction coil windings which could not be placed closer than 2 cms to the vacuum locking ring on the endplates. This reduced the maximum absorption path length obtainable from this system to 26 cms. Molecular oxygen was admitted to the tube with a Leybold-Heraeus high precision variable leak valve.

The second system consisted of the 100 cm long, 6 cm diameter quartz discharge tube with the endplates attached directly to the T section flange of the first differential pumping stages. There was no provision for adjustment of the absorption path length. A sectional diagram of the endplates is shown in Figure 2.4.3. The entire assembly, apart from the cover of the water jacket, was essentially constructed from one piece of brass. There were thus no soldered joints exposed to the discharge. Such joints, in the first version of the endplates for the 100 cm tube had been prone to attack. The orifice was again set 2 to 3 cms into the discharge tube to avoid pockets of recombined gas from entering the light path. Another modification was to place a quartz 'cap' with a 2 mm diameter hole in the centre over the interior surface of the brass endplates. Experience had shown that the discharge attacked the metal surface forming a deposit on the interior of the quartz tube.

2.5 The continuum light source

A pulsed source of emission continuum of wide spectral coverage in the XUV was originally described by Balloffet, Romand and Vodar (9) and has since been known as the B.R.V. source. The device underwent further development at Imperial College and is known to produce continuum radiation from the visible to below 50 Å. In the absence of an electron synchrotron

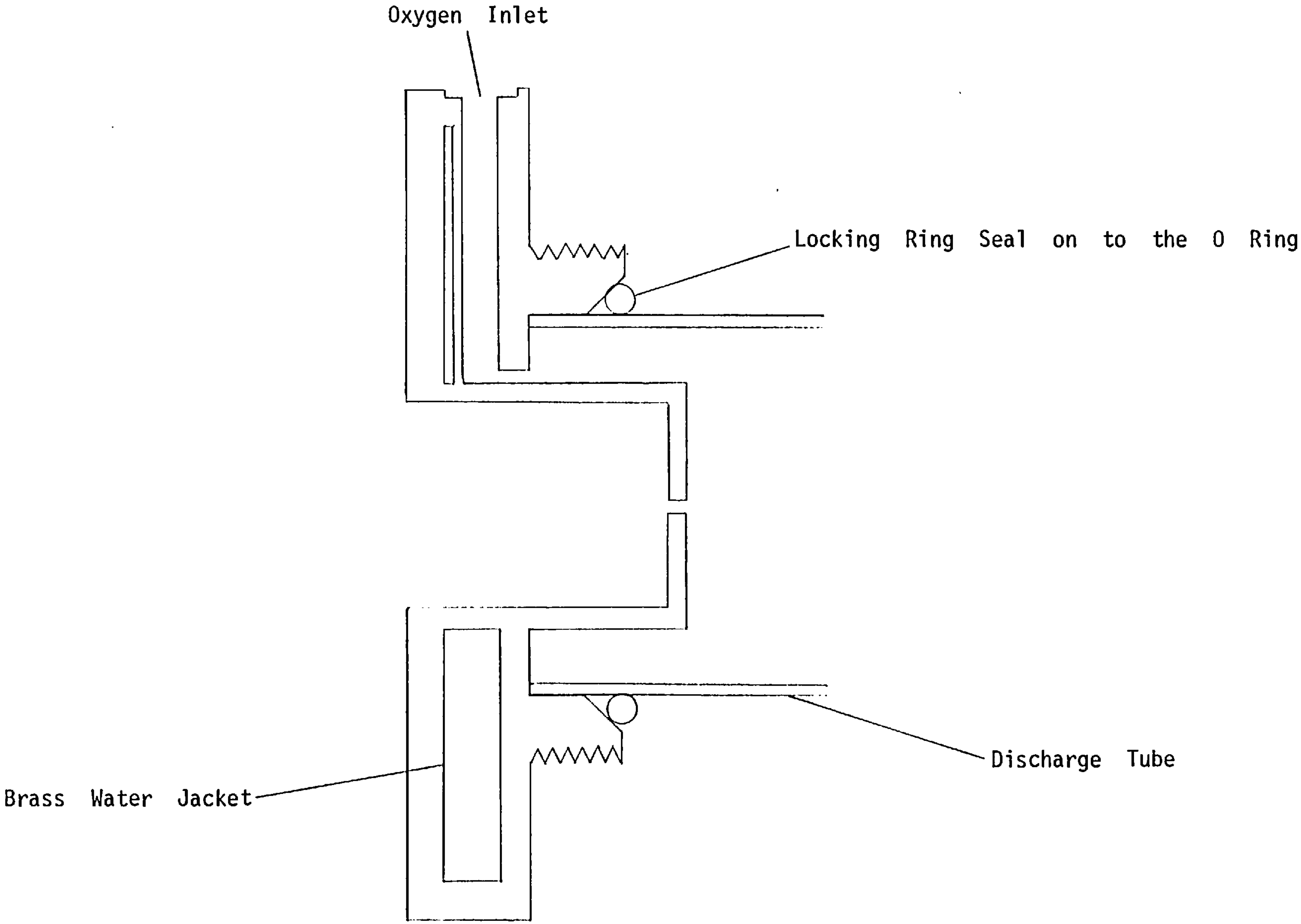

FIGURE 2.4.3 - 100 cm Discharge Tube Endplates

facility, it was the only choice of background light source for this experiment. A sectional view of the device is shown in Figure 2.5.1. The water cooled 6 mm diameter uranium anode pin is held at a potential of +40 Kv with respect to an earthed brass cathode by the charge on a 0.04 μF low inductance capacitor. A pressure of no more than 10^{-5} torr must be maintained in the vacuum housing to prevent self-discharge of the source. A triggering pulse is applied (from a thyratron unit) across the mica surface on the inside wall of the cathode. The thyratron unit produces a faster rising and more energetic pulse than the 2.5 Kv pulse transformer and 300 V pulse trigger unit employed hitherto in the use of the source at Imperial College. Another recent development was to shorten the length of the uranium anode pin from approximately 2.5 cms to 1.25 cms. These were found to be considerably cheaper, easier to cool and introduced no reduction in performance.

The mechanism by which radiation is produced has been described by Fox and Wheaton (10). The sliding spark produced at the cathode by the trigger voltage pulse creates free electrons which are accelerated towards the anode by the 40 Kv potential drop and initiates the discharge. Electrons impinging on the face of the anode both create a highly ionized uranium plasma and emit bremsstrahlung radiation. The plasma then pinches, due to interaction of the current stream with its own magnetic field, causing the electron density and temperature to increase rapidly. A second burst of bremsstrahlung emission occurs at this time. The radiation pulse from the source has a half-width of less than 1 μs.

The continuum obtained in the current use of the source proved to be quite clean above 400 Å with few emission or absorption lines superimposed. Below 400 Å the quality of the continuum was seen to deteriorate. The continuum as a whole became poor in quality and intensity if the pressure in the source vacuum chamber rose above 10^{-5} torr or if both the uranium

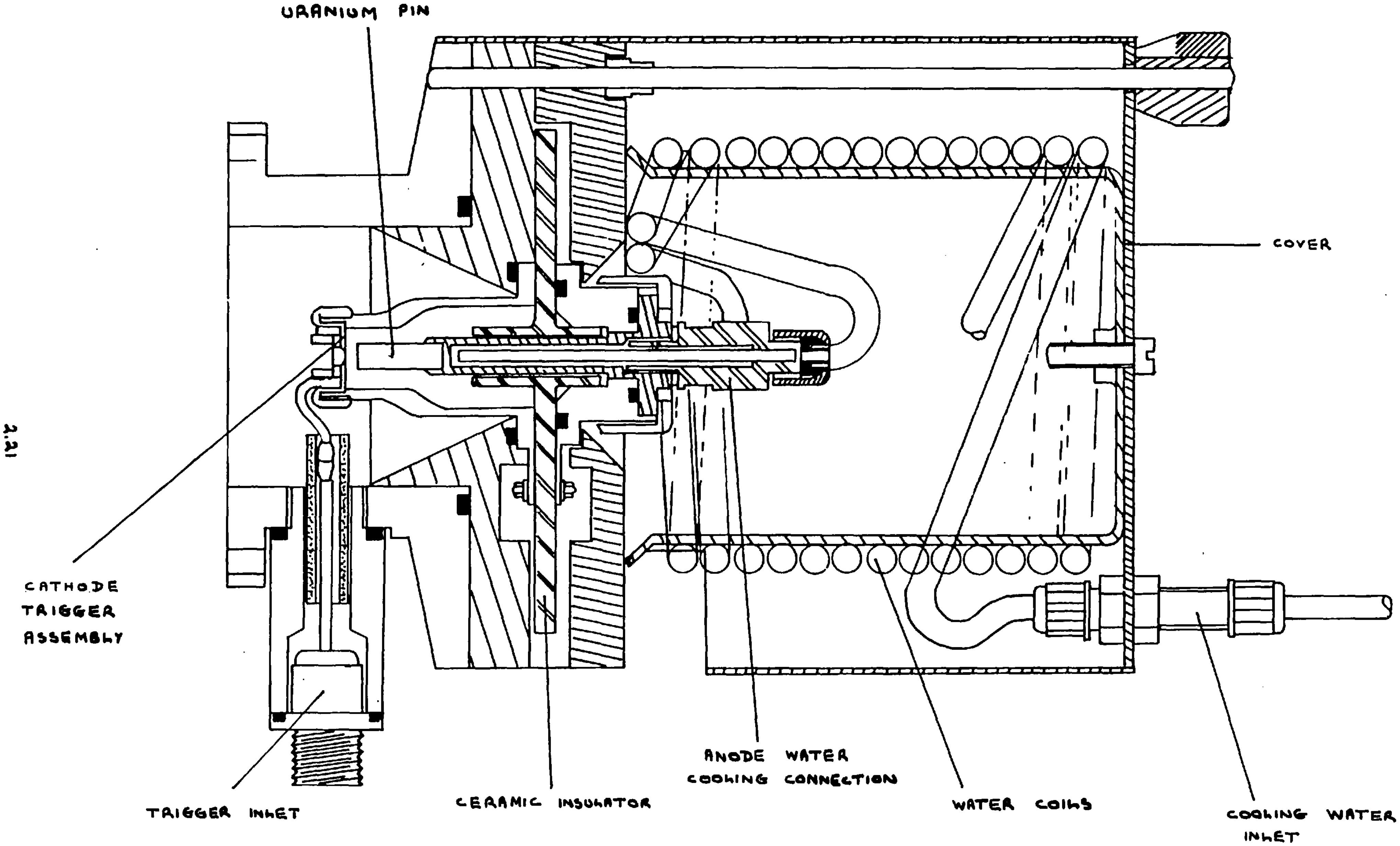

FIGURE 2.5.1 THE BRV SOURCE

anode pin and cathode were not changed frequently. Electron bombardment of the anode face at each firing of the source gradually wore a conical pit into the uranium surface. This probably inhibited the production of the highly ionized plasma which also tended to be confined by the rim around the base of the cone reducing the region of light emission. On the cathode, the sliding spark across the 250 μm gap separating the brass ring at which the trigger pulse is applied and the earthed body of the electrode (see Figure 2.5.2) enlarged the hole at the axis of the cathode. The mica insulation in the 250 μm gap eventually broke down and the source no longer triggered. Experience showed that 1800 was the maximum number of shots that could be expected from a set of electrodes to produce a continuum of high quality and sufficient intensity.

The limitation on the number of shots obtainable from one set of electrodes firstly made it desirable to optimise the light path between source and spectrograph grating to maximise the throughput and avoid 'wasting' radiation and secondly limited the choice of spectrograph plate to the very fast Kodak 101-01 emulsion described in Section 2.6.

2.6 The spectrograph and the photographic emulsion

The dispersing instrument for this experiment was a one metre normal incidence vacuum spectrograph designed by Vodar and Romand and manufactured under license by Jobin Yvon. Figure 2.6.1 is a diagram of the optical layout of the instrument. The original 1200 lines per mm concave grating was replaced by a one metre concave radius 2400 lines per mm gold coated diffraction grating manufactured by Bausch & Lomb. This required the design and construction of a new grating mount. The Bausch & Lomb grating was blazed at 625 Å and produced a linear dispersion of approximately 4 Å per mm along the plate. The dimensions of the grating were 2.5 cm by 2.5 cm. The focussing of the spectrograph was a lengthy process since no visible wavelengths could be observed in the instrument, at normal incidence, except

FIGURE 2.5.2

THE B.R.V. SOURCE CATHODE

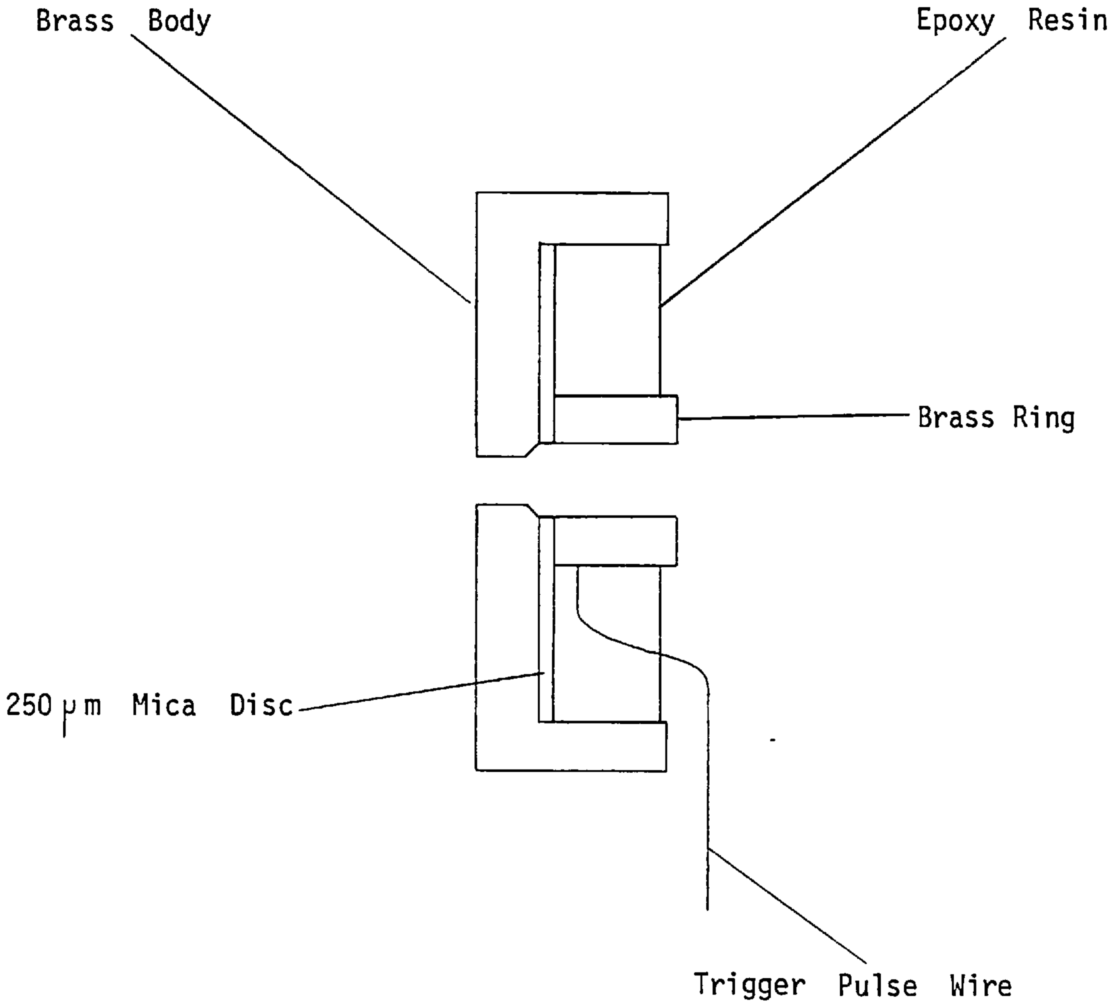

FIGURE 2.6.1

OPTICAL LAYOUT OF THE JOBIN YVON SPECTROGRAPH

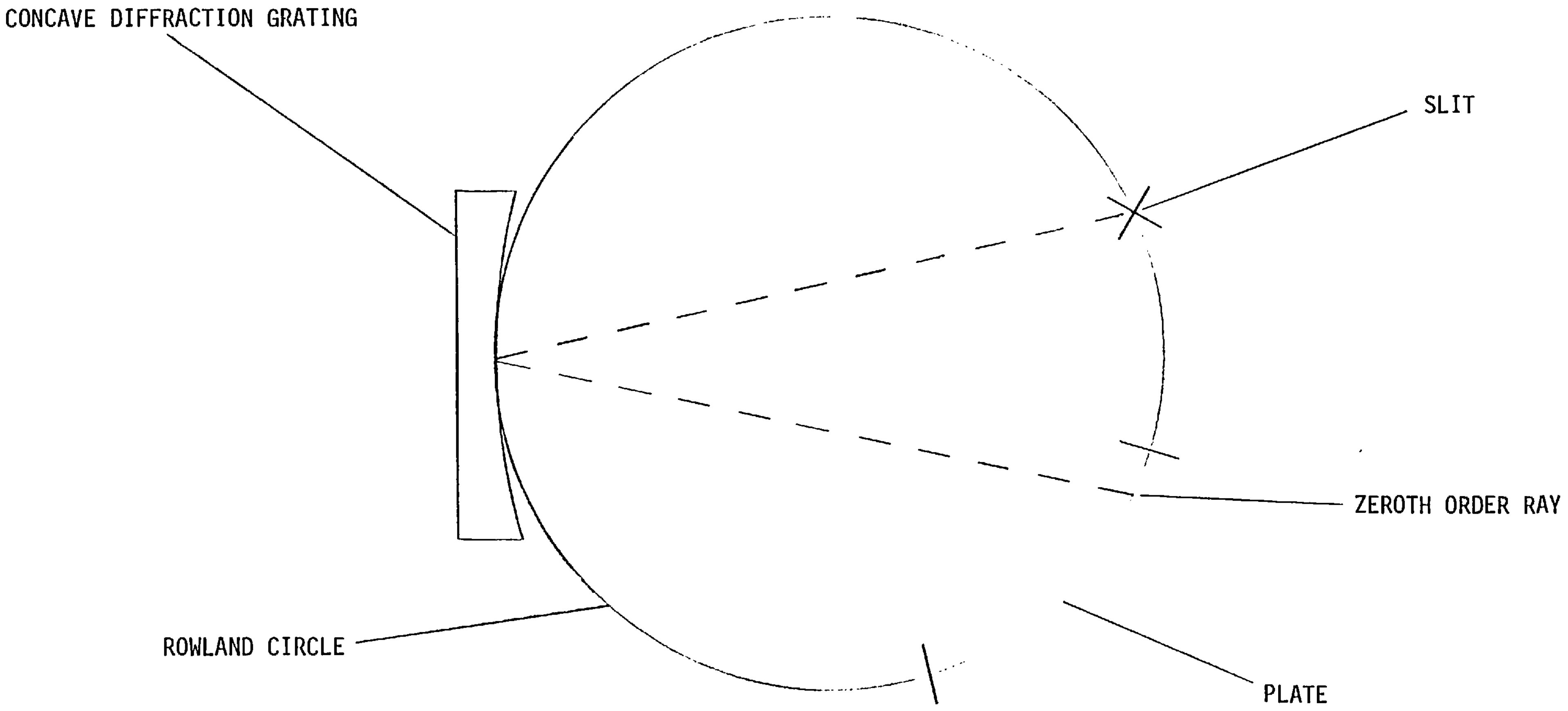

at zeroth order. Final focussing was completed by evacuating the spectrograph and taking a series of exposures with the Garton flashtube line source (20) attached to the entrance port. The instrument was let up to atmospheric pressure with cylinder nitrogen and small adjustments were made in the position of the grating between each exposure. The position of best focus was determined on processing the plate.

The spectrograph consisted of three vacuum chambers. The 'spark chamber' was spearately pumped, and served in this experiment, as the second differential pumping stage of the containment system (see Section 2.3). The instrument was originally designed for spectrochemical analysis of highly ionized states of metalloids particularly sulphur, carbon, phosphorus, nitrogen, oxygen and hydrogen. The electrode holders, incorporated to obtain vacuum sliding sparks with a 25 kV generator, were removed from the spark chamber for this investigation. The main grating vacuum chamber of the spectrograph was separated from the spark chamber by the slit and the gate valve. This vessel was evacuated by the instrument's 15 cm principal diffusion pump. The third part of the spectrograph consisted of the photographic plate chamber. This was roughly evacuated independently but diffusion pumped through the valve leading into the main chamber. Also incorporated into the plate chamber was a variable width horizontal slit, which permitted the height of the spectral lines on the plate to be adjusted, and provision for racking the plate holder to obtain several spectra on one piece of film. The spectral range of the instrument was 1350 to 300 Å. In fact, whilst focussing the instrument with the Garton flashtube emission lines of wavelength down to 150 Å were obtained.

The photographic emulsion used to record spectra was Eastman-Kodak special 35 mm film type 101-01. Gelatin absorbs radiation of wavelength less than 2200 angstroms strongly and an emulsion capable of recording ultraviolet radiation of concern to this experiment must contain an absolute minimum amount of gelatin. The silver halide grains in the Kodak 101-01 emulsion actually protrude from the extremely thin gelatin coating and unfortunately can be made developable by mechanical contact. The emulsion is thus very susceptible to chemical fogging and abrasion damage and great care is required in handling and processing. 150 micron thick narrow 'rails' of polystyrene beads embedded in and protruding from a layer of gelatin placed along both edges of the film, allow it to be rolled without subsequent mechanical abrasion of the film emulsion. On 35 mm film, the available image space between rails is about 28 mm.

The Kodak 101-01 is one of the most sensitive ultraviolet emulsions available and is suitable for experiments where exposure time is limited. At 1200 Å, for example, 101-01 is about 10 times as sensitive as Kodak SWR. In the experimental runs, processing was carried out according to the film manufacturers recommended procedures using D19 developer and dish development. The emulsion was soaked in distilled water for two minutes prior to development in order to reduce fogging. 101-01 is sensitive to radiation of wavelength in the range 50 to 4000 angstroms. It is a much finer grain film than the Kodak-Pathe SC5 and SC7 emulsions but the contrast is still low on comparison with plates for the visible. The rolls of film were always stored at reduced temperatures but allowed to reach room temperature before use.

2.7 Experimental runs to photograph the absorption spectrum of atomic oxygen at wavelengths from 600 Å to 350 Å

The absorption spectrum of atomic oxygen at wavelengths from 600 to 350 Å was photographed with the apparatus which has been described in Sections 2.2 to 2.6. This spectrum and the results of subsequent analysis are presented in the next chapter of this thesis.

On assembly, each component of the system had to be optically aligned accurately. The procedure adopted for this task in the case of the 100 cm tube, was as follows. Firstly a helium-neon laser, supported on its own optical bench, was aligned with the centres of the spectrograph slit and the concave diffraction grating. With the plateholder removed, the grating could be viewed, at a position away from zeroth order, through the plate chamber with a torch. The tube separating the spectrograph second differential pumping stage from the first, the first stage T section and the discharge tube endplate were then progressively attached and aligned with respect to the laser beam. With the source, the source end containment system and the second endplate loosely bolted to the supporting frame, all of the gas flow impedances at the source end were aligned along a common axis passing through the centre of the B.R.V. cathode. Finally, the frame was placed in between the spectrograph and the laser, the discharge tube was loosely clamped between both endplates and the whole frame moved on its adjusting screws so that the common axis of the source end containment system and the B.R.V. source cathode coincided with the laser beam. The quartz tube locking rings were then tightened. If an anglepoise lamp was directed at the grating through the plate chamber in zeroth order position, the brightly illuminated slit could be observed through the source cathode along the axis of the whole apparatus.

The system was now ready for evacuation. If the brass assembly supporting the B.R.V. uranium pin anode were replaced by a flat window resting against the O ring, the laser beam could be observed at the orifices in the discharge tube endplates and any (in fact, non-existent) movement in the equipment during evacuation could be detected and rectified. The frame supporting the entire source end of the apparatus was constructed for this experiment from welded 3.7 cm square tube. The source and source end differential pumping section were secured to it on mild steel mounting plates.

The spectrum was first photographed with the 30 cm discharge tube filled to a pressure of 600 microns (measured with the discharge off).

The tube was aligned by a procedure very similar to that described above. Plates were taken with 900 shots from the B.R.V. source and the full 30 cm path length. The slit width was approximately 20 microns. The wavelength range observed on the plate was from the upper limit of the instrument at 1350 Å to a lower limit set by the grating (and the point at which the continuum deteriorates) at 350 Å.

Some new transitions below 600 Å and the majority of the structure reported in reference (4) between 910 and 665 Å were observed. This proved that the discharge was accomplishing a considerable degree of dissociation and that substantial quantities of atomic oxygen were being produced. Indeed, the emission spectrum of O I was very prominent on the spectrograph plates at longer wavelengths. Moreover, molecular oxygen transitions superimposed on the spectrum were weak even though the discharge tube contained pure oxygen.

The 100 cm discharge tube was constructed in an attempt to increase the available integrated number density of atomic oxygen. This proved to be a success and below 600 Å more new transitions were observed which had not been seen on the spectra taken with the 30 cm tube. The molecular contamination of the spectrum as a whole (1350 Å to 350 Å) was also reduced. The Rydberg series, for example, observed by Codling and Madden (11) in molecular oxygen between 500 Å and 600 Å could no longer be seen on the plates. Plate 2.7.1 is the absorption spectrum of the 100 cm discharge from 750 Å to 690 Å. The molecular oxygen features at 720 Å and 732.5 Å are weak in comparison to the four atomic oxygen series converging to the O II $2p^3\ {}^2D^o$ limit at 731.8 Å. Plate 2.7.1 should be compared with Figure 5 of reference (4). The best plates were obtained with the tube filled to a pressure of 100 microns (measured with the discharge off) and with 3000 shots from the B.R.V. continuum source.

With both discharge tubes, the optimum filling pressures were

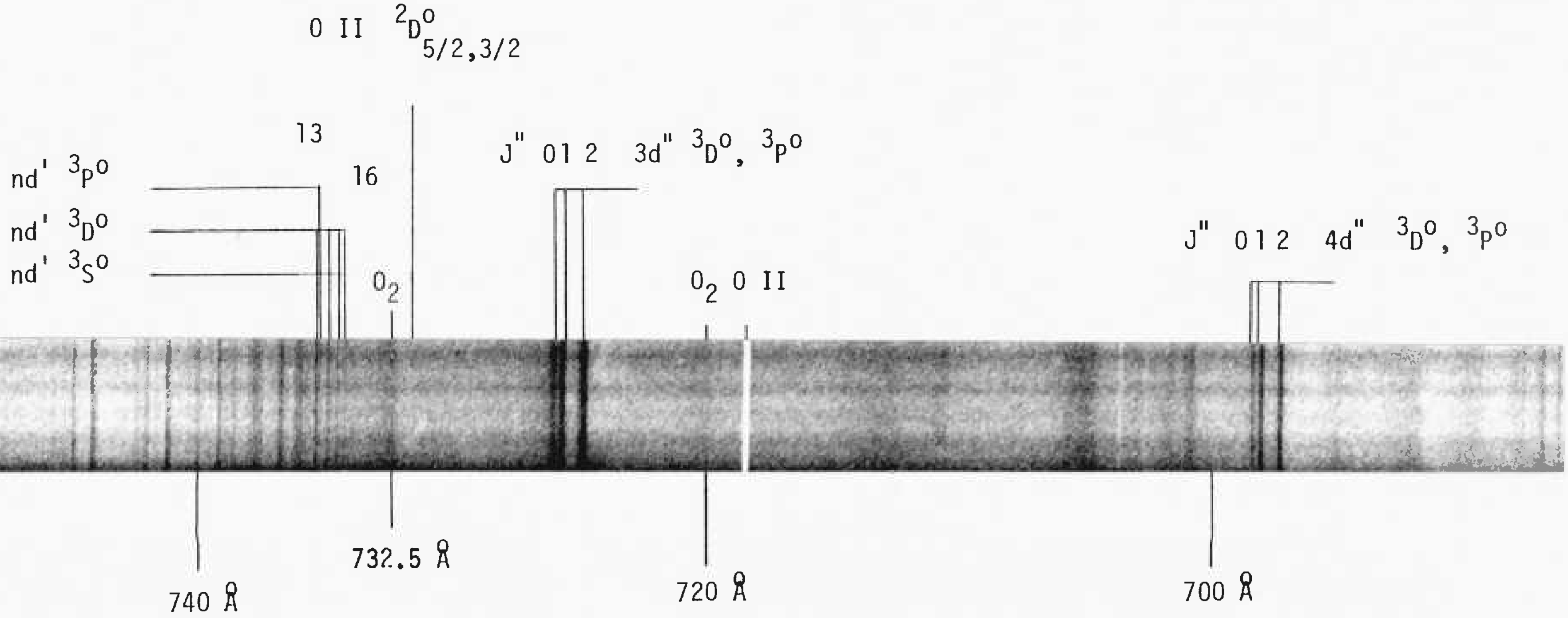

PLATE 2.7.1

ATOMIC OXYGEN ABSORPTION SPECTRUM 750 Å to 690 Å obtained empirically. The intensity of the visible discharge emission was found to fade rapidly on raising the filling pressure above the optimum values with the discharge collecting in localised pockets along the tube. The continuous absorption due to photoionization upon which the discrete structure was superimposed was found to rise rapidly as the pressure was increased and the number of shots required from the background light source had therefore to be adjusted empirically for each value. A spectrum of the source alone - i.e. with the absorption cell completely evacuated - was taken on each plate. The number of shots required for this to produce an exposure comparable to that of the spectrum through the radiofrequency discharge was typically 500 for the 100 cm tube.

CHAPTER III

NEW ABSORPTION SERIES OF ATOMIC OXYGEN IN THE VACUUM ULTRAVIOLET

3.1 Introduction

New absorption series from the O I ground state were observed on the photographic plates obtained in the experiments described in the previous chapter. Plate 3.1.1 is a photograph of the absorption spectrum of oxygen obtained in the 500 Å - 400 Å region. The photograph is a positive print, and therefore black denotes absorption. The new system, marked with vertical lines above the spectrum, is quite weak with respect to the continuous absorption upon which it is superposed. The wavelengths of the resonances were obtained by measurement of their locations along the plates and then interpolation between the known wavelengths of the O II emission lines observed in the spectrum. A table of the reference wavelengths is given in Appendix 1 and the computer program which was used for interpolation is described in Appendix 2. Microdensitometer traces of the spectrum are given in Figures 3.1.1, 3.1.2 and 3.1.3. No transitions have been observed in the spectrum of molecular oxygen in this wavelength region in previous work (12).

3.2 Interpretation

In order to classify the new O I absorption series, it is useful to determine the energy levels to which transitions are allowed from the ground state $1s^2\ 2s^2\ 2p^4\ {}^3P_{2,1,0}$. The spin selection rule $\Delta s = 0$ should be strictly obeyed for a light atom and this restricts the upper levels to triplet terms. The most likely transitions are those with $\Delta \ell = \pm 1$, which, for inner shell transitions in this region means 2s to np. The terms involved may be considered to be the result of adding a p electron to the four terms of O II resulting from the

PLATE 3.1.1

THE ATOMIC OXYGEN ABSORPTION SPECTRUM FROM 500 Å to 400 Å

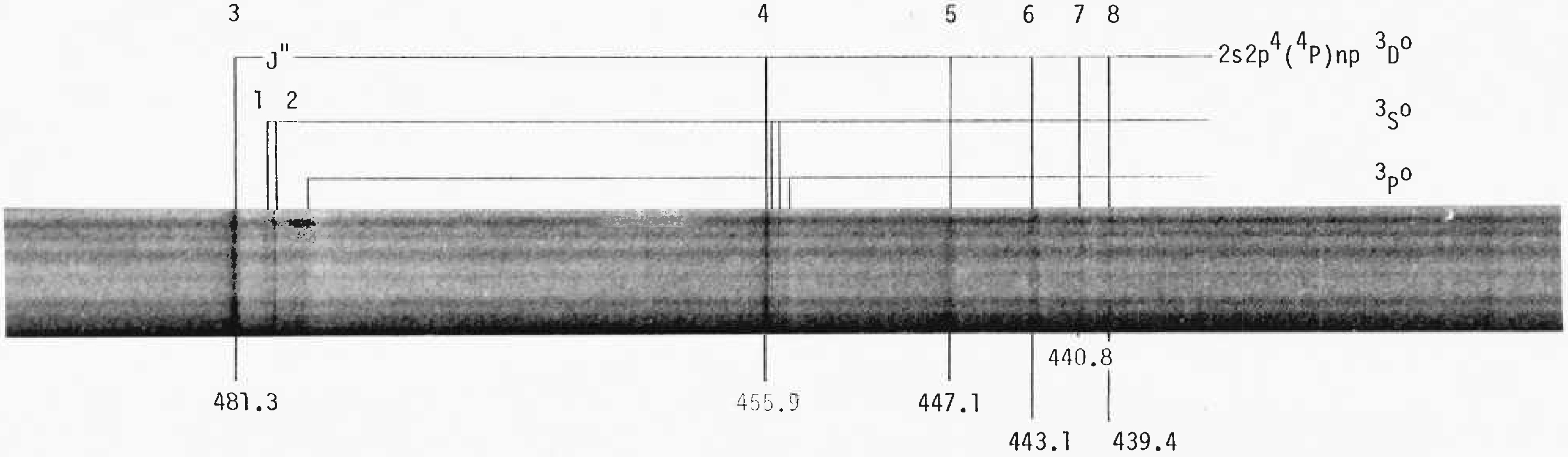

MICRODENSITOMETER TRACES OF THE NEW SERIES MEMBERS

FIGURE 3.1.1

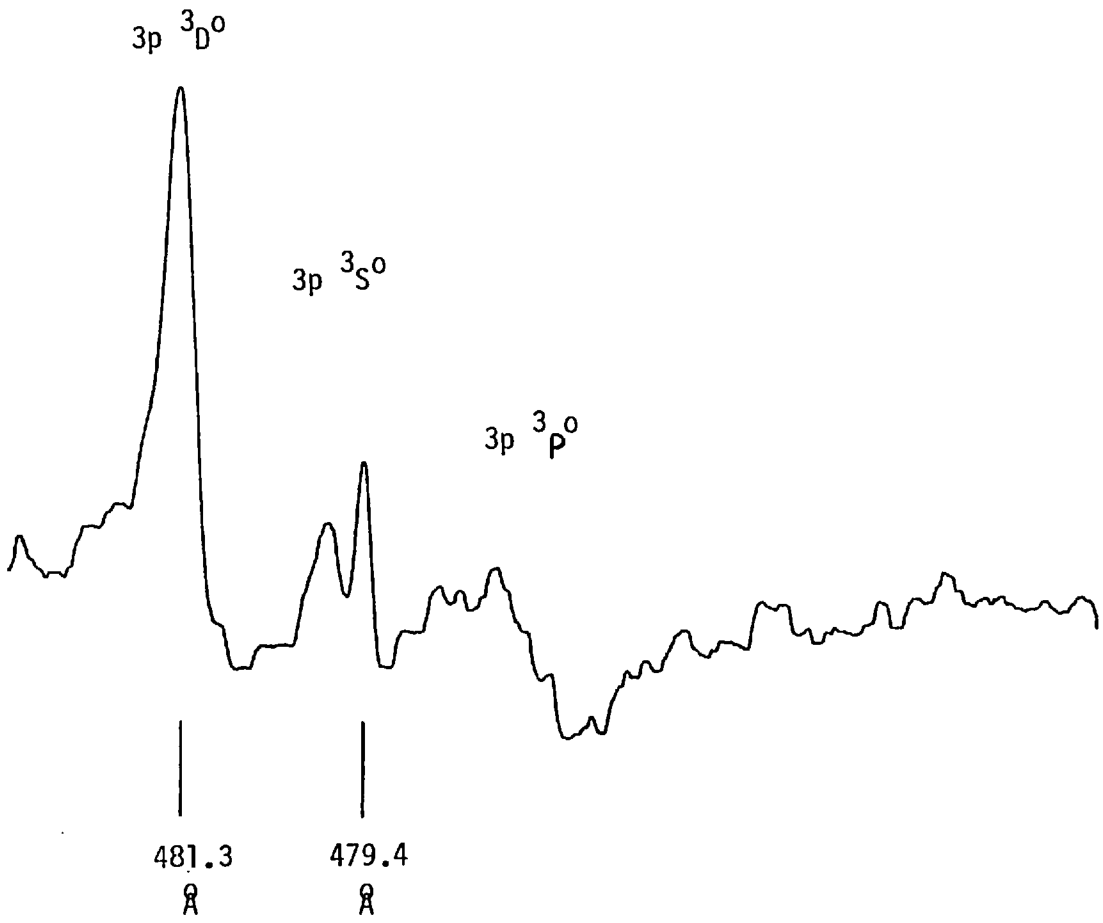

FIGURE 3.1.2

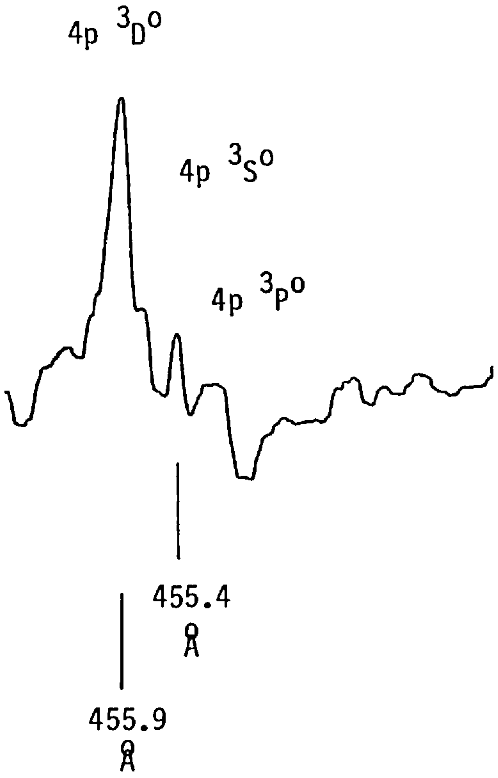

FIGURE 3.1.3

MICRODENSITOMETER TRACES OF THE NEW SERIES MEMBERS n = 5.8

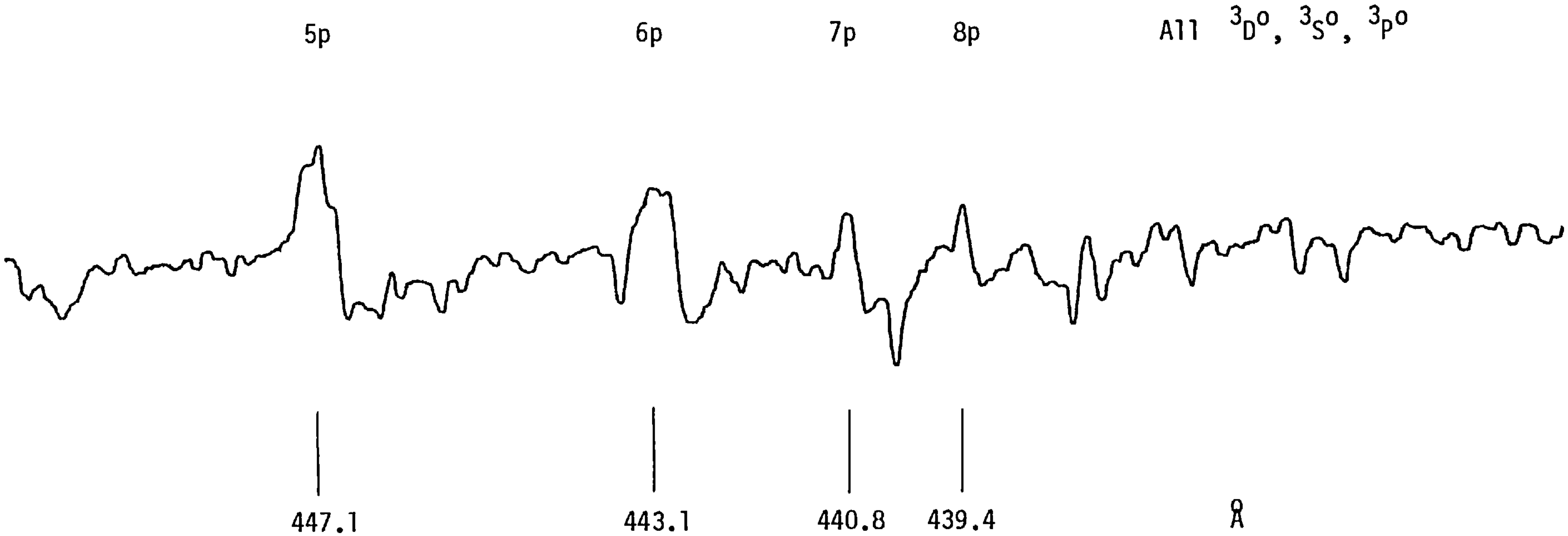

electron configuration $1s^2$ $2s$ $2p^4$. These are ^4P, ^2D, ^2S and ^2P in order of increasing energy. The resulting terms are obtained by combining the angular momentum of the p electron with the core angular momentum of these four parents. The possible transitions are further reduced by the selection rule $\Delta L = 0, \pm 1$ to the nine allowed term series given in Table 3.2.1. In addition, nine absorption series are allowed having the metastable terms $2p^4\ {}^1D_2$ or $2p^4\ {}^1S_0$ as the lower state. These are listed in Tables 3.2.2 and 3.2.3 respectively.

It can be seen on Plate 3.1.1 that the observed structure consists of one prominent Rydberg series with weak transitions belonging to one or two other series on the low wavelength side of each of its members. On the plates, the series were identified initially by their approximate convergence limits. These were obtained from the Rydberg-Ritz formula

$$\nu_\infty = \nu_i + R_0/(n^*)^2 \qquad (3.2.1)$$

In this expression, ν_∞ is the series limit, ν_i is the observed frequency of the series member, n^* is the effective principal quantum number obtained from the frequency differences of likely adjacent series members and term tables (16). R_0 is the Rydberg constant for oxygen atoms which was taken (14) to be 109733.55 cm^{-1}.

The average series limit (for the most prominent series) is given in Table 3.2.4. It is 435.3 (± 0.2) Å, which is close to the 435.4 Å for the $2s\ 2p^4\ {}^4P_{5/2}$ level of O II, computed from the sum of measured(13) transitions from the O II ground state $2p^3\ {}^4S^o_{3/2}$ and the measured (14) value of the limit O I $2p^4\ {}^3P_2$ to O II $2p^3\ {}^4S^o_{3/2}$, 109837.03 cm^{-1} (see Table 3.2.1). The observed series was thus attributed to the family with upper states $2p^4\ ({}^4P)np\ {}^3D^o, {}^3S^o, {}^3P^o$ converging to the limit

TABLE 3.2.1

Summary of the Atomic Oxygen Series resulting from the Excitation of a 2s Electron from the ground state $2p^4\ ^3P_2$

O II Term	Term value from O I ground state(1) (cm^{-1})		Convergence Limit(1) (Å)	O I Series
$2s\ 2p^4(^4P)$	$^4P_{5/2}$	229674.73	435.40	$2s2p^4(^4P)np\ ^3D^o, ^3S^o, ^3P^o$
	$^4P_{3/2}$	229838.13	435.09	
	$^4P_{1/2}$	229920.53	434.93	
$2s\ 2p^4(^2D)$	$^2D_{5/2}$	275824.73	362.55	$2s\ 2p^4(^2D)np\ ^3D^o, ^3P^o$
	$^2D_{3/2}$	275833.03	362.54	
$2s\ 2p^4(^2S)$	$^2S_{1/2}$	305547.43	327.28	$2s\ 2p^4(^2S)np\ ^3P^o$
$2s\ 2p^4(^2P)$	$^2P_{3/2}$	322430.23	310.15	$2s\ 2p^4(^2P)np\ ^3D^o, ^3S^o, ^3P^o$
	$^2P_{1/2}$	322599.43	309.98	

1. The series limits were computed from the sum of measured transitions from the O II ground state $2p^3\ ^4S^o{}_{3/2}$ (reference 13) and the value of the limit O I $2p^4\ ^3P_2$ to O II $2p^3\ ^4S^o{}_{3/2}$, 109837.03 cm^{-1} (reference 14).

TABLE 3.2.2

Summary of the Atomic Oxygen Series resulting from the Excitation of a 2s Electron from the Metastable State $2p^4\ ^1D_2$

O II Term	Term value from $2p^4\ ^1D_2$ (1) (cm^{-1})		Convergence Limit(1) (Å)	O I Series
$2s\ 2p^4(^2D)$	$^2D_{5/2}$	259956.87	384.68	$2s2p^4(^2D)np\ ^1P_1^o, ^1D_2^o, ^1F_3^o$
	$^2D_{3/2}$	259965.17	384.67	
$2s\ 2p^4(^2S)$	$^2S_{1/2}$	289679.57	345.21	$2s2p^4(^2S)np\ ^1P_1^o$
$2s\ 2p^4(^2P)$	$^2P_{3/2}$	306562.37	326.20	$2s2p^4(^2P)np\ ^1P_1^o, ^1D_2^o$
	$^2P_{1/2}$	306731.57	326.02	

1. The series limits were computed from the sum of measured transitions from the O II ground state $2p^3\ ^4S^o_{3/2}$ (reference 13) and the difference between the terms O I $2p^4\ ^1D_2$ and O II $2p^3\ ^4S^o_{3/2}$ 93969.17 cm^{-1} (references 14 and 15).

TABLE 3.2.3

Summary of the Atomic Oxygen Series resulting from the Excitation of a 2s Electron from the Metastable State $2p^4\ {}^1S_0$

O II Term	Term value from O I $2p^4\ {}^1S_0$ (1) (cm^{-1})		Convergence Limit (1) (Å)	O I Series
$2s\ 2p^4(^2D)$	$^2D_{5/2}$	242032.15	413.17	$2s\ 2p^4(^2D)np\ {}^1P_1^o$
	$^2D_{3/2}$	242040.45	413.15	
$2s\ 2p^4(^2S)$	$^2S_{1/2}$	271754.85	367.98	$2s\ 2p^4(^2S)np\ {}^1P_1^o$
$2s\ 2p^4(^2P)$	$^2P_{3/2}$	288637.65	346.46	$2s\ 2p^4(^2P)np\ {}^1P_1^o$
	$^2P_{1/2}$	288806.85	346.25	

1. The series limits were calculated from the sum of measured transitions from the O II ground state $2p^3\ {}^4S^o_{3/2}$ (reference 13) and the difference between the terms O I $2s^2\ 2p^4\ {}^1S_0$ and O II $2s^2\ 2p^3\ {}^4S^o_{3/2}$ 76044.45 cm^{-1} (references 14 and 15).

TABLE 3.2.4

Rydberg-Ritz Calculation of the Limits of the New Series

Wavelength of the transition E (1) (Å)	E (cm^{-1})	Difference from adjacent series member (cm^{-1})	n^* (2)	Series limit calculated from the Rydberg-Ritz formula (3) (Å)
481.3	207774.2	-	-	-
455.9	219333.0	11558.8	3.229	435.05
447.1	223671.7	4338.7	4.243	435.22
443.1	225691.9	2020.2	5.306	435.56
440.8	226858.5	1166.7	6.259	435.43
439.4	227582.3	723.7	7.243	435.40

1. For the most prominent series.
2. The values of n^* are obtained from Rydberg interpolation tables (reference 16).
3. The average series limit is 435.3 ± 0.2 Å, 229710 ± 90 cm^{-1}.

$2s\ 2p^4\ {}^4P$ at approximately 435 Å. No structure converging to any of the other limits given in Tables 3.2.1, 3.2.2 or 3.2.3 could be positively identified in the region of observation.

The separation of the weaker lines grouped around the first two members of the stronger series is given in Table 3.2.5. These values are compared with theoretical values (derived in calculations which are described in the next chapter) which are given in Table 4.3.11. The degree of correspondence is good and on this basis each transition was assigned to a series and a principal quantum number allocated. For a particular n, the terms run ${}^3D^o$, ${}^3S^o$ and ${}^3P^o$ in order of increasing energy. The most prominent series is the ${}^3D^o$ and the numbers from $n = 3$ ($207774.2\ \text{cm}^{-1}$) to $n = 8$ are labelled on Plate 3.1.1. The three series will be discussed in detail in Sections 3.3, 3.4 and 3.5.

In the Rydberg-Ritz formula (3.2.1) the effective quantum number is often expressed in terms of the principal quantum number n and the quantum defect :

$$n^* = n - \mu \qquad (3.2.2)$$

μ is a measure of how hydrogen-like the series is and is highly dependent on the degree of penetration of the outer electron's orbit into the core. μ varies rapidly with the orbital angular momentum quantum number ℓ, for a particular n but is almost independent of n for a particular ℓ (and an unperturbed series).

The quantum defects for the atomic oxygen series converging to terms arising from the O II configuration $1s^2\ 2s^2\ 2p^3$ are roughly 1.2 for the ns series and 0.03 for the nd series (4). The average value of the quantum defect for the series $2s\ 2p^4({}^4P)np\ {}^3D^o$ observed in this experiment was 0.74. This is close to the value (0.77) for the forbidden series with upper levels $2s^2\ 2p^3({}^4S^o_{3/2})np\ {}^5P_{3,2,1}$
reported by Isberg (17). $np\ {}^3P_{2,1,0}$

TABLE 3.2.5

A Comparison of the Wavenumber Differences between New Series Members and the Calculated Differences

Transition	Transition Wavenumber (cm^{-1})	Difference(2) (cm^{-1})	Calculated(1) Difference (cm^{-1})
3p $^3D^o$	207774.2		
3p $^3S^o$	208441.1, 208604.6	666.9, 830.4	791.59
3p $^3P^o$	209401.8	1627.6	1417.70
4p $^3D^o$	219333.0		
4p $^3S^o$	219455.7, 219602.5	122.7, 269.5	217.16
4p $^3P^o$	219852.8	519.8	503.23

1. See Table 4.3.11.
2. See Section 3.5. The differences quoted are from the two strongest transitions at 207774.2 and 219333.0 cm^{-1}.

3.3 The series with upper states $1s^2\ 2s\ 2p^4(^4P)np\ ^3D^o$

The series with upper states $2s\ 2p^4(^4P)np\ ^3D^o$ is given in Table 3.3.1. for $n = 3$ to 8 and illustrated in Plate 3.1.1. The series was the most prominent of the three observed, and for a particular principal quantum number, the members of this series were lowest in energy. The multiplet splittings of the $^3D^o$ terms were not observed. The average convergence limit was 435.3 ± 0.2 Å, 229710 ± 90 cm^{-1}, which is close to the expected value given in Table 3.2.1. Wavelength measurements for each of the transitions were taken at the visual estimate of the region of greatest absorption. As all the lines are diffuse, the measurements are inherently of low precision. The accuracy of the values quoted in Table 3.2.1 depends on the width and the strength of the resonances.

It may be observed from Plate 3.1.1 that the $n = 5$ and $n = 6$ members of this series are very broad. The upper levels are allowed to autoionize into the nd $^3D^o$, ns', nd', $^3D^o$ and nd'' $^3D^o$ continua. There is no definite indication on the microdensitometer traces of the transitions (given in Figures 3.1.1, 3.1.2 and 3.1.3) that the profiles are asymmetric (18,19).

3.4 The series with upper states $1s^2\ 2s\ 2p^4(^4P)np\ ^3S_1^o$

The series with upper states $2s\ 2p^4(^4P)np\ ^3S_1^o$ is given in Table 3.4.1. Only the $n = 3$ and $n = 4$ members of the series could be distinguished. The splitting of the lower levels $^3P_2$ and $^3P_1$ was observed and measured as 163.5 cm^{-1} for $n = 3$ and 146.8 cm^{-1} for $n = 4$. This is to be compared to the 158.29 cm^{-1} given in reference (4). The resonances appeared to be pure absorption lines and the midpoint of the line was measured. The upper levels are allowed to autoionize into the ns $^3S_1^o$ and nd' $^3S_1^o$ continua.

TABLE 3.3.1

Observed Absorption Series $1s^2\ 2s^2\ 2p^4\ ^3P_{2,1,0}$

to $1s^2\ 2s\ 2p^4(^4P)np\ ^3D^o_{3,2,1}$

n	E (cm^{-1})	E (Å)	n*	μ	Remarks
3p $^3D^o$	207774.2	481.3			1
4p $^3D^o$	219333.0	455.9	3.229	0.771	1
5p $^3D^o$	223671.7	447.1	4.243	0.757	2
6p $^3D^o$	225691.9	443.1	5.306	0.694	2
7p $^3D^o$	226858.5	440.8	6.259	0.741	1
8p $^3D^o$	227582.3	439.4	7.243	0.757	1
O II ^4P		435.3 ± 0.2			

1. Estimated uncertainty is 0.1 Å.
2. Estimated uncertainty is 0.2 Å.

TABLE 3.4.1

Observed Absorption Series $1s^2\ 2s^2\ 2p^4\ {}^3P_{2,1,0}$

to $1s^2\ 2s\ 2p^4(^4P)np\ {}^3S^o_1$

n	J"	J	E (cm^{-1})	E (cm^{-1})	E (Å)	Remarks
3p $^3S^o_1$	1	1	208441.1		479.8	1
	2	1	208604.6	163.5	479.4	1
4p $^3S^o_1$	1	1	219455.7		455.7	1
	2	1	219602.5	146.8	455.4	1

1 Estimated uncertainty is 0.1 Å.

3.5 The series with upper states $1s^2 2s2p^4(^4P)np\ ^3P^o_{2,1,0}$

The series with upper states $2s2p^4(^4P)np\ ^3P^o_{2,1,0}$ was the weakest system identified in this investigation. Only the n=3 and n=4 members can be distinguished on Plate 3.1.1. The lines are broadened by autoionization and have an asymmetric profile (18,19) with the cross section lower on the low wavelength side. Approximate wavelength measurements were obtained from the microdensitometer traces of Figures 3.1.1 and 3.1.2 by comparing the separation of the $^3D^o$, $^3S^o$ and $^3P^o$ terms for n=3 and n=4. For the asymmetric $^3P^o$ resonances the point of greatest rate of change of plate density was taken as the 'line centre'. These give the separation of the 3p $^3P^o$ term from the 3p $^3D^o$ as 1.96 times the separation of the 3p $^3S^o$ ($J'' = 2$) from the 3p $^3D^o$ or 1627.6 cm^{-1}. The corresponding value for n=4 is 519.8 cm^{-1} (the observed and calculated separations are compared in Table 3.2.5). This procedure puts the 3p $^3P^o$ term at 209402 ± 44 cm^{-1}, 477.6 ± 0.1 Å and the 4p $^3P^o$ term at 219853 ± 48 cm^{-1}, 454.9 ± 0.1 Å.

In Chapter I it was noted that Dehmer, Berkowitz and Chupka (6) had observed that the term $1s^2 2s2p^5\ ^3P^o$ autoionizes. This term is autoionization forbidden in Russell-Saunders coupling but the $2s2p^4(^4P)np\ ^3P^o_{2,1,0}$ terms are allowed to autoionize to the nd' $^3P^o$ and ns", nd" $^3P^o$ continua.

CHAPTER IV

CALCULATION OF THE $1s^2\ 2s\ 2p^4(^4P)np\ ^3D^o,\ ^3S^o,\ ^3P^o$ TERMS OF ATOMIC OXYGEN

4.1 Introduction

The classification of lines in an observed spectrum can often be aided by calculation of the theoretical energy levels. In the previous chapter the theoretical energy differences between the $2s\ 2p^4(^4P)np\ ^3D^o$, $^3S^o$ and $^3P^o$ terms for particular values of n were compared with the measured separations of lines on the spectrum. The calculation of these upper state term values by the Hartree Fock self-consistent field technique will now be described.

In the Central Field approximation, each atomic electron is assumed to move in a central potential arising from the nuclear charge and the spherically averaged potential of all the other electrons in the atom. The simplest wavefunction describing the atomic system as a whole, which is totally antisymmetric with respect to an exchange of the co-ordinates and spin of a pair of electrons is the Slater Determinant whose elements are the single electron spin orbital functions, each of which consists of a product of radial, angular and spin functions. Small deviations in the spherical symmetry of the potential in which each electron moves may be treated as perturbations which, in the LS coupling approximation, split the (previously degenerate) configuration into terms whose perturbed wavefunctions are linear combinations of Slater Determinants and eigenfunctions of the operators L^2, S^2, L_z and S_z.

The set of operators L^2, S^2, L_z and S_z all commute with each other and therefore there exists a complete set of orthonormal simultaneous eigenstates u_k^o. Such a set may be used to expand any arbitrary function and in particular a solution of the Schrodinger Equation

$$u = \sum_k C_k \, u_k^o \tag{4.1.1}$$

Substitution of Eqn.(4.1.1) into the Schrodinger equation, multiplication by u_n^{o*} and integration yields

$$\sum_k C_k \, (H_{nk}^o - E \, \delta_{nk}) = 0 \tag{4.1.2}$$

where

$$H_{nk}^o = \int u_n^{o*} \, H \, u_k^o \, d\gamma \tag{4.1.3}$$

are matrix elements of the Hamiltonian with respect to the u_k^o.

(4.1.2) is a set of n homogeneous linear equations in k unknowns C_k which has non trivial solutions if and only if the matrix of the coefficients is singular, i.e.

$$\left| H_{nk}^o - E \, \delta_{nk} \right| = 0 \tag{4.1.4}$$

This is known as the secular or characteristic equation.

The operators L^2, S^2, L_z and S_z also commute with the nonrelativistic Hamiltonian for the N electron system, in atomic units

$$H = -\frac{1}{2} \sum_{i=1}^{N} \left(\nabla_i^2 + \frac{2z}{r_i} \right) + \sum_{\text{pairs } i,j} \frac{1}{r_{ij}} \tag{4.1.5}$$

all of the linearly independent set of eigenfunctions u_k^o of L^2, S^2, L_z and S_z which are non-degenerate are therefore also eigenfunctions of the Hamiltonian, i.e. $u = u_k$. Each degenerate eigenfunction of L^2, S^2, L_z and S_z is not in general an eigenfunction of the

Hamiltonian also, but the expansion of the function which is (Eqn.4.1.1) will involve only the u_k^o belonging to this degenerate set of eigenvalues. Non-diagonal terms in the secular equation therefore only arise in those cases in which there are degenerate eigenfunctions of L^2, S^2, L_z and S_z. This occurs, for example, in configurations for which there are several repeated terms $({}^{2S+1}L)$ of different parentage $({}^{2Sp+1}Lp)$.

Slater(22a) has tabulated for the p^n, $p^n\ell$, $\ell^n s$, $\ell^n\ell's$, d^n and d^np configurations the matrix elements of the Hamiltonian with respect to eigenfunctions of L^2, S^2, L_z and S_z which have eigenvalues

$M_L = 0$, $M_S = 0$ for configurations consisting of an even number of electrons,

$M_L = 0$, $M_S = 1/2$ for those consisting of an odd number of electrons.

These matrix elements are expressed relative to the mean of the energy of the terms arising from the configuration (21a), each weighted by the number of degenerate states belonging to the term -(2L+1)(2S+1). This mean is called by Slater the average energy of the configuration. The matrix elements (and the average energy) are expressed in terms of the following integrals (21b) involving the radial functions of two electrons $P_{n\ell}(r)$ and $P_{n\ell}(s)$.

$$F^k(n_i\ell_i\,,\ n_j\ell_j) =$$

$$\int_0^\infty \int_0^\infty P^*_{n_i\ell_i}(r)\, P^*_{n_j\ell_j}(s)\, U^k(r\,,s)\, P_{n_i\ell_i}(r)\, P_{n_j\ell_j}(s)\, dr\, ds \qquad (4.1.6)$$

$$G^k(n_i\ell_i\,,\ n_j\ell_j) =$$

$$\int_0^\infty \int_0^\infty P^*_{n_i\ell_i}(r)\, P^*_{n_j\ell_j}(s)\, U^k(r\,,s)\, P_{n_j\ell_j}(r)\, P_{n_i\ell_i}(s)\, dr\, ds \qquad (4.1.7)$$

where $$u^k(r,s) = \frac{s^k}{r^{k+1}} \quad \text{for} \quad r \geqslant s$$

$$= \frac{r^k}{s^{k+1}} \quad \text{for} \quad r \leqslant s.$$

4.2 Calculation of the average energy of the configurations $1s^2\ 2s\ 2p^4\ np$ and of the F^k and G^k integrals

In terms of the F^k and G^k integrals the average energies of the configurations $1s^2\ 2s\ 2p^4\ np$ are given $^{(21a)}$ by

$$E_{AV} = \sum_{i=1}^{N=8} I(n_i\ell_i) + F^0(1s,1s) + 6\left[F^0(2p,2p) - \frac{2}{25}F^2(2p,2p)\right]$$

$$+ 2\left[F^0(1s,2s) - \frac{1}{2}G^0(1s,2s)\right] + 8\left[F^0(1s,2p) - \frac{1}{6}G^1(1s,2p)\right]$$

$$+ 2\left[F^0(1s,np) - \frac{1}{6}G^1(1s,np)\right] + 4\left[F^0(2s,2p) - \frac{1}{6}G^1(2s,2p)\right]$$

$$+ \left[F^0(2s,np) - \frac{1}{6}G^1(2s,np)\right]$$

$$+ 4\left[F^0(2p,np) - \frac{1}{6}G^0(2p,np) - \frac{1}{15}G^2(2p,np)\right] \qquad (4.2.1)$$

where

$$I(n_i\ell_i) =$$

$$\int_0^\infty P_{n_i\ell_i}(r)\left[-\frac{d^2}{dr^2} - \frac{2z}{r} + \frac{\ell_i(\ell_{i+1})}{r^2}\right]P_{n_i\ell_i}(r)\,dr \qquad (4.2.2)$$

The radial functions $P_{n_i\ell_i}(r)$ can be varied to minimize the average energy of each configuration subject to the following constraints

(i) Boundary conditions

$$P_{n_i \ell_i}(0) = P_{n_i \ell_i}(\infty) = 0 \qquad (4.2.3)$$

(ii) Normalization conditions

$$\int_0^\infty P^*_{n_i \ell_i}(r) \; P_{n_i \ell_i}(r)\, dr = 1 \qquad (4.2.4)$$

(iii) Orthogonality conditions between functions of the same angular momentum quantum number

$$\int_0^\infty P^*_{n_i \ell_i}(r) \; P_{n_j \ell_j}(r)\, dr = 0 \quad \text{for} \quad \ell_i = \ell_j \quad i \neq j \qquad (4.2.5)$$

(iv) The number of nodes $= n_i - \ell_i - 1$ (4.2.6)

(v) The initial slope $a_o = P_{n_i \ell_i}(r)/r^{\ell_{i+1}} > 0$, as $r \rightarrow 0$ (4.2.7)

This results (22b) in the Hartree-Fock equations for the functions $P_{n_i \ell_i}(r)$

$$\left[- \frac{d^2}{dr^2} - \frac{2z}{r} + \frac{\ell_i \, (\ell_{i+1})}{r^2} + \sum (\text{all electrons}) \, \frac{2}{r} \; Y_o(n\ell, n\ell; r) - X \right] P_{n_i \ell_i}(r)$$

$$= - \lambda_{ii} \; P_{n_i \ell_i}(r) - \sum (\text{shells } j, \, j \neq i, \, \ell_j = \ell_i) \; N_j \lambda_{ii} \; P_{n_j \ell_j}(r) \qquad (4.2.8)$$

where

X is the exchange potential given in reference 22b.

N_j is the number of electrons in the jth shell.

λ_{ii} and λ_{ij} are undetermined multipliers.

$$\text{and} \quad Y_k(n_i\ell_i, n_j\ell_j; r) = r \int_0^\infty U^k(r,s)\, P_{n_i\ell_i}(s)\, P_{n_j\ell_j}(s)\, ds \tag{4.2.9}$$

A computer program to solve numerically this system of coupled integro differential equations by the self-consistent field technique has been developed by Froese Fischer (23,24). Approximations to the exchange functions, the Y_k functions, λ_{ii} and λ_{ij} are first derived from initial estimates of the radial functions (e.g. screened hydrogenic). With these as given, equation (4.2.8) is solved to obtain 'improved' radial functions $P_{n_i\ell_i}(r)$ using the initial estimates of the $P_{n_j\ell_j}(r)$ $(j \neq i)$. The whole cycle is repeated (using the latest set of radial functions as the 'initial' estimates) until the results are self-consistent.

The average energies of the following configurations were calculated with the Froese Fischer program

$1s^2\ 2s^2\ 2p^4$

$1s^2\ 2s\ 2p^5$

$1s^2\ 2s\ 2p^4\ np$ for $n = 3$ to 10.

The results of these calculations are given in Table 4.2.1. The program outputs, in addition, the values of the F^k and G^k integrals and these are tabulated in Appendix 3. The input data (23,24) specified

TABLE 4.2.1

The average energy of the configurations

$1s^2\ 2s^2\ 2p^4$, $1s^2\ 2s\ 2p^5$, $1s^2\ 2s\ 2p^4\ np$, n=3,10

Configuration	Average Energy (atomic units)	Average Energy (Rydbergs)
$2s^2\ 2p^4$	-74.7692012	-149.53840
$2s\ 2p^5$	-74.1053093	-148.21061
$2s\ 2p^4$ 3p	-73.7026381	-147.40527
4p	-73.6498424	-147.29968
5p	-73.6302011	-147.26040
6p	-73.6207184	-147.24143
7p	-73.6154165	-147.23083
8p	-73.6121528	-147.22430
9p	-73.6100014	-147.22000
10p	-73.6085085	-147.21701

for the program is given in Appendix 4.

The Froese Fischer program includes provision for calculating configuration interactions i.e. when the wave function for the bound state of an N electron atomic system is expressed in terms of eigenfunctions of L^2 and S^2 belonging to more than one configuration, i.e.

$$u = \sum_{N_c=1}^{\text{Number of configurations}} A_{N_c} U_{N_c}(n_1\ell_1, n_2\ell_2, \ldots, n_N\ell_N, L, S)$$

It cannot however perform a multiconfiguration calculation for the case of interest here, i.e. a bound state in the continuum which interacts most strongly with continuum states.

4.3 Calculation of the matrix elements of the Hamiltonian and the solution of the secular equation

The ${}^3D^o$, ${}^3S^o$ and ${}^3P^o$ terms arising from the configuration $1s^2\ 2s\ 2p^4\ np$ are given in Table 4.3.1. The order of the secular equation which must be solved in each case is equal to the number of terms of each type, i.e. three for ${}^3D^o$, two for ${}^3S^o$ and four for ${}^3P^o$. The matrix elements of the Hamiltonian of equation (4.1.5) with respect to eigenfunctions of L^2, S^2, L_z and S_z with eigenvalues $L = 0,1,2$ $S = 1$, $M_L = 0$, $M_S = 0$ for the configuration $p^4\ p'\ s$ have been tabulated by Slater (22a) and are reproduced in Tables 4.3.2, 4.3.3 and 4.3.4.

Since the electrons are coupled in a different order ($p^4\ p'\ s$ instead of $sp^4\ p'$) the matrix elements of Tables 4.3.2, 4.3.3 and 4.3.4 are calculated with respect to a different complete set of simultaneous eigenstates $u_k^{o'}$ of L^2, S^2, L_z and S_z. This set may also be used to expand a solution of the Schrodinger equation in analogy with equation (4.1.1).

$$u = \sum_k C_k' \ u_k^{o'} \qquad (4.3.1$$

TABLE 4.3.1

Repeated $^3D^o$, $^3S^o$ and $^3P^o$ terms for the configuration $1s^2\ 2s\ 2p^4\ np$

Term of Interest	Identical terms of differing parentage	Order of Secular Equation
$2s\ 2p^4(^4P)np\ ^3D^o$	$2s\ 2p^4(^2P)np\ ^3D^o$	3
	$(^2D)np\ ^3D^o$	
$2s\ 2p^4(^4P)np\ ^3S^o$	$2s\ 2p^4(^2P)np\ ^3S^o$	2
$2s\ 2p^4(^4P)np\ ^3P^o$	$2s\ 2p^4(^2P)np\ ^3P^o$	4
	$(^2S)np\ ^3P^o$	
	$(^2D)np\ ^3P^o$	

The matrix components of the Hamiltonian with respect to the $u_k^{o'}$ are different from those with respect to the u_k^o but the roots of the secular equation are the same in both cases.

The numerical values of the matrix elements (obtained from the F^k and G^k integrals of Appendix 3) are given in Tables 4.3.5, 4.3.6 and 4.3.7, for n=3, 4, 5 and 6. Energy eigenvalues for the $2s\,2p^4$ np $^3D^o$, $^3S^o$ and $^3P^o$ terms produced on the solution of the secular equation are given in Tables 4.3.8, 4.3.9 and 4.3.10. Some of the off diagonal matrix elements were small enough to be ignored and it proved unnecessary to go beyond a quadratic secular equation for the $^3D^o$ and $^3P^o$ terms. Finally, the energy eigenvalues for the $^3D^o$, $^3S^o$ and $^3P^o$ terms with the ^4P parent are given in Table 4.3.11. The calculated energy differences between the three terms for each of the configurations np, n=3 to 6 are also given.

TABLE 4.3.2

Hamiltonian matrix elements between eigenfunctions of L^2 and S^2 $(M_L=0,\ M_S=0)$ $p^4\ p's\ {}^3D^o$

	$p^4(^3P)p'(^4D^o)s\ {}^3D^o$	$p^4(^3P)p'(^2D^o)s\ {}^3D^o$	$p^4(^1D)p'(^2D^o)s\ {}^3D^o$
	A	B	C
A	a_{11}	a_{12}	a_{13}
B	a_{21}	a_{22}	a_{23}
C	a_{31}	a_{32}	a_{33}

where

$$a_{11} = -\frac{3}{25}F^2(p,p) + \frac{F^2}{25}(p,p') - \frac{G^0}{3}(p,p') - \frac{2}{15}G^2(p,p') + \frac{5}{9}G^1(s,p) + \frac{5}{18}G^1(s,p')$$

$$a_{22} = -\frac{3}{25}F^2(p,p) + \frac{F^2}{25}(p,p') - \frac{G^0}{3}(p,p') + \frac{61}{150}G^2(p,p') - \frac{2}{9}G^1(s,p) + \frac{1}{18}G^1(s,p')$$

$$a_{33} = \frac{3}{25}F^2(p,p) + \frac{7}{25}F^2(p,p') - \frac{G^0}{3}(p,p') - \frac{11}{150}G^2(p,p') - \frac{G^1}{6}(s,p')$$

$$a_{12} = a_{21} = \frac{\sqrt{8}}{9}G^1(s,p) - \frac{\sqrt{8}}{9}G^1(s,p')$$

$$a_{23} = a_{32} = -\frac{9\sqrt{6}}{150}G^2(p,p')$$

$$a_{13} = a_{31} = 0$$

TABLE 4.3.3

Hamiltonian matrix elements between eigenfunctions of L^2 and S^2 ($M_L=0$, $M_S=0$) $p^4\,p'\,s\ {}^3S^o$

	$p^4({}^3P)p'({}^4S^o)s\ {}^3S^o$	$p^4({}^3P)p'({}^2S^o)s\ {}^3S^o$
	A	B
A	a_{11}	a_{12}
B	a_{21}	a_{22}

where

$$a_{11} = -\frac{3}{25}F^2(p,p) + \frac{2}{5}F^2(p,p') - \frac{1}{3}G^0(p,p') - \frac{2}{15}G^2(p,p') + \frac{5}{9}G^1(s,p) + \frac{5}{18}G^1(s,p')$$

$$a_{22} = -\frac{3}{25}F^2(p,p) + \frac{2}{5}F^2(p,p') - \frac{1}{3}G^0(p,p') - \frac{2}{15}G^2(p,p') - \frac{2}{9}G^1(s,p) + \frac{1}{18}G^1(s,p')$$

$$a_{12} = a_{21} = \frac{\sqrt{8}}{9}\,G^1(s,p) - \frac{\sqrt{8}}{9}\,G^1(s,p')$$

TABLE 4.3.4

Hamiltonian matrix elements between eigenfunctions of L^2 and S^2 $(M_L=0,\ M_S=0)$ $p^4\ p's\ ^3P^o$

	$p^4(^3P)p'(^4P^o)s\ ^3P^o$	$p^4(^3P)p'(^2P^o)s\ ^3P^o$	$p^4(^1D)p'(^2P^o)s\ ^3P^o$	$p^4(^1S)p'(^2P^o)s\ ^3P^o$
	A	B	C	D
A	a_{11}	a_{12}	a_{13}	a_{14}
B	a_{21}	a_{22}	a_{23}	a_{24}
C	a_{31}	a_{32}	a_{33}	a_{34}
D	a_{41}	a_{42}	a_{43}	a_{44}

where

$$a_{11} = \frac{-3}{25} F^2(p,p) - \frac{F^2}{5}(p,p') - \frac{G^0}{3}(p,p') - \frac{2}{15} G^2(p,p') + \frac{5}{9} G^1(s,p) + \frac{5}{18} G^1(s,p')$$

$$a_{22} = -\frac{3}{25} F^2(p,p) - \frac{F^2}{5}(p,p') + \frac{16}{6} G^0(p,p') + \frac{G^2}{6}(p,p') - \frac{2}{9} G^1(s,p) + \frac{1}{18} G^1(s,p')$$

$$a_{33} = \frac{3}{25} F^2(p,p) - \frac{7}{25} F^2(p,p') + \frac{4}{3} G^0(p,p') - \frac{19}{150} G^2(p,p') - \frac{1}{6} G^1(s,p')$$

$$a_{44} = \frac{12}{25} F^2(p,p) - \frac{G^1}{6}(s,p')$$

$$a_{12} = a_{21} = \frac{\sqrt{8}}{9} G^1(s,p) - \frac{\sqrt{8}}{9} G^1(s,p')$$

$$a_{23} = a_{32} = \sqrt{5}\ G^0(p,p') - 3\frac{\sqrt{5}}{150} G^2(p,p')$$

$$a_{24} = a_{42} = G^0(p,p') - \frac{G^2}{5}(p,p')$$

$$a_{13} = a_{31} = 0$$

$$a_{14} = a_{41} = 0$$

TABLE 4.3.5

Hamiltonian matrix elements between eigenfunctions of L^2 and S^2 ($M_L=0,M_S=0$) $2p^4\ np'\ 2s\ {}^3D^o$, n=3,..,6

	$p^4({}^3P)p'({}^4D^o)s\ {}^3D^o$	$p^4({}^3P)p'({}^2D^o)s\ {}^3D^o$	$p^4({}^1D)p'({}^2D^o)s\ {}^3D^o$
	A	B	C
A	$a_{11}=$	$a_{12}=$	$a_{13}=0$
n=3	2.3797803 10^{-1}	1.5921455 10^{-1}	
n=4	2.3816988 10^{-1}	1.6002112 10^{-1}	
n=5	2.3824262 10^{-1}	1.6024717 10^{-1}	
n=6	2.3827330 10^{-1}	1.6033441 10^{-1}	
B	$a_{21} = a_{12}$	$a_{22} =$	$a_{23} =$
n=3		-1.5766502 10^{-1}	-5.7926513 10^{-4}
n=4		-1.5838974 10^{-1}	-1.9785018 10^{-4}
n=5		-1.5858591 10^{-1}	-8.9812990 10^{-5}
n=6		-1.5866040 10^{-1}	-4.8073685 10^{-5}
C	$a_{31} = 0$	$a_{32} = a_{23}$	a_{33}
n=3			4.7295092 10^{-2}
n=4			4.5804235 10^{-2}
n=5			4.5502692 10^{-2}
n=6			4.5402192 10^{-2}

TABLE 4.3.6

Hamiltonian matrix elements between eigenfunctions of L^2 and S^2 ($M_L=0$, $M_S=0$) $2p^4$ np' 2s $^3S^o$, n=3,...,6.

	$p^4(^3P)p'(^4S^o)s\ ^3S^o$	$p^4(^3P)p'(^4S^o)s\ ^3S^o$
	A	B
A	a_{11} =	a_{12} =
n=3	2.4347897 10^{-1}	1.5921455 10^{-1}
n=4	2.3980579 10^{-1}	1.6002112 10^{-1}
n=5	2.3894959 10^{-1}	1.6024717 10^{-1}
n=6	2.3864291 10^{-1}	1.6033441 10^{-1}
B	$a_{21} = a_{12}$	a_{22}
n=3		-1.5429243 10^{-1}
n=4		-1.5748078 10^{-1}
n=5		-1.5820893 10^{-1}
n=6		-1.5846742 10^{-1}

TABLE 4.3.7

Hamiltonian matrix elements between eigenfunctions of L^2 and S^2 ($M_L=0$, $M_S=0$) $2p^4\ np'\ 2s\ ^3P^o$, n=3,...,6.

	$p^4(^3P)p'(^4P^o)s\,^3P^o$	$p^4(^3P)p'(^2P^o)s\,^3P^o$	$p^4(^1D)p'(^2P^o)s\,^3P^o$	$p^4(^1S)p'(^2P^o)s\,^3P^o$
	A	B	C	D
A	a_{11} =	a_{12} =	a_{13} = 0	a_{14} = 0
n=3	$2.3431073\ 10^{-1}$	$1.5921455\ 10^{-1}$		
n=4	$2.3707927\ 10^{-1}$	$1.6002112\ 10^{-1}$		
n=5	$2.3777131\ 10^{-1}$	$1.6024717\ 10^{-1}$		
n=6	$2.3802689\ 10^{-1}$	$1.6033441\ 10^{-1}$		
B	$a_{21} = a_{12}$	a_{22} =	a_{23} =	a_{24} =
n=3		$-1.4991855\ 10^{-1}$	$9.0361116\ 10^{-3}$	$3.3316200\ 10^{-3}$
n=4		$-1.5567154\ 10^{-1}$	$3.0195325\ 10^{-3}$	$1.1080600\ 10^{-3}$
n=5		$-1.5733878\ 10^{-1}$	$1.4174926\ 10^{-3}$	$4.9948000\ 10^{-4}$
n=6		$-1.5798961\ 10^{-1}$	$7.2752260\ 10^{-4}$	$2.6648000\ 10^{-4}$
C	a_{31}= 0	$a_{32} = a_{23}$	a_{33} =	a_{34} =
n=3			$4.5394360\ 10^{-2}$	$-2.2785801\ 10^{-3}$
n=4			$4.5483187\ 10^{-2}$	$-5.5906767\ 10^{-4}$
n=5			$4.5406539\ 10^{-2}$	$-2.2098314\ 10^{-4}$
n=6			$4.5362961\ 10^{-2}$	$-1.1018746\ 10^{-4}$
D	a_{41} = 0	$a_{42} = a_{24}$	$a_{43} = a_{34}$	a_{44} =
n=3				$1.8058341\ 10^{-1}$
n=4				$1.8098597\ 10^{-1}$
n=5				$1.8110300\ 10^{-1}$
n=6				$1.8114879\ 10^{-1}$

TABLE 4.3.8

Energy eigenvalues for the terms $1s^2\ 2s\ 2p^4(^{2Sp+1}Lp)np\ ^3D^o$

Configuration and parent term	Energy relative to the average energy of the configuration (atomic units)	Energy (atomic units)	ΔE Energy relative to 0 I ground state 3p (atomic units)	ΔE (cm^{-1})	ΔE (Å)
$(^2P)3p$	2.9409080 10^{-1}	-73.408547	1.4007210	307412.17	325.29615
$(^4P)3p$	-2.1377779 10^{-1}	-73.916415	0.89285300	195951.85	510.32942
$(^2D)3p$	4.7295092 10^{-2}	-73.655343	1.1539249	253248.57	394.86896
$(^2P)4p$	2.9468732 10^{-1}	-73.355155	1.4541129	319129.96	313.35196
$(^4P)4p$	-2.1490718 10^{-1}	-73.864749	0.94451842	207290.84	482.41397
$(^2D)4p$	4.5804235 10^{-2}	-73.604038	1.2052298	264508.29	378.05997
$(^2P)5p$	2.9487222 10^{-1}	-73.335328	1.4739391	323481.33	309.13684
$(^4P)5p$	-2.1521551 10^{-1}	-73.845416	0.96385200	211533.80	472.73768
$(^2D)5p$	4.5502692 10^{-2}	-73.584698	1.2245696	268752.75	372.0892
$(^2P)6p$	2.9494604 10^{-1}	-73.325772	1.4834956	325578.56	307.14552
$(^4P)6p$	-2.1533314 10^{-1}	-73.836051	0.97321646	213589.11	468.118865
$(^2D)6p$	4.5402192 10^{-2}	-73.575316	1.2339517	270811.82	369.26009

TABLE 4.3.9

Energy eigenvalues for the terms $1s^2\ 2s\ 2p^4(^{2Sp+1}Lp)np\ ^3S^o$

Configuration and parent term	Energy relative to the average energy of the configuration (atomic units)	Energy (atomic units)	$\triangle$ E Energy relative to O I ground state 3p (atomic units)	$\triangle$ E (cm^{-1})	$\triangle$ E (Å)
$(^2P)3p$	$2.9935746\ 10^{-1}$	-73.403280	1.4059873	308569.10	324.07756
$(^4P)3p$	$-2.1017092\ 10^{-1}$	-73.912809	0.89645898	196743.25	508.27663
$(^2P)4p$	$2.9624271\ 10^{-1}$	-73.353599	1.4556687	319471.45	313.01701
$(^4P)4p$	$-2.1391770\ 10^{-1}$	-73.863760	0.94550831	207507.89	481.90936
$(^2P)5p$	$2.9554258\ 10^{-1}$	-73.334658	1.4746094	323628.38	308.99638
$(^4P)5p$	$-2.1480192\ 10^{-1}$	-73.845003	0.96426498	211624.44	472.53520
$(^2P)6p$	$2.9529604\ 10^{-1}$	-73.325422	1.4838456	325655.37	307.07307
$(^4P)6p$	$-2.1512055\ 10^{-1}$	-73.835838	0.97342905	213635.85	468.08621

TABLE 4.3.10

Energy eigenvalues for the terms $1s^2\ 2s\ 2p^4(^{2Sp+1}Lp)np\ ^3P^o$

Configuration and parent term	Energy relative to the average energy of the configuration (atomic units)	Energy (atomic units)	△E Energy relative to O I ground state 3p (atomic units)	△E (cm^{-1})	△E (Å)
$(^2P)3p$	2.9171023 10^{-1}	-73.410927	1.3983405	306889.84	325.84981
$(^4P)3p$	-2.0731805 10^{-1}	-73.909956	0.89931226	197369.39	506.66416
$(^2D)3p$	4.5394360 10^{-2}	-73.657243	1.1520246	252831.58	395.52020
$(^2S)3p$	1.8058341 10^{-1}	-73.522654	1.2872137	282501.12	353.98089
$(^2P)4p$	2.9402196 10^{-1}	-73.355820	1.4534479	318984.01	313.49533
$(^4P)4p$	-2.1261423 10^{-1}	-73.862456	0.94681178	207794.08	481.24565
$(^2D)4p$	4.5483187 10^{-2}	-73.604359	1.2049092	264437.88	378.16064
$(^2S)4p$	1.8098597 10^{-1}	-73.468856	1.3404119	294176.33	339.93217
$(^2P)5p$	2.9459226 10^{-1}	-73.335608	1.4736591	323419.88	309.19558
$(^4P)5p$	-2.1415973 10^{-1}	-73.844360	0.96490717	211765.56	472.22031
$(^2D)5p$	4.5406539 10^{-2}	-73.584794	1.2244740	268731.75	372.11828
$(^2S)5p$	1.8110300 10^{-1}	-73.449098	1.3601699	298512.56	334.99427
$(^2P)6p$	2.9480166 10^{-1}	-73.325916	1.4833512	325546.96	307.17534
$(^4P)6p$	-2.1476438 10^{-1}	-73.835482	0.97378522	213713.98	467.91508
$(^2D)6p$	4.5362961 10^{-1}	-73.575355	1.2339180	270803.30	369.27170
$(^2S)6p$	1.8114879 10^{-1}	-73.439569	1.3696983	300603.86	332.66371

TABLE 4.3.11

Energy eigenvalues for the terms

$1s^2\ 2s\ 2p^4(^4P)np\ ^3D^o, ^3S^o, ^3P^o\quad n=3,6$

Configuration	Term	Energy (atomic units, relative to average energy of configuration)	Energy difference from $^3D^o$ (atomic units)	Energy difference from $^3D^o$ (cm^{-1})
3p	$^3D^o$	$-2.1377779\ 10^{-1}$		
3p	$^3S^o$	$-2.1017092\ 10^{-1}$	$3.6068700\ 10^{-3}$	791.58929
3p	$^3P^o$	$-2.0731805\ 10^{-1}$	$6.4597400\ 10^{-3}$	1417.7004
4p	$^3D^o$	$-2.1490718\ 10^{-1}$		
4p	$^3S^o$	$-2.1391770\ 10^{-1}$	$9.8948000\ 10^{-4}$	217.15830
4p	$^3P^o$	$-2.1261423\ 10^{-1}$	$2.2929500\ 10^{-3}$	503.22708
5p	$^3D^o$	$-2.1521551\ 10^{-1}$		
5p	$^3S^o$	$-2.1480192\ 10^{-1}$	$4.1359000\ 10^{-4}$	90.769397
5p	$^3P^o$	$-2.1415973\ 10^{-1}$	$1.0557800\ 10^{-3}$	231.70897
6p	$^3D^o$	$-2.1533314\ 10^{-1}$		
6p	$^3S^o$	$-2.1512055\ 10^{-1}$	$2.1259000\ 10^{-4}$	46.656510
6p	$^3P^o$	$-2.1476438\ 10^{-1}$	$5.6876000\ 10^{-4}$	124.82410

CHAPTER V

THE RADIOFREQUENCY DISCHARGE IN NITROGEN

5.1 Introduction

In the first three chapters of this thesis an experiment carried out to obtain the absorption spectrum of atomic oxygen in the wavelength region below 600 Å has been described. Nitrogen is another element of astrophysical interest not stable in the laboratory in atomic form. Our knowledge of its energy levels is derived mainly from the study of emission spectra. States arising from the excitation of an inner electron are difficult to observe in emission since lying as they do above the first ionization limit, they are frequently subject to strong autoionization as a result of interaction with states in the continuum. Transitions to such levels will take place by absorption but little work has been reported to date on photoabsorption by atomic nitrogen above the first ionization potential. This is due to the problem of creating and containing a pure sample of atomic nitrogen of sufficient integrated number density.

In 1966, Carroll, Huffman, Larrabee and Tanaka (26) photographed between 1000 and 600 Å the absorption spectrum of a microwave electrodeless discharge through a mixture consisting of 98% helium and 2% molecular nitrogen. A Rydberg series was observed in the region 694 Å to 612 Å which was completely absent in the absorption spectrum of ordinary molecular nitrogen. Twelve members of the series were observed and yielded a convergence limit of 164012 cm^{-1}, 609.71 Å. The authors attributed the spectrum to transitions from the $1s^2\ 2s^2 2p^3\ {}^4S^o_{3/2}$ ground state of the nitrogen atom to the Rydberg terms $1s^2\ 2s\ 2p^3({}^5S^o)np\ {}^4P$. As a result of autoionization all of the lines were broadened and showed an asymmetric structure. On the short wavelength side of each line the photoabsorption cross section was lower than on the long wavelength side producing an apparent enhancement of the background continuum intensity. In the experiment, atomic nitrogen was produced in a quartz tube 50 cm long and 14 mm in diameter. The helium Hopfield continuum served as the background light source.

In this investigation, interest turned to discovering whether pure atomic nitrogen could be created in a radiofrequency discharge. If successful, the absorption spectrum could be photographed at wavelengths shorter than the He II $^2S_{1/2}$ limit at 504 Å. A description of the experimental work on nitrogen is given in the next section, with the discussion on the results following in Section 5.3.

5.2 Experimental

The apparatus described in Chapter II was used to photograph the absorption spectrum of an electrodeless radiofrequency discharge through pure molecular nitrogen. The spectrum was obtained with the short discharge tube of length 30 cms and diameter 10 cms. Two auxiliary quartz tubes incorporated to facilitate variation of the absorption path length were drawn out to their fullest extent so that approximately 26 cms of absorbant was available. The induction coil configuration was the same as before with a coil of total length 25 cms and 5 cm spacing between turns. Nitrogen was found to discharge uniformly at higher pressures (measured before the radiofrequency oscillator was switched on) than had been achievable with oxygen. The optimum cell filling pressure was determined empirically by observing when the strength of the atomic absorption was greatest and the intensity of molecular structure superimposed on the spectrum least (see Section 5.3). This was 0.8 torr (discharge off). If the pressure were raised above this, the bright pink discharge in the tube faded rapidly.

The following spectra were recorded on each piece of film:

a) The absorption spectrum of the discharge.

b) The emission spectrum of the BRV continuum source (with the absorption cell evacuated).

c) Absorption spectra of molecular nitrogen taken with three different cell filling pressures 0.8, 0.4 and 0.1 torr.

In each case the number of shots required from the B.R.V. source had to be adjusted empirically to produce an optimum exposure. This was 1000 for the spectrum of the discharge. The dispersing instrument was the 1 metre normal incidence Jobin Yvon vacuum spectrograph described in Section 2.6 with a slit width of approximately 20 microns. All spectra were recorded on Kodak 101-01 film over the full range of the system, which was from 1350 Å to approximately 350 Å.

Attempts were also made to photograph the spectrum with the second discharge tube of length 100 cms and diameter 6 cms filled with nitrogen. The endplates described in Section 2.4 and illustrated in Figure 2.4.3 were in fact the second set constructed for the tube. The design of the first set was similar, the main difference being that the endplates were not made from one piece of brass. The short cylindrical section protruding 2 to 3 cms into the discharge tube and the disc with the 2 mm orifice in the centre had been manufactured from stainless steel in the first version. These were then silver soldered to the brass water jacket which comprised the remainder of the endplate flange as illustrated in Figure 5.2.1. It had been hoped that with its very high melting point the stainless steel would withstand any thermal attack from the discharge or heating by eddy currents induced by the radio-frequency oscillator.

This system worked satisfactorily when the discharge was being run in oxygen. With nitrogen, however, the stainless steel discs on

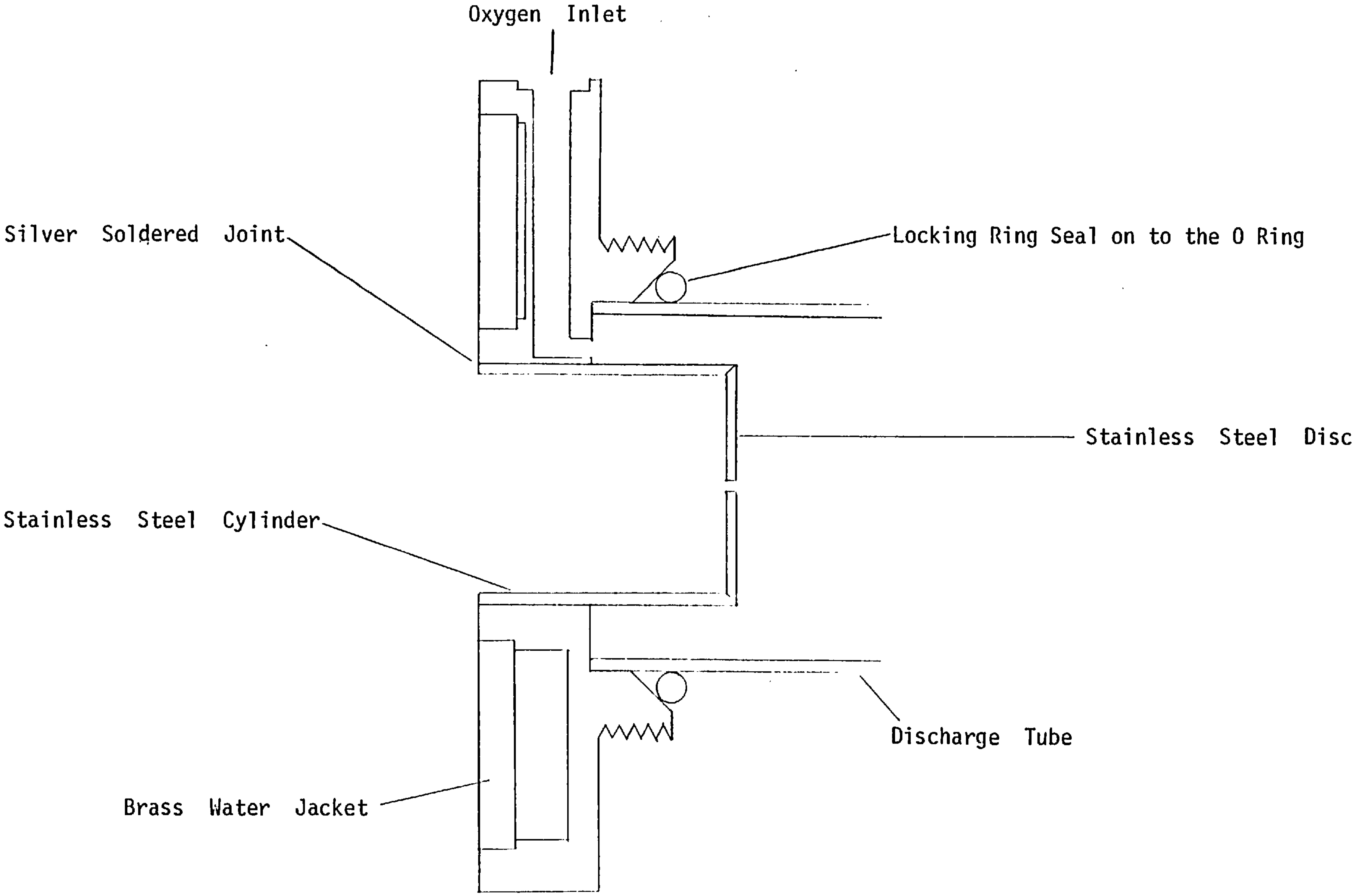

FIGURE 5.2.1 - 100 cm Tube Endplates (Version I)

the endplates rapidly became red hot. After two or three minutes the orifice on one of the endplates moved a few millimetres across the face of the disc as the metal melted on one side of the hole and cooled on the other. Meanwhile the interior surface of the quartz tube rapidly became coated in a slate grey deposit at each end. At the end at which the stainless steel was melting the quartz became locally very hot and extensive thermal damage to the Viton O ring was later found to have taken place. This was, incidentally, the only occasion in these experiments on which the O rings incurred any damage. The Viton material, offering improved thermal stability up to temperatures of 200 ^oC, withstood surprisingly well an often very hot quartz tube.

The rapid thermal damage to the system in fact occurred when the discharge became very bright near the 2 mm holes. After this attempt, the endplates for the 100 cm tube had to be rebuilt and were designed to be constructed from one piece of brass with no stainless steel components or soldered surfaces exposed to the discharge. This was the second version of the endplates described in Section 2.4. No further attempts were made to run the radiofrequency discharge in nitrogen using the 100 cm tube which continued to operate satisfactorily during further experiments with oxygen. With the 30 cm discharge tube the quartz on the auxiliary sliding tubes also quickly became red hot near the orifices but survived long enough for spectra to be taken.

5.3 Results and discussion

Plate 5.3.1 gives a photograph of the absorption spectrum of the radiofrequency discharge in nitrogen from 1000 Å to approximately 690 Å. Plate 5.3.2 shows the spectrum from 700 Å to 350 Å. Also shown on the plates are (a) the emission spectrum of the B.R.V. continuum source obtained with an absorption tube completely evacuated and (b) the absorption spectrum of molecular nitrogen taken at pressures of 0.8, 0.4 and 0.1 torr for Plate 5.3.1 and 0.4 torr for Plate 5.3.2. All the photographs are positive prints and therefore black denotes absorption.

It can be seen from Plate 5.3.1 that from 1000 to 660 Å the usual (27) band structure of molecular nitrogen appeared with considerable intensity on the spectrum of the discharge. For example, the series converging onto the $B\ {}^2\Sigma_u^+$ state of N_2^+ at 661.23 Å observed by Hopfield (28) can be distinguished although the intensity of absorption is less than on the molecular spectra taken at pressures of 0.8 torr and 0.4 torr. The discharge spectrum was modified, in addition, by the appearance of bands probably arising from transitions between excited vibrational levels of the ground state and the various known states in the energy range above 12 eV. At lower wavelengths, the absorption spectrum of molecular nitrogen was first studied in the 600 Å to 100 Å wavelength region by Codling (29) utilizing the continuum radiated by an 180 MeV electron synchrotron as a background light source. Discrete structure was observed only in the 570 Å to 470 Å region and appeared to correspond to a single state of neutral N_2 having vibrational spacings very similar to those of the known $C\ {}^2\Sigma_u^+$ state of N_2^+. This structure can be seen on the molecular spectrum of Plate 5.3.2. The transitions are much weaker on the discharge spectrum and indeed many are indistinguishable.

On the spectrum of the radiofrequency discharge in nitrogen the members of the atomic Rydberg series in the region 694 Å to 612 Å reported by Carroll et al. (26) from n=3 to n=8 can be observed. These correspond to transitions from the $1s^2\ 2s^2\ 2p^3\ {}^4S^o_{3/2}$ ground state of the nitrogen atom to the terms $1s^2\ 2s\ 2p^3({}^5S^o)np\ {}^4P$. The series, marked with vertical lines below the spectrum, is weak and is superimposed on a strong absorption continuum. A considerable degree of dissociation must therefore have been accomplished by the radiofrequency

KEY 1 to 3 MOLECULAR NITROGEN 4 RADIOFREQUENCY DISCHARGE 5 BRV CONTINUUM SOURCE

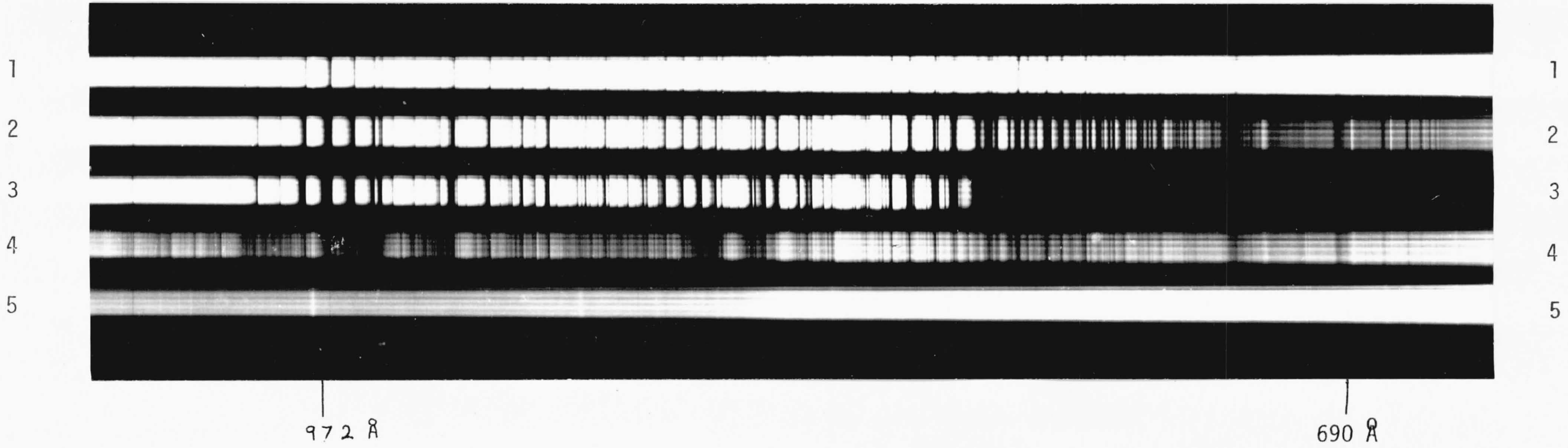

PLATE 5.3.1

THE ABSORPTION SPECTRUM OF NITROGEN 1000 Å to 690 Å

KEY 1 BRV CONTINUUM SOURCE 2 MOLECULAR NITROGEN 3 RADIOFREQUENCY DISCHARGE

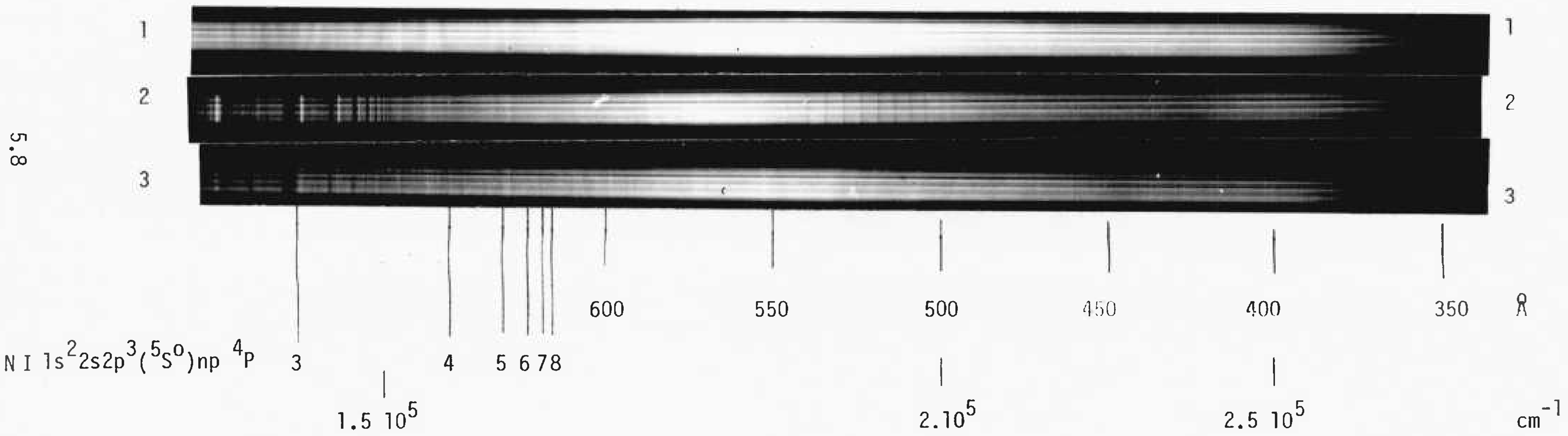

PLATE 5.3.2

THE ABSORPTION SPECTRUM OF NITROGEN 700 Å to 350 Å discharge and substantial quantities of atomic nitrogen must have been produced. This was achieved in spite of the fact that the absorption cell contained pure nitrogen (i.e. with no added helium).

The allowed absorption series (from the ground state of N I) involving the excitation of an inner subshell 2s electron which are predicted to lie in the wavelength region from 600 to 350 Å are given in Table 5.3.1. The spin selection rule $\triangle S = 0$ should be obeyed for nitrogen since the spin-orbit interaction should not be sufficiently strong in such a light atom to permit the observation of intercombination transitions. The possible transitions from the N I $^4S^o$ ground state are further reduced by the selection rules $\triangle \ell = \pm 1$, $\triangle L = 0, \pm 1$ to the term series given in Table 5.3.1.

Although the region of observation was extended in this experiment from 600 Å to approximately 350 Å it is extremely difficult positively to identify any new structure present on the spectrum of the discharge which does not occur in that of the background light source or that of molecular nitrogen. The process is made harder by the fact that, towards the lower wavelength limit of the apparatus, the quality of the B.R.V. source continuum deteriorates with many emission lines superimposed.

TABLE 5.3.1

Summary of the atomic nitrogen series resulting from the excitation of a 2s electron from the ground state

$1s^2\ 2s^2\ 2p^3\ {}^4S^o_{3/2}$

N II Term	Approximate term value$^{(1)}$ from ground state (cm^{-1})		Convergence limit (1) (Å)	N I Series
$2s2p^3(^3D^o)$	$^3D^o_3$	209582.90	477.14	$2s2p^3(^3D^o)np\ ^4P$
	$^3D^o_2$	209596.30	477.11	
	$^3D^o_1$	209597.90	477.10	
$2s2p^3(^3P^o)$	$^3P_{2,1}$	226563.20	441.38	$2s2p^3(^3P^o)np\ ^4P$
	^3P_o	226569.80	441.37	
$2s2p^3(^3S^o)$	$^3S_1$	272474.90	367.01	$2s2p^3(^3S^o)np\ ^4P$

1. The series limits were computed from the sum of measured transitions from the N II ground state $2p^2\ {}^3P_o$ (reference 13) and the value of the limit N I $2p^3\ {}^4S^o_{3/2}$ to N II $2p^2\ {}^3P_o$ (reference 13).

PART II - MEASUREMENTS OF THE RELATIVE PHOTOABSORPTION CROSS SECTION OF ATOMIC OXYGEN IN THE EXTREME VACUUM ULTRAVIOLET

CHAPTER VI

EXPERIMENTAL

6.1 Introduction

When light passes through an absorbing gas column of length ℓ, the relation between the incident and the transmitted intensities is given by the Lambert Beer formula, i.e.

$$I_\nu(\ell) = I_\nu(o) \exp(-\sigma_\nu N) \qquad (6.1.1)$$

where

$$N = \int_o^\ell N(x)\,dx \qquad (6.1.2)$$

is the integrated number density and σ_ν the photoabsorption cross section of the atom at the wavenumber ν. Measurements are required of two quantities in order to assign values to the cross section - firstly the ratio of the two intensities $\frac{I_\nu(\ell)}{I_\nu(o)}$ and secondly the integrated number density N. In practice, for an unstable absorbant contained in a windowless system, N is often harder to obtain than $\frac{I_\nu(\ell)}{I_\nu(o)}$.

If the absolute photoabsorption cross section, σ_{ν_i}, at one or any number of frequencies, ν_i, is known, the cross sections at different frequencies, σ_{ν_j}, can be expressed relative to them by measurement of $I_\nu(\ell)/I_\nu(o)$ for all ν_i and ν_j. The integrated number density must be constant during the measurement of the intensity ratios but knowledge of its absolute value is not required. The photoabsorption cross section data, both absolute and relative, which has been obtained to date on atomic oxygen at wavelengths shorter than 1050 Å was outlined in Chapter I. To remind the reader, there have been three reports (1,2,3) of absolute cross section measurements at a number of wavelengths down to 450 Å. The continuous relative photoionization cross section curve has also been obtained between 920 and 650 Å (6). The curve may be regarded as equivalent to the photoabsorption cross section curve except at the wavelengths of transitions for which autoionization is Russell-Saunders forbidden (and which were observed in emission in reference 4).

This chapter describes an experiment to obtain the relative photoabsorption cross section at wavelengths between 830 and 430 Å. The overlap with the region in which absolute data is available permits the new relative values between 650 and 430 Å to be set onto an absolute scale. The measurement of the ratio of the transmitted intensity to the intensity incident on the absorbing gas column $\frac{I_\nu(\ell)}{I_\nu(0)}$ using photographic photometry is described in Section 6.2 and this is followed by an account of the experiments in Section 6.3.

6.2 Measurement of the intensity ratio $\frac{I_\nu(\ell)}{I_\nu(0)}$ by photographic photometry

The response of a photographic emulsion to light is shown in Figure 6.2.1 where the 'density' d is plotted against the logarithm of the intensity of the light to which the emulsion was exposed for a constant time. d is defined as $\log_{10} \frac{1}{T}$ where T is the ratio of the intensity of light incident on the developed emulsion to the intensity of light transmitted through it. It is T that is measured when the plate is scanned with a microdensitometer. A curve rather similar to that of Figure 6.2.1 is obtained if d is plotted against the logarithm of the exposure time t for constant I. The curves are not necessarily exactly the same shape since the 'reciprocity' law between intensity and exposure does not usually strictly hold. Simultaneous doubling of the intensity and halving of the exposure time may not result in the same plate blackening. This 'reciprocity failure' is a consequence of the fact that the sensitivity of an emulsion is a function of both the total number of photons and their rate of arrival which is a feature of the multi-stage processes by which a single grain of emulsion is blackened.

Many factors influence the response of an emulsion and so, if accurate intensity measurements are to be made photographically, a response curve must be plotted for each individual plate. This may be done by making a number of exposures of known intensity ratio with the same exposure time and at the same wavelength. It is not, in general, safe to keep I constant and vary t unless the reciprocity law has been found to hold for the emulsion concerned. The procedure is illustrated in Figure 6.2.2 where the horizontal axis is set to a relative scale and the calibration exposures marked by dots have been used to construct a response curve. The values of two unknown intensities relative to the calibration intensities can be read off the curve for the two unknown exposures and hence their ratio may be determined.

Characteristic curves and absolute sensitivity data for the Kodak 101-01 emulsion have been reported by Burton, Hatter and Ridgeley(30). A comparison was made between the response of a calibrated detector and the response of the film to constant ultraviolet irradiance. In the detector, a tungsten photocathode was used as a secondary standard for the 500 Å to 1200 Å wavelength range and a calibrated sodium salicylate

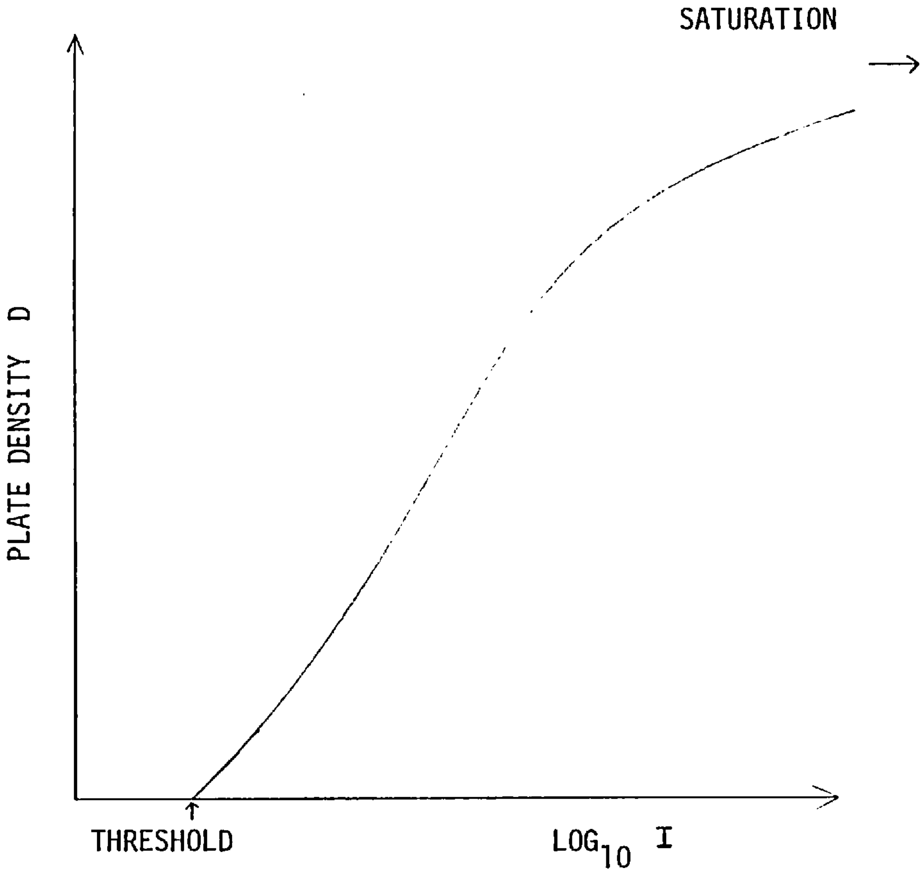

FIGURE 6.2.1

THE TYPICAL RESPONSE CURVE OF A PHOTOGRAPHIC EMULSION-CONSTANT EXPOSURE TIME

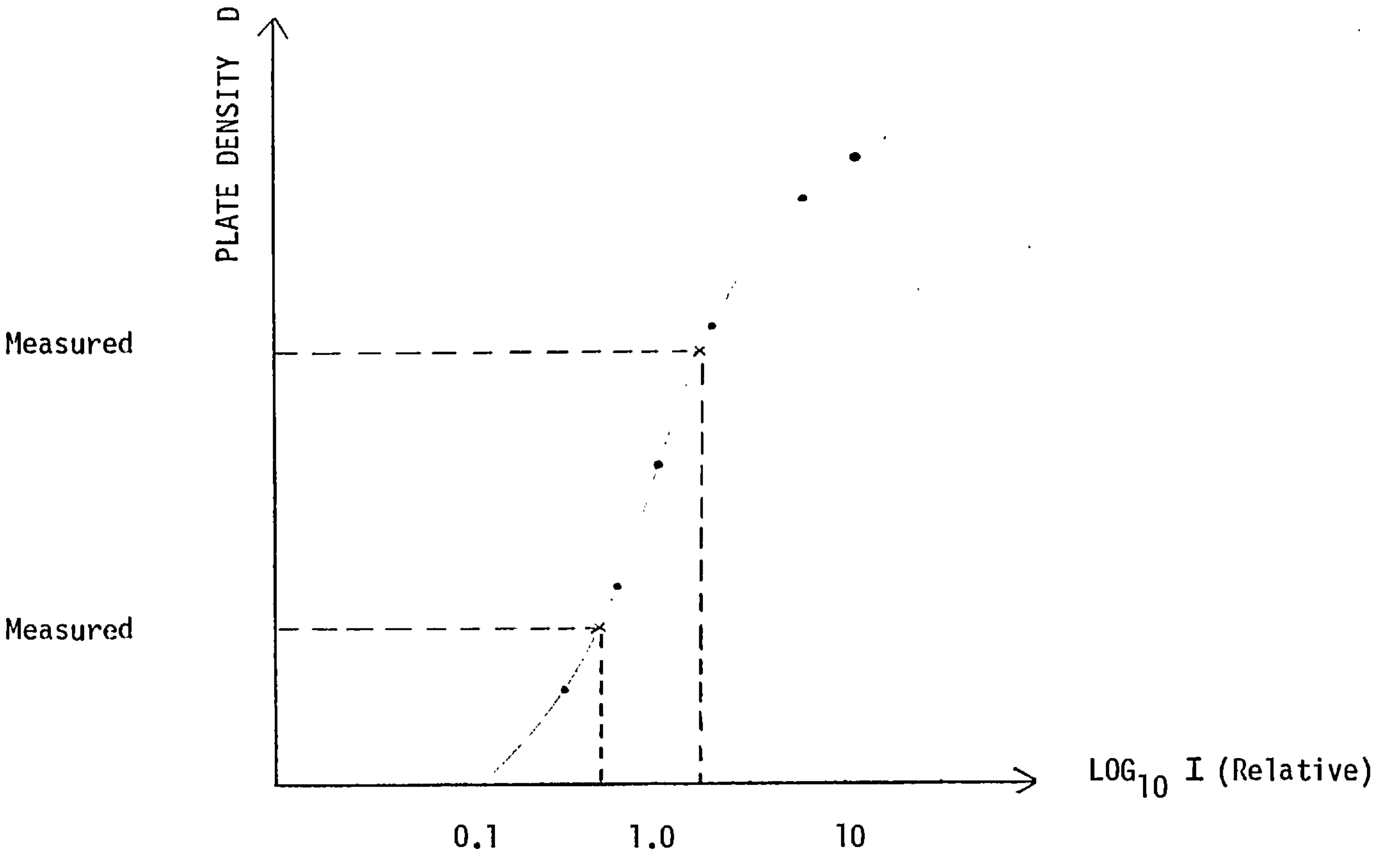

FIGURE 6.2.2

THE DEDUCTION OF AN UNKNOWN INTENSITY RATIO FROM THE RESPONSE CURVE coated photodiode served as a standard in the 1200 Å to 3000 Å region. A 2.5 GHz microwave discharge in inert gas-air mixtures was employed as the light source. The density-intensity of light response curve of the film was first obtained by using a fixed exposure time and varying the intensity between exposures. This was achieved either by changing the power input to the light source or by changing the width of the monochromator entrance and exit slits. Then, a series of exposures were made with constant intensity of illumination and different exposure times ranging from one second to 120 seconds. Time-varied and intensity-varied curves obtained by these two procedures were then compared to evaluate reciprocity effects. The authors discovered that the curves obtained by variation of intensity and exposure time were effectively identical at wavelengths shorter than 1750 Å. They concluded that reciprocity effects were not significant within the accuracy of the measurements which was estimated to be ±10%. This was also found to be true for two other emulsions studied - the Kodak-Pathe SC5 and SC7 films.

The reciprocity behaviour of the 101-01 emulsion is relevant to this experiment since it proved difficult to calibrate the plates by taking intensity varied exposures of constant time. The optical layout of the system was such that several hundred shots of the BRV continuum source were required to produce an exposure in the linear region of the response curve (with an evacuated system). Since the calibration had to be performed using one set of source electrodes, the number of shots available for calibration was limited to about 1800. The use of calibrated attenuators such as grids or a variable slit was not possible because insufficient calibration points would have been available to construct an accurate response curve. A stepped slit could not be used since the height of the exposed part of the emulsion for a normal slit was only about 5 mm.

Due to these difficulties the plates for this experiment were calibrated using time varied exposures. This was achieved by taking a number of continuum spectra using the BRV source (with an evacuated system), varying the number of times the source was fired. Assuming that enough shots are used each time to average out the flash to flash variation of intensity produced by the source, but that the total number of calibration shots is within the working range of one set of electrodes, this is equivalent to time varied exposures of constant intensity.

The pulse length of the ultraviolet radiation from the BRV source is about 1 μs which is six orders of magnitude less than the times investigated in reference 30. Although the results of Burton et al. offer some degree of encouragement, there is no data available on the reciprocity behaviour of the Kodak 101-01 for very short exposure times. In this experiment it was assumed that reciprocity effects were not significant. The author is aware that this assumption is an extrapolation of the results of reference 30 and this must be reflected in the uncertainty in the results.

6.3 Experimental runs to obtain the photoabsorption cross section

The apparatus described in Chapter II was used to measure the relative photoabsorption cross section of atomic oxygen continuously from 830 Å to 430 Å. Measurements were taken using the 100 cm long, 6 cm diameter quartz discharge tube filled to a pressure of 8.10^{-2} torr (measured before the discharge was initiated). The radiofrequency induction coil configuration was the same as before with a 5 cm spacing between turns and an extension over the full length of the tube. The slit width used was approximately 20 microns (0.08 Å). On each plate, the following spectra were taken

(a) The emission spectrum of the B.R.V. continuum source with 600 shots and the system completely evacuated. This gives the intensity of light incident on the absorbing gas column.

(b) The absorption spectrum of the radiofrequency discharge in oxygen using the same number of shots and the same set of anode and cathode for the BRV cource. This gives the intensity of light transmitted through the absorbing gas column.

The first exposure was in fact taken in two stages. Firstly, 300 shots of the BRV source were recorded. Then the tube was filled with oxygen, the discharge switched on and the absorption spectrum taken with 600 shots. Finally, the apparatus was re-evacuated, the plate racked back to its original position and the final 300 shots of the source recorded. This procedure was followed to diminish the errors introduced by any systematic change in the intensity distribution of the radiation produced by one shot of the source as electrode wear progressed. It was believed, that since the plate racking mechanism on the Jobin Yvon vacuum spectrograph was very well engineered, the errors introduced by sideways movement of the plate during racking in the vertical direction, were likely to be small enough to achieve an overall reduction in error.

On completion of the first two exposures, the BRV source anode and cathode were replaced and five calibration exposures taken with a completely evacuated system using 700, 500, 400, 200 and 75 shots. All of these, again, were built up progressively in stages to reduce any effects of electrode wear. The reader should note that it is not necessary to assume that I (1 shot) for the first set of electrodes is equal to I (1 shot) for the second set used for plate calibration.

With the Kodak 101-01 35 mm film, the two rails of polystyrene beads embedded in and protruding from the gelatin (which are placed along both edges of the film so that successive layers are prevented from touching when the film is rolled) reduced the available image space to 28 mm. The problem arose, therefore, that there was not enough space physically on each plate to accommodate all the spectra that had to be taken. With the 2400 lines per mm concave diffraction grating fitted to the vacuum spectrograph, the wavelength range from 1350 Å down to zeroth order was visible on the plate. The plate holder was thus modified so that the section of film corresponding in position to the unwanted spectral region from 1350 Å to 830 Å was masked and remained unexposed when spectra were taken. This permitted the film to be taken out, rotated 180° about an axis perpendicular to the plane of the film face and reloaded half way through the experiment, doubling the number of exposures that could be recorded on one piece of film.

It was important when obtaining the data to arrange as far as possible that the exposures lay on the linear part of the response curve of the photographic emulsion. In practice, the plate density tended to lie in the linear region of the response curve when recording $I(o)$ at wavelengths near the grating blaze and in the lower section of the response curve for $I(\Omega)$ away from blaze. Another problem was that a wavelength standard had to be set up for all of the exposures on the plate. The most convenient way of doing this was to record the O II emission from the radiofrequency discharge as described in Chapter III.

The procedure of taking a plate became quite a long one - the discharge emission had to be exposed for several minutes for the lines to be distinguishable after development and since the radiofrequency power could only be maintained (with the 100 cm tube) for 2 or 3 minutes before stopping and allowing the system to cool it took about 20 minutes to calibrate the spectrum. This had then to be repeated six times for each plate. Turning the film round half way through the run added another hour since the plate chamber of the vacuum spectrograph had to be raised to atmosphere pressure with cylinder nitrogen and then properly re-evacuated. Since the shape of the characteristic curve may change when the emulsion is evacuated (due to the removal of oxygen and water vapour) care was taken to ensure that the film was returned to its former conditions of vacuum.

The accuracy of the method of measuring $I_\gamma(\ell)/I_\gamma(o)$ by photographic photometry was tested by a run in which the following procedure was adopted. With the first set of BRV source electrodes, emission spectra of the continuum source were taken with a completely evacuated system using 600, 450 and 300 shots. The plate was then turned round, the source electrodes changed and calibration spectra taken with 800, 500, 400, 200 and 75 shots. The intensity ratios of the first three were then deduced at all wavelengths from the response curve and compared with the 'expected' ratios of 2:1.5:1. The results of the test run are discussed in the next chapter.

After development, the ratio of the transmitted to incident intensities of light exposed to the blackened emulsion (the transmissivity) was measured on a Joyce Loebl Mark III microdensitometer equipped with a scanning table powered by a stepping motor. Data was obtained therefore at discrete intervals along each spectrum and was output straight onto paper tape. The values for the seven scans for each plate could then be entered directly into computer data files. A response curve for the emulsion was constructed by performing a least squares polynomial fit to the calibration points using a computer program similar to that described in Appendix 2. The microdensitometer output for the five calibration spectra at any one wavelength were used as data points for this. On construction of the response curve, the intensity ratio $I(\ell)/I(o)$ at every point along the spectrum at which microdensitometer measurements were made (every 25 microns along the plate) was deducible.

No cross section measurements were attempted with the 30 cm long

10 cm diameter discharge tube since the molecular oxygen contamination of the spectra taken with this tube had been found to be appreciably greater.

CHAPTER VII

ATOMIC OXYGEN PHOTOABSORPTION CROSS SECTION RESULTS

7.1 Introduction

The relative photoabsorption cross section curves for atomic oxygen obtained in two experimental runs are given in Figures 7.1.1 to 7.1.3 (Run 1) and 7.1.4 to 7.1.6 (Run 2). These graphs constitute all of the data obtained in this investigation by the experimental procedure described in the previous chapter. On the graphs the values of

$$- \log_e I_\gamma(\ell)/I_\gamma(o)$$

are plotted against wavelength (and wavenumber) where $I_\gamma(\ell)$ is the intensity of light transmitted through the absorbing gas column and $I_\gamma(o)$ is the intensity of the incident light. Since

$$- \log_e I_\gamma(\ell)/I_\gamma(o) = \sigma_\gamma N \qquad (7.1.1)$$

these values are proportional to the photoabsorption cross section σ_γ , with the integrated number density of absorbing atoms N as the constant of proportionality. Increased absorption is denoted by the upward direction on the graphs. For comparison purposes, Figure 7.1.4 (Run 2) has been superimposed on Figure 7.1.1 (and displaced 0.15 up the ordinate for clarity). This constitutes the dashed curve.

The wavelength values were ascribed by measurement of the linear position of each element of blackened emulsion along the plate and interpolation between the O II emission from the radiofrequency discharge (listed in Appendix 1). The interpolation was achieved by performing a least squares polynomial fit to the standard wavelengths as described in Appendix 2. Since the intensity of the O II transitions was comparable on the spectra taken with and without oxygen in the absorption tube the value of $I_\gamma(\ell)/I_\gamma(o)$ appears to increase rapidly at the reference wavelengths producing a sharp dip in the cross section curve.

These can be readily identified on the graphs.

It can be seen from Figures 7.1.1 to 7.1.6 that the wavelength region from 830 Å to 430 Å is covered with absorption structure superimposed upon an underlying continuous absorption. The results from 830 Å to 650 Å, which overlap the region in which most of the absolute cross section data is available, are discussed in Section 7.2 of this chapter. Those below 650 Å, including the cross section data in the region of the new absorption series of atomic oxygen reported in Part I of this thesis are discussed in Section 7.3. Relative and absolute cross section values are compared in Section 7.4 and the final section of this chapter includes a discussion on the accuracy of results obtained by this experiment.

7.2 Results from 830 Å to 650 Å

The relative photoabsorption cross section values of atomic oxygen from 830 Å to 650 Å obtained in this experiment are given in Figures 7.1.1 (Run 1) and 7.1.5 (Run 2). Table 7.2.1 contains a list of the principal features on the curve of Figure 7.1.5.

Seven allowed Rydberg series of atomic oxygen were observed in this wavelength region by Huffman, Larrabee and Tanaka (4). Four converge to the ${}^2D^o$ limit (731.8 Å) of O II and three converge to the ${}^2P^o$ limit (665.3 Å). The lower members of these series can be distinguished on the cross section curves and correspond closely in wavelength with the values given in reference 4. (See Table 7.2.1). With reference to Figure 7.1.5 and Table 7.2.1, $4s'\ {}^3D^o$, $3d'\ {}^3S^o\ {}^3D^o$, $4d'\ {}^3S^o\ {}^3D^o$ and $5d'\ 6d'\ 8d'\ {}^3S^o\ {}^3P^o\ {}^3D^o$ were all observed in absorption. Emission from the upper state terms $3d'\ {}^3P^o$ (812 Å), $2s2p^5\ {}^3P^o$ (792 Å) and $4d'\ {}^3P^o$ (770.4 Å) occurred (as reported in reference 4) and produced an apparent dip in the cross section curve. Autoionization of these levels is forbidden in Russell-Saunders coupling.

FIGURE 7.1.1

RELATIVE ABSORPTION CROSS SECTION OF ATOMIC OXYGEN
(830 TO 430 A)

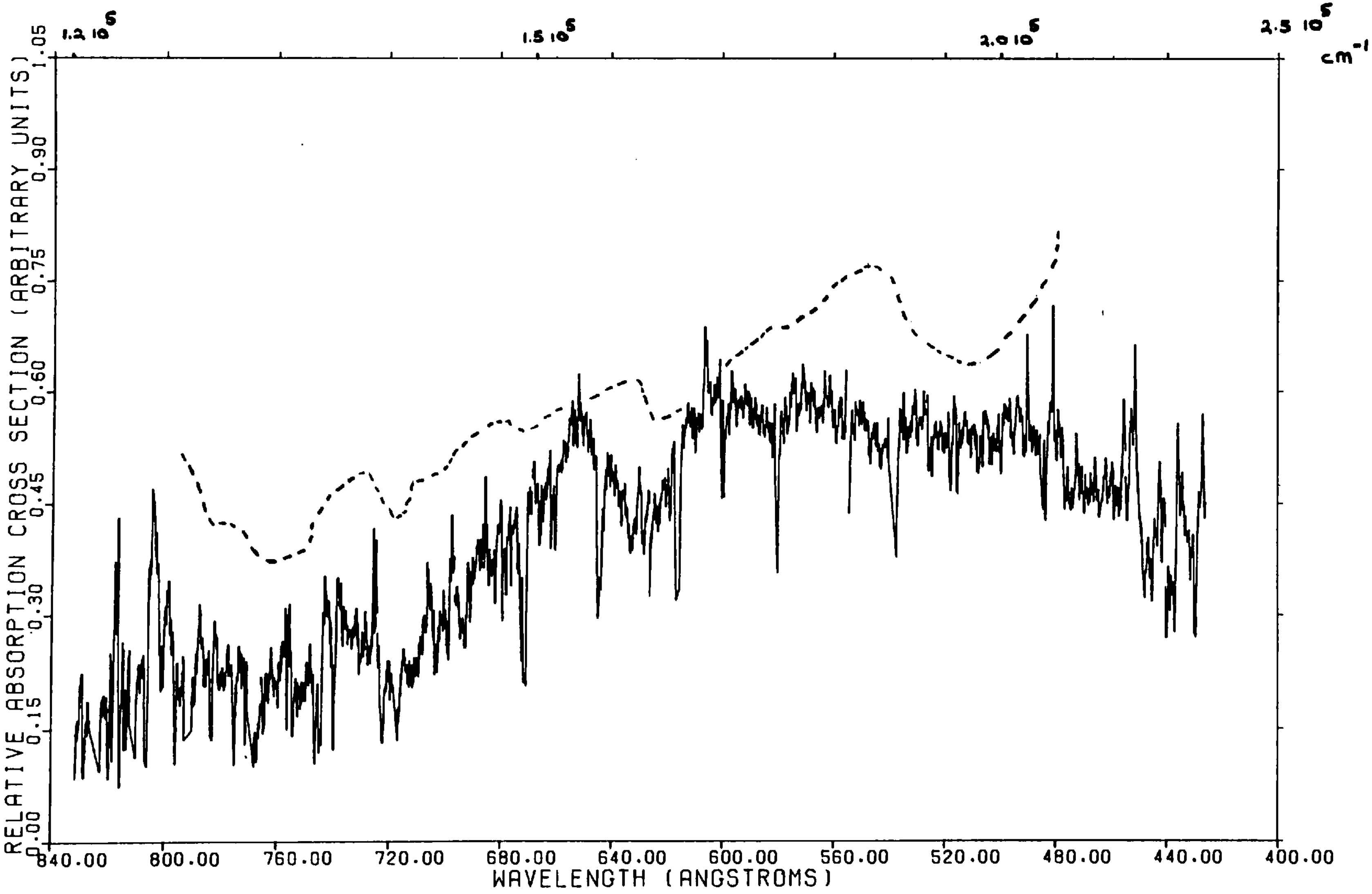

FIGURE 7.1.2

RELATIVE ABSORPTION CROSS SECTION OF ATOMIC OXYGEN
(650 TO 430 A)

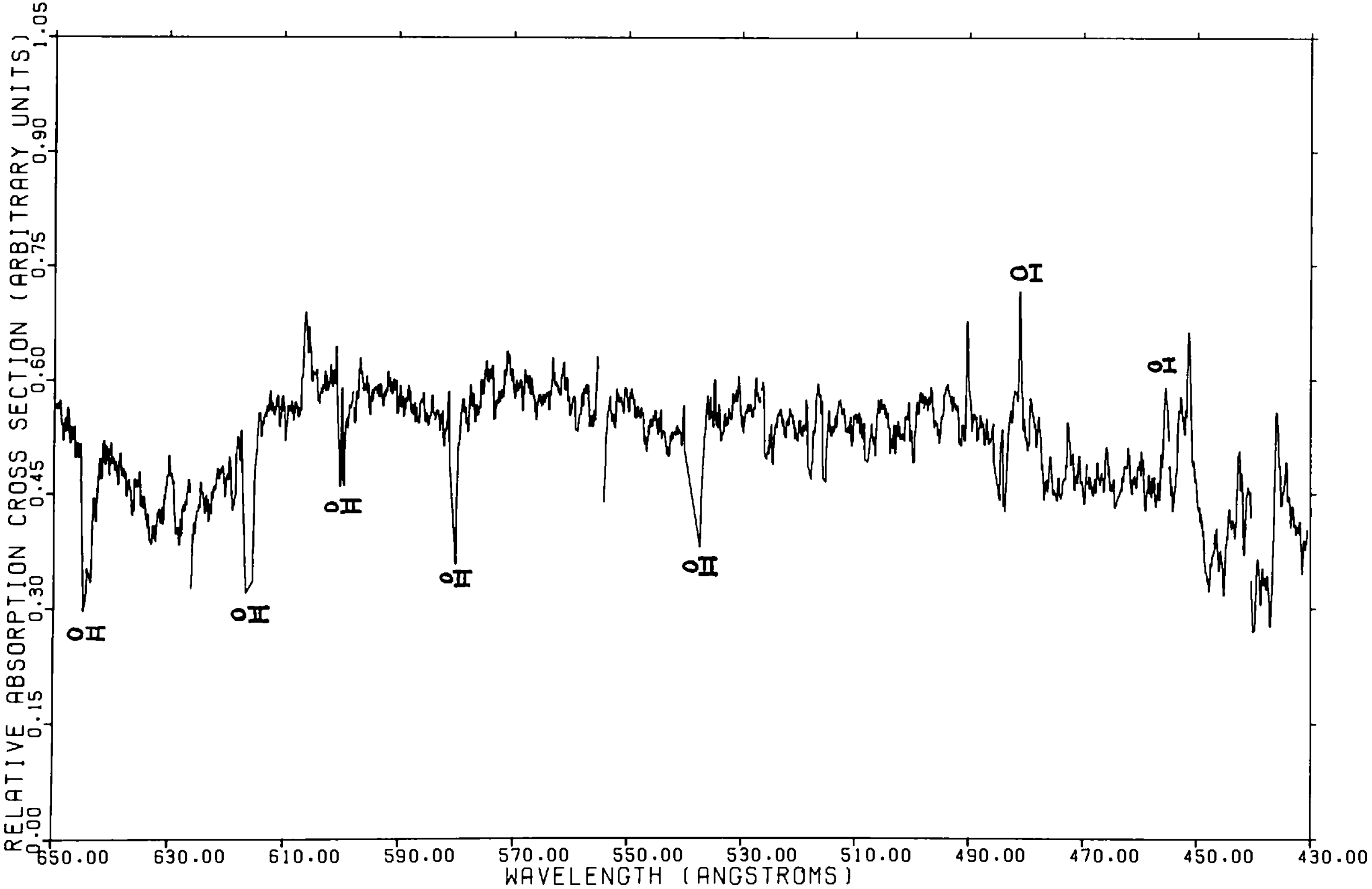

FIGURE 7.1.3

RELATIVE ABSORPTION CROSS SECTION OF ATOMIC OXYGEN
(485 TO 430 A)

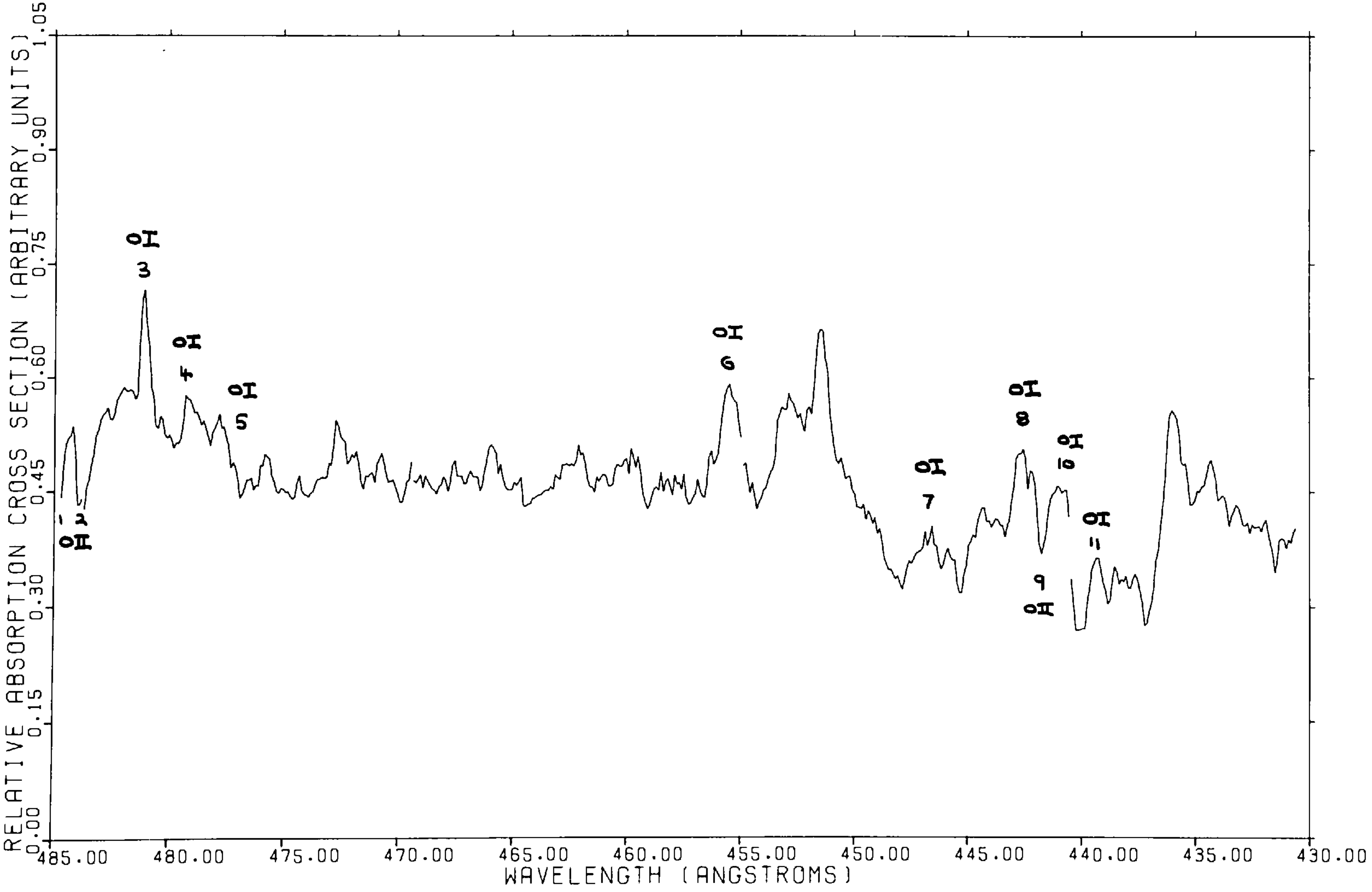

FIGURE 7.1.4

RELATIVE ABSORPTION CROSS SECTION OF ATOMIC OXYGEN
(830 TO 475 A)

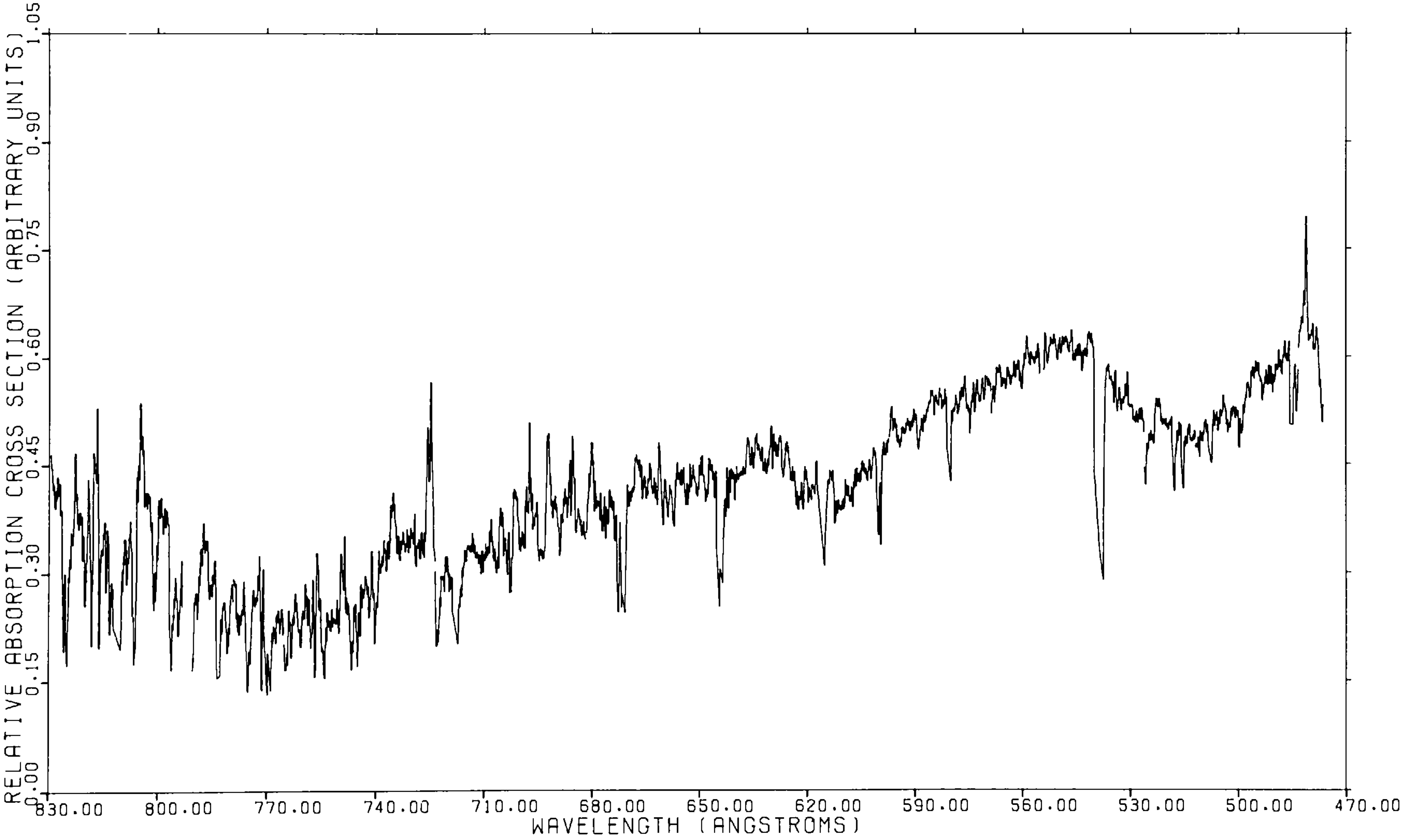

FIGURE 7.1.5

RELATIVE ABSORPTION CROSS SECTION OF ATOMIC OXYGEN
(830 TO 650 A)

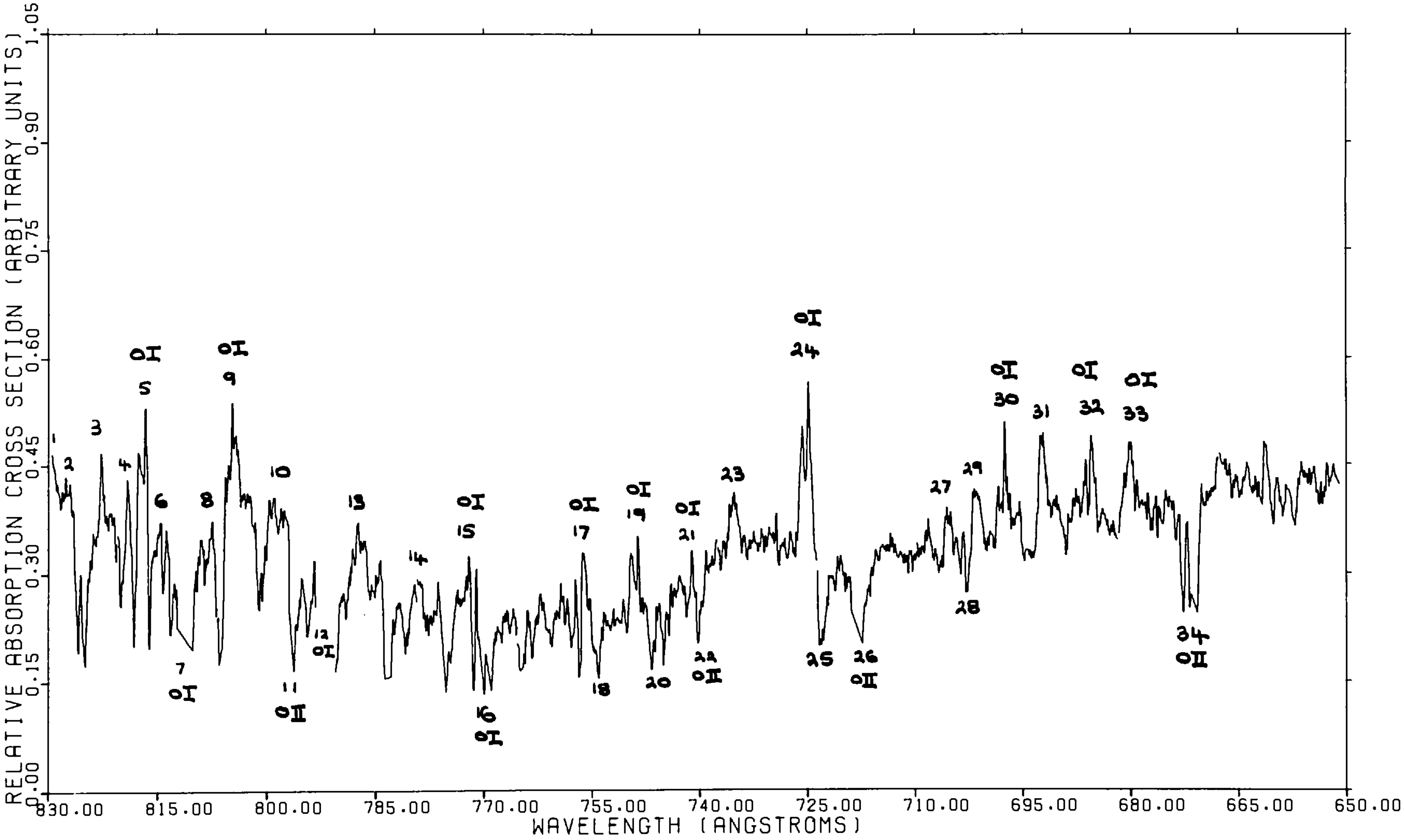

FIGURE 7.1.6

RELATIVE ABSORPTION CROSS SECTION OF ATOMIC OXYGEN
(650 TO 475 A)

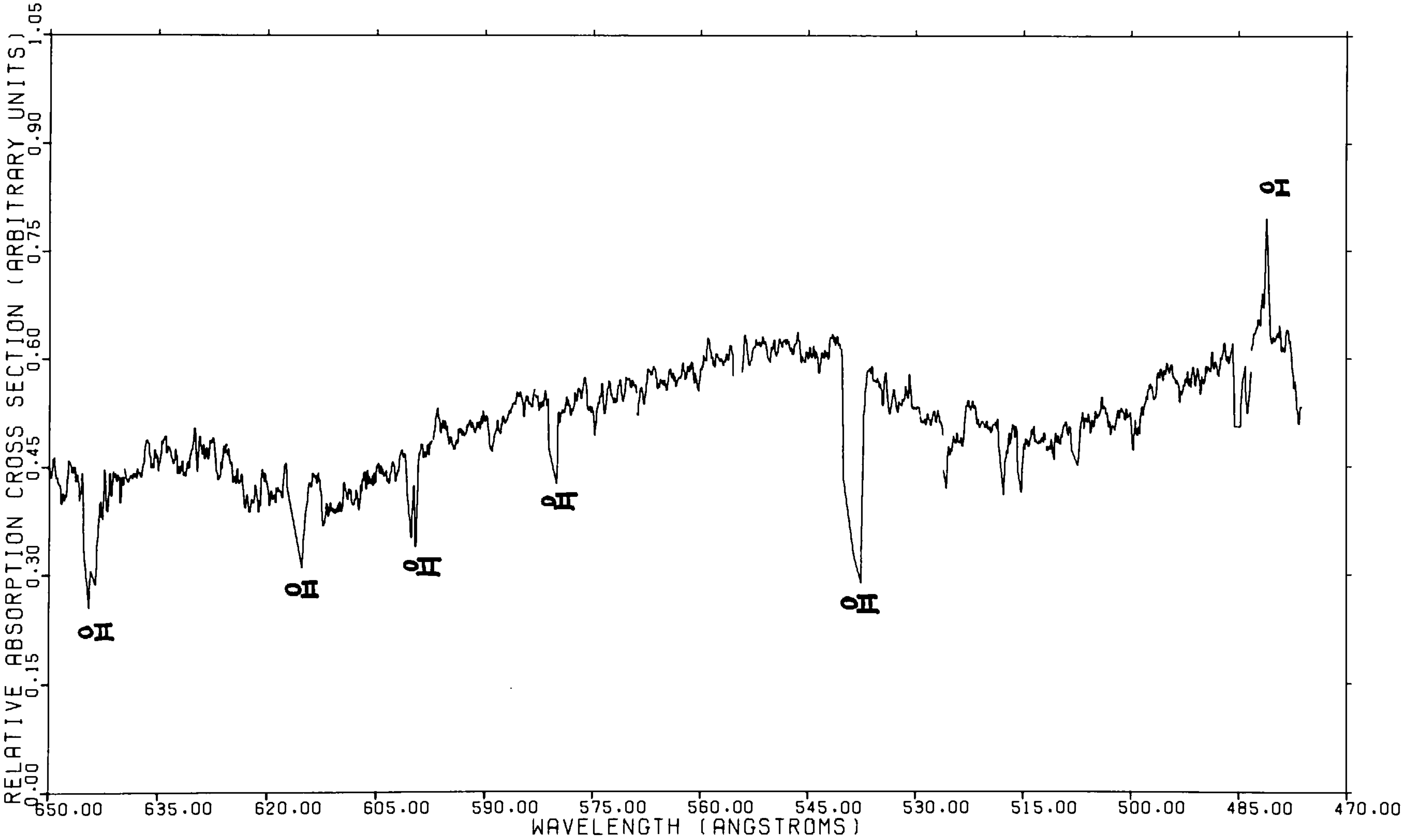

At shorter wavelengths the 3d", 4d", 5d" and 6d" configurations converging to the $^2P^o$ limit stand out very clearly (in absorption). The transitions from the lower levels J" = 2 and J" = 1 are resolved in all of these groups of series members. There is also indication of the 6s" $^3D^o$ term at 688 Å. The cross section falls below the level of continuous absorption on the short wavelength side of 3d" (feature 25 on Figure 7.1.5).

The general trend of continuous absorption is as follows. From 830 Å to 770 Å the cross section is static - perhaps showing a slight drop in value. It is difficult to be more precise than this because the curve is not at all smooth due to crowded superimposed structure. From 770 Å to 650 Å the cross section rises steadily. The value at 650 Å is approximately twice that at 770 Å. The rise is slightly steeper for the curve obtained on the first experimental run (Fig.7.1.1) than for the corresponding curve obtained on the second run (Figures 7.1.4 and 7.1.5). There is no sign on the curves of absorption edges at the $^2D^o$ (732 Å) and $^2P^o$ (665 Å) limits of O II. This can be explained by the fact that the absorption on the low energy side of the limits consists in part of transitions to excited bound states of the atom which tend to smear out the effect of the increased continuous absorption as the limits are traversed.

Photoabsorption cross sectional measurements for molecular oxygen in the wavelength region from 1060 to 580 Å have been reported by Huffman, Larrabee and Tanaka (31). The entire region is covered with numerous absorption bands superimposed upon an underlying continuous absorption. The continuous absorption rises from 10 Mbns to 30 Mbns from 830 Å to 800 Å probably due to the onset of a dissociation continuum(31). It is encouraging to note that the general increase is not observed on the curves from this experiment (Figures 7.1.1 and 7.1.5). The peaks

TABLE 7.2.1

A List of the Principal Features on the Cross Section Curve of Figure 7.1.5

Code	Wavelength (Å)	Remarks
1	829.7	O_2?
2	827.6	O_2?
3	822.8	O_2?
4	819.2	O_2?, O I $2p^4\ {}^1D_2$ to $({}^2P^o)3d''\ {}^1D^o_2$?
5	816.7	O I $({}^2D^o)\ 4s'\ {}^3D^o + O_2$?
6	814.6	?
7	812.1	O I $({}^2D^o)\ 3d'\ {}^3P^o$ (emission)
8	807.6	O_2?
9	804.8	O I $({}^2D^o)3d'\ {}^3S^o$, ${}^3D^o + O_2$?
10	799.1	O_2?
11	796.6	O II (emission)
12	792.0	$2s2p^5\ {}^3P^o$ (emission)
13	787.3	O_2?
14	778.8	O_2?
15	772.1	O I $({}^2D^o)\ 4d'\ {}^3S^o$, ${}^3D^o$
16	770.4	O I $({}^2D^o)4d'\ {}^3S^o$, ${}^3P^o$ (${}^3P^o$ in emission)
17	756.4	O I $({}^2D^o)5d'\ {}^3S^o$, ${}^3P^o$, ${}^3D^o$
18	754.2	?
19	748.7	O I $({}^2D^o)6d'\ {}^3S^o$, ${}^3P^o$, ${}^3D^o$

TABLE 7.2.1 (Continued)

Code	Wavelength (Å)	Remarks
20	747.1	?
21	741.2	0 I ($^2D^o$)8d' $^3S^o$, $^3P^o$, $^3D^o$
22	740.4	0 II (emission
23	735.3	0_2?
24	725.8	0 I ($^2P^o$)3d" $^3P^o$, $^3D^o$
25	723.5	?
26	718.6	0 II (emission)
27	705.6	0_2?
28	702.9	?
29	701.3	0_2?
30	697.5	0 I ($^2P^o$)4d" $^3P^o$, $^3D^o$
31	692.6	0_2?
32	685.6	0 I ($^2P^o$)5d" $^3P^o$, $^3D^o$
33	680.2	0 I ($^2P^o$)6d" $^3P^o$, $^3D^o$
34	672.9	0 II (emission)

on the cross section curve between 830 and 800 Å on Figure 7.1.5 are probably due, in part, to molecular oxygen band absorption (the molecular cross section rises to between 50 and 60 Mbns at these bands(31)). The cross section on Figure 7.1.5 is highest (from 830 to 800 Å) at 817 Å and 805 Å where there are both atomic oxygen transitions (4) and intense molecular bands (31). The molecular oxygen features which can be identified on Figure 7.1.5 are listed in Table 7.2.1. Emission from excited states of O II occurs at 797 Å, 740 Å, 719 Å and 673 Å.

7.3 Results from 650 Å to 430 Å

The relative photoabsorption cross section values of atomic oxygen below 650 Å which have been obtained by this experiment are given in Figures 7.1.2 (Run 1,650Å to 430 Å) and 7.1.6 (Run 2, 650 Å to 470 Å). It can be seen from the figures that the absorption from 650 Å to 490 Å is a much smoother continuous curve than in the higher wavelength region which was discussed in the previous section. From 490 Å to 430 Å absorption structure is again superimposed on underlying continua.

Table 7.3.1 gives a list of the principal features on Fig.7.1.3 which shows the cross section from 490 Å to 430 Å obtained in the first run. The observation of new absorption series of atomic oxygen has been reported in Part I of this thesis. With reference to Figure 7.1.3 it can be seen that most of the new transitions appear as structure on the cross section curve and correspond closely in wavelength to the values given in Chapter III. The $J'' = 1$ and $J'' = 2$ lines for the 3p $^3S^o$ term (479.6 Å) and the $^3D^o$, $^3S^o$ and $^3P^o$ terms for 4p to 8p are not resolved. The strong absorption feature between 455 and 450 Å and the rapid variation in the cross section at 437 Å are believed to be due to emission lines from the BRV source. The data at these points is therefore unreliable.

TABLE 7.3.1

A List of the Principal Features on the Cross Section Curve of Figure 7.1.3

Code	Wavelength (Å)	Remarks
1	485.086	O II emission
2	483.976	O II emission
	483.752	
3	481.3	O I $2s2p^4(^4P)3p\ ^3D^o$
4	479.6	O I $(^4P)3p\ ^3S^o$
5	477.6	O I $(^4P)3p\ ^3P^o$
6	455.9	O I $(^4P)4p\ ^3D^o,\ ^3S^o,\ ^3P^o$
7	447.1	O I $(^4P)5p\ ^3D^o,\ ^3S^o,\ ^3P^o$
8	443.1	O I $(^4P)6p\ ^3D^o,\ ^3S^o,\ ^3P^o$
9	442.048	O II emission
	442.001	
10	440.8	O I $(^4P)7p\ ^3D^o,\ ^3S^o,\ ^3P^o$
11	439.4	O I $(^4P)8p\ ^3D^o,\ ^3S^o,\ ^3P^o$

Below 650 Å, the continuous absorption rises with decreasing wavelength, reaching a peak at about 560 Å and then falls back slightly before the lower limit of these results at 430 Å. There is some variation between the data obtained in the two experimental runs (see Figure 7.1.1) as follows.

(a) In the first run the cross section rises to a peak at 650 Å. This is not observed in the second run.

(b) The cross section between 540 Å and 490 Å is almost constant for run one but decreases and rises again for run two.

The photoabsorption cross section of molecular oxygen has been measured in the 600 Å to 400 Å region by Watson, Lang and Stewart(12). The cross section falls from 28 Mbns at 600 Å to 20 Mbns at 590 Å and rises to 26 Mbns at 570 Å (due to the first member of the series $2s\sigma_u$ to $ns\sigma_g$ $(n \geqslant 3)$(11,12) which has a small negative value of the asymmetry factor q, defined by Fano (18). This variation does not occur on Figure 7.1.2 nor 7.1.6.

O II emission lines are prominent on the curves particularly in the region from 650 Å to 490 Å. They occur at 644 Å, 617 Å, 601 Å, 581 Å, 555 Å, 539 Å, 518 Å, 500 Å, 485 Å and 442 Å.

7.4 Comparison of relative and absolute cross section measurements

The relative photoabsorption cross section values obtained in the experiment have been compared with the absolute values of Cairns and Samson (1) (Table 7.4.1), Comes, Speier and Elzer (2) (Table 7.4.2) and Kohl, Lafyatis, Palenius and Parkinson (3) (Table 7.4.3). In Tables 7.4.1 to 7.4.3 the absolute values from references 1 to 3 are reproduced together with the values of

$$-\log_e \frac{I_\gamma(\ell)}{I_\gamma(o)}$$

from this investigation at the corresponding wavelengths, and their ratio. The mean values of the ratios can be used to give the absolute values corresponding to the vertical scales on Figures 7.1.1 to 7.1.6. These are shown in Tables 7.4.4 and 7.4.5. The ±7% uncertainty limits on the results of Kohl et al. (3) fall within the ±30% uncertainties of Cairns and Samson (1) but the values of Comes, Speier and Elzer (2) (± 10%) are about a factor of two lower. The results from reference 2 were not therefore used in the calculation of the mean ratio.

The standard deviation of the ratio values provide an indication of how closely the current measurements fit each set of absolute data. For the Cairns and Samson results the mean ratios are 36.3 (Run 1) and 32.0 (Run 2) and the standard deviations of the ratios are 11.5 (Run 1) and 8.2 (Run 2). The corresponding values for the Comes, Speier and Elzer measurements are 15.2, 16.3 (means for Runs 1 and 2 respectively), and 2.5, 4.7 (standard deviations for Runs 1 and 2 respectively). The fit for Run 1 against the data from reference 2 (s.d. 16% of the mean) is better than in the other cases (s.d's 26% to 32% of the means). The result at 717 Å from reference 2 was discarded in the calculations because of the close proximity of an O II emission line.

7.5 The accuracy of the results

The accuracy of the photoabsorption cross section results which have been presented in this chapter depends on the following:

(a) The error introduced by the presence of species apart from ground state atomic oxygen in the discharge tube.

(b) The error associated with the measurement of the ratio of the intensity of light incident on the absorbing gas column to the intensity of light transmitted through it.

TABLE 7.4.1

A Comparison of Relative and Absolute Cross Section Measurements - Cairns and Samson

Wavelength (Å)	Absolute Cross Section measured by Cairns & Samson (10^{-18} cm^2)	Relative values from the present work		Ratios	
		(Run 1)	(Run 2)	(Run 1)	(Run 2)
822.2	6.0	0.166	0.377	36.1	15.9
779.9	11.1	0.293	0.270	37.9	41.1
774.5	7.6	0.218	0.195	34.9	39.0
760.2	8.3	0.202	0.238	41.1	34.9
743.7	7.6	0.303	0.278	25.1	27.4
735.9	14.3	0.296	0.394	48.3	36.3
725.5	16.7	0.275	0.440	60.7	38.0
715.6	12.2	0.228	0.320	53.5	38.1
702.9	13.0	0.262	0.272	49.6	47.8
700.3	12.7	0.318	0.348	39.9	36.5
685.5	17.3	0.402	0.482	43.0	35.9
683.3	11.8	0.362	0.365	32.6	32.3
637.3	13.7	0.456	0.438	30.0	31.3
625.1	13.0	0.428	0.455	30.8	28.6
585.8	12.3	0.572	0.543	22.0	22.7
584.3	11.9	0.572	0.541	20.8	22.0
551.4	13.2	0.577	0.630	22.9	21.0
508.6	13.3	0.537	0.504	24.8	26.4

TABLE 7.4.2

A Comparison of Relative and Absolute Cross Section Measurements - Comes, Speier and Elzer

Wavelength (Å)	Absolute Cross Section measured by Comes, Speier and Elzer (10^{-18} cm^2)	Relative values from the present work		Ratios	
		(Run 1)	(Run 2)	(Run 1)	(Run 2)
790	2.1	0.219	0.239	9.6	8.8
777	2.5	0.233	0.234	10.7	10.7
765	2.3	0.128	0.164	17.6	13.7
717	4.8	0.155	0.257	30.7	18.5
705	4.2	0.338	0.369	12.4	11.4
702	4.8	0.265	0.410	17.9	11.6
657	7.1	0.501	0.386	14.2	18.4
642	8.3	0.491	0.390	16.9	21.3
622	8.1	0.456	0.402	17.8	20.2
615	8.5	0.489	0.360	17.4	23.6
609	9.9	0.566	0.405	17.5	24.4
597	9.1	0.590	0.499	15.4	18.2
585	9.1	0.550	0.544	16.6	16.7
552	9.5	0.588	0.618	16.2	15.4
536	9.2	0.555	0.568	16.6	16.2
507	9.0	0.527	0.510	17.0	17.7
487	7.8	0.549	0.622	14.2	12.6
471	6.7	0.463	-	14.5	-
462	7	0.498	-	14.1	-
450	5.5	0.452	-	12.2	-

TABLE 7.4.3

A Comparison of Relative and Absolute Cross Section Measurements - Kohl, Lafyatis, Palenius and Parkinson

Wavelength (Å)	Absolute cross Section measured by Kohl, Lafyatis, Palenius and Parkinson (10^{-18} cm^2)	Relative values from the present work (Run 1)	Relative values from the present work (Run 2)	Ratios (Run 1)	Ratios (Run 2)
780	4.86	0.226	0.253	21.5	19.2
765	5.30	0.128	0.168	41.4	31.6

TABLE 7.4.4

Absolute Values for the Cross Section Graph Scales

Figures 7.1.1, 7.1.2 and 7.1.3 (Mbns)

Scale Values	Cairns & Samson I	Comes et al. II	Kohl et al. III	I and III Combined
0.15	5.5	2.3	4.7	5.4
0.30	10.9	4.6	9.4	10.8
0.45	16.3	6.8	14.2	16.1
0.60	21.8	9.1	18.9	21.5
0.75	27.2	11.4	23.6	26.9
0.90	32.7	13.7	28.3	32.2
1.05	38.1	16.0	33.0	37.6

TABLE 7.4.5

Absolute Values for the Cross Section Graph Scales

Figures 7.1.4, 7.1.5 and 7.1.6 (Mbns)

Scale Values	Cairns & Samson I	Comes et al. II	Kohl et al. III	I and III Combined
0.15	4.8	2.5	3.8	4.7
0.30	9.6	4.9	7.6	9.4
0.45	14.4	7.3	11.4	14.1
0.60	19.1	9.8	15.2	18.8
0.75	23.9	12.2	19.1	23.5
0.90	28.7	14.7	22.9	28.2
1.05	33.5	17.1	26.7	32.9

(c) The uncertainty in the data which was used to place the results on an absolute scale.

Taking point (a) first, the most likely source of contamination is molecular oxygen either in the ground state or in excited states produced by the discharge. On visual inspection of the plates obtained in the experiments using the 100 cm discharge tube described in Section 2.2, it was encouraging to find that, although molecular absorption bands were not entirely absent, they were weak in comparison with atomic oxygen absorption lines. This point may be illustrated by reference to Plate 2.7.1. The member of the Rydberg series $O_2^+ \; b^4\Sigma_g^- \leftarrow O_2, X^3\Sigma_g^-$ at 705.3 Å has a cross section of 68 Mbns(31) (50% higher than the cross section of the continua upon which it is superimposed). It appears faintly on Plate 2.7.1, near the $4d'' \; {}^3D^o, {}^3P^o$ series member in atomic oxygen which is much more intense (see the cross section curve on Figure 7.1.5). The cross section curves described in Sections 7.2 and 7.3 were also found to be free of important molecular oxygen features.

Other species which might have been present are the metastable states of O I, $2p^4 \; {}^1D_2$ and $2p^4 \; {}^1S_0$. Seven absorption series with the lower level ${}^1D_2$ (5 converging to ${}^2D^o$ and 2 converging to ${}^2P$) and one with the lower level ${}^1S_0$ (converging to ${}^2P^o$) have been reported by Huffman, Larrabee and Tanaka(5) (see Table 1.2.2). Some of these transitions could be observed faintly on the absorption spectra taken in the course of these experiments (${}^1D_2$ to $({}^2P^o)3d'' \; {}^1D_2^o$ is a possible feature on the cross section curve of Figure 7.1.5 at 819.3 Å), although there is a molecular oxygen band at 819.8 Å (31). Since the intensity of the transitions which could be observed was low in comparison with the series from the ${}^3P$ ground state it is probable that the contribution of metastable states to the overall absorption is small.

Turning to point (b), the method of photographic photometry which was used to measure the intensity ratios is inherently a rather inaccurate one. However carefully the emulsion is calibrated, the sensitivity is not necessarily uniform over the whole plate. Furthermore, there are errors associated with the microdensitometer measurements and the construction of the response curve of the emulsion by a least square polynomial fit.

The effects of these sources of error were investigated by the following procedure. With one set of BRV source electrodes continuum spectra were taken (with an evacuated discharge tube) using 600, 450 and 300 shots. The plate was then calibrated and processed in the normal way. The intensity ratios of the three exposures were then deduced (at a number of wavelengths) from the response curve and compared with the expected ratios of 2:1.5:1. Results of the test run are presented in Table 7.5.1. The errors in the intensity ratios range from zero to 21%. The errors in the logarithm (to the base e) of the intensity ratios, however, are higher, in one case reaching 57% though the mean is 23%.

The test run can provide no information on the accuracy of the calibration of the emulsion (the reciprocity behaviour of the 101-01 film and the change in the intensity distribution of the radiation emitted by the source as electrode wear progresses are both uncertain). The total uncertainty in the results (i.e. associated with points (a), (b) and (c) of the first paragraph of this section) may be estimated from the fit of the current measurements to the absolute data (see previous section) and the error in the absolute data (30% for reference 1, 7% for reference 3). The total error is estimated at ± 50%.

TABLE 7.5.1

Results of the Test Run

Expected Intensity Ratio	Measured Intensity Ratio	Percentage error in the intensity Ratio	Percentage error in $\log_e$ of the intensity ratio
1.33	1.415	7	22
1.5	1.3	13	35
1.33	1.355	2	7
1.5	1.816	21	47
1.33	1.387	4	15
1.5	1.268	16	42
1.33	1.33	0	0
1.5	1.710	14	32
1.33	1.380	4	13
1.5	1.570	5	11
1.33	1.130	15	57
1.5	1.413	6	15
1.33	1.374	3	11
1.5	1.656	10	24
1.33	1.403	6	19
1.5	1.462	3	6
1.33	1.135	15	56
1.5	1.633	9	21
1.33	1.327	0	1
1.5	1.690	13	30
1.33	1.406	6	19
1.5	1.276	15	40
1.33	1.346	1	4
1.5	1.734	16	36

CHAPTER VIII

CONCLUSIONS AND SUGGESTIONS FOR FUTURE WORK

8.1 Conclusions

The absorption of extreme vacuum ultraviolet radiation by atomic oxygen has been investigated and the results presented in this thesis. The most important advantage of absorption spectroscopy is that energy levels which lie above the first ionization potential of the atom, and for which autoionization is allowed, can be observed. Emission from such levels is often difficult to record because of the relatively rapid depopulation of the upper state by autoionization.

The greatest difficulty in these experiments was found to be the creation of a pure sample of atomic oxygen of sufficient integrated number density and the containment of that sample in a windowless system. This difficulty was overcome by the use of a 2 to 7 MHz radiofrequency discharge through a 100 cm column of oxygen contained in a quartz tube equipped with a differential pumping section at both ends. No previous application of a similar radiofrequency discharge for the creation of atomic oxygen for absorption spectroscopy is known to the author. The differential pumping sections had to be designed with care in view of the high performance required of the first pumping stages. These experiments have employed the techniques developed in this laboratory over the design and use of the B.R.V. continuum source.

Table 8.1.1 lists the wavelengths (32,33) of important solar emission lines in the range 830 Å to 430 Å which have been measured in rocket and satellite experiments. None of the members of the three atomic oxygen absorption series converging to the ^4P term of O II which have been reported in this thesis correspond in wavelength with solar lines (the only line which comes within the range of the new series is the Ne VII transition at 465.2 Å which is nearest

$2s2p^4(^4P)4p\ ^3D^o$ at 455.9 Å). The photoabsorption cross section values obtained in this investigation at the wavelengths of the solar lines are also given in Table 8.1.1. The results of Section 7.4 were used to quote absolute values for the cross sections.

8.2 Suggestions for future work

The system for the creation and containment of atomic oxygen and atomic nitrogen which has been developed for these experiments could, in principle, be used to photograph the absorption spectra at wavelengths from 350 Å right down into the X-ray region. The short wavelength limit in this investigation was set by the rapid decline in the efficiency of the concave diffraction grating in the normal incidence mount. The dispersing instrument would have to be replaced with a spectrograph in which the grating is mounted at grazing incidence for an extension to lower wavelengths. The substitution of an electron synchrotron background continuum would facilitate the detection of weak line absorption spectra made difficult with the B.R.V. source by the many emission lines superimposed on the continuum below 350 Å. Some minor changes would be required to the discharge tube and the containment system before they could be attached to the synchrotron. Additional differential pumping stages would be needed to reduce the pressure to the ultra high vacuum at which the synchrotron operates. There would also need to be safeguards to protect the source if the vacuum should fail, for example on fracture of the quartz tube.

The proposal for an extension to shorter wavelengths can also be made for the photoabsorption cross section measurements (the lower wavelength limit here was 430 Å). In addition to this, investigation of the reciprocity behaviour of the Kodak 101-01 photographic emulsion for a pulsed light source (i.e. for exposures ranging from 10^{-6} sec to 10^{-3} sec) would determine whether reciprocity failure is a source

TABLE 8.1.1

Atomic Oxygen Photoabsorption Cross Section Values at important Solar Emission Lines

Wavelength (Å)	Identification	O I Cross Section(3) (Mbns)
790.2	O IV	6.0
790.1	O IV	7.1
787.7	O IV	10.4
786.5	S V	9.9
780.3(2)	Ne VIII	7.1
770.4	Ne VIII	- (4)
765.1(2)	N IV	4.9
761.1(1)	O V	7.3
629.7	O V	15.7
625.3(1)	Mg X	14.8
609.8	Mg X	15.7
599.6	O III	12.6
584.3(1)	He I	18.7
537.0	He I	17.7
521.0	Si XII	17.7
499.3	Si XII	18.0
465.2	Ne VII	16.3

1. Absolute value is available at this wavelength from reference 1.
2. Absolute value is available at this wavelength from reference 3.
3. Average value from Runs 1 and 2.
4. O I $2s^2\ 2p^3(^2D^o)\ 4d'\ ^3P^o$ observed in emission at this wavelength.

of error in the results of Part II of this thesis. The apparatus could also be used for the measurement of absolute photoabsorption cross sections. This would require the development of a technique to obtain the integrated number density of atomic oxygen and a full quantitative investigation on the contents of the discharge tube so that correction to the results could be made for absorption by molecular oxygen (both in the ground and excited states) and by atoms in the metastable $^1D_2$ and $^1S_0$ levels. For the most accurate cross section measurements the apparatus would have to be set up with dispersion of the radiation from the continuum source before entry into the discharge tube and the use of photomultipliers to determine the intensity ratios.

APPENDIX 1

O II emission lines on the spectra were used as wavelength standards in this investigation. The O II transitions are listed in Table A.1.1. All values were obtained from Reference (25).

TABLE A.1.1

O II Transitions used as Wavelength Standards

Wavelength (Å)	Lower State	Upper State
429.647	$2s^2\ 2p^3\ {}^4S^o_{3/2}$	$2s^2\ 2p^2(^3P)3d\ {}^4D_{5/2}$
430.041) 1.	${}^4S^o_{3/2}$	$2p^2(^3P)3d\ {}^4P_{3/2}$
430.177)	${}^4S^o_{3/2}$	${}^4P_{5/2}$
442.001) 1.	${}^2D^o_{5/2}$	$2p^2(^1D)3d\ {}^2D_{5/2}$
442.048)	${}^2D^o_{3/2}$	${}^2D_{3/2}$
445.601) 1.	${}^2D^o_{5/2}$	$2p^2(^1D)3d\ {}^2F_{7/2}$
445.638)	${}^2D^o_{3/2}$	${}^2F_{5/2}$
483.976	${}^2D^o_{5/2}$	$2p^2(^3P)3d\ {}^2P_{3/2}$
485.086	${}^2D^o_{5/2}$	$2p^2(^3P)3d\ {}^2F_{7/2}$
485.515	${}^2D^o_{3/2}$	${}^2F_{5/2}$
507.683 (2)	$2p^2\ {}^3P_1$	$2p^2\ {}^3S^o_1$
508.182 (2)	${}^3P_2$	${}^3S^o_1$
515.498	$2p^3\ {}^2P^o_{3/2}$	$2p^2(^3P)3d\ {}^2D_{5/2}$

(continued)

TABLE A.1.1 (Continued)

Wavelength	Lower State	Upper State
517.937	$2s^2\ 2p^3\ ^2P^o$	$2s^2\ 2p^2(^3P)3d\ ^2P_{1/2}$
518.242	$^2P^o$	$^2P_{3/2}$
537.830	$^2D^o_{3/2}$	$2s\ 2p^4\ ^2P_{1/2}$
538.256	$^2D^o_{5/2}$	$^2P_{3/2}$
539.086	$^4S^o_{3/2}$	$2p^2(^3P)3s\ ^4P_{5/2}$
539.547	$^4S^o_{3/2}$	$^4P_{3/2}$
539.853	$^4S^o_{3/2}$	$2p^2(^3P)3s\ ^4P_{1/2}$
555.056) 1.	$^2D^o_{5/2}$	$2p^2(^1D)3s\ ^2D_{5/2}$
555.121)	$^2D^o_{3/2}$	$^2D_{3/2}$
580.400	$^2P^o$	$2s\ 2p^4\ ^2P_{1/2}$
580.967	$^2P^o$	$^2P_{3/2}$
599.598 (2)	$2p^2\ ^1D_2$	$2p^3\ ^1D^o_2$
600.585	$^2P^o_{3/2}$	$2p^2(^1D)3s\ ^2D_{5/2}$
616.291	$^2D^o_{5/2}$	$2p^2(^3P)3s\ ^2P_{3/2}$
617.051	$^2D^o_{3/2}$	$^2P_{1/2}$

---

1. Grouped as one standard.
2. O III transition.

APPENDIX 2

WAVELENGTH INTERPOLATION

Let the function $f(x)$ describe the relationship between the linear position of a transition along a spectrograph plate x and the wavelength of the transition $y = f(x)$. Measurement of the positions of the standard wavelengths on the plate yields the numbers f_n which approximate the value of $f(x)$ at x_n, that is

$$f(x_n) = f_n + \varepsilon_n \qquad n = 1, \ldots, N \tag{A.2.1}$$

where the experimental errors ε_n are unknown. The problem then arises of how to recover $f(x)$ from the given approximate data f_n $n = 1, \ldots, N$. In this investigation this was accomplished by fitting the data with a function $F(x)$ taken to be a second order polynomial, that is

$$F(x) = C_0 + C_1 x + C_2 x^2 \tag{A.2.2}$$

where the coefficients C_i were chosen so as to minimize the sum of the squares of the deviations

$$d_n = f_n - F(x_n ; C_0 , C_1 , C_2) \tag{A.2.3}$$

that is to minimize

$$E(C_0,C_1,C_2) = \sum_{n=1}^{N} \left. f_n - F(x_n; C_0,C_1,C_2) \right.^{2} \tag{A.2.4}$$

This procedure leads to a linear system of equations for the determination of the C_i's. The resulting approximation is known as the least squares approximation to the given data.

On differentiating $E(C_0,C_1,C_2)$ with respect to the C_i we obtain

$$\frac{\partial}{\partial C_i} E(C_o,C_1,C_2) = \sum_{n=1}^{N} \frac{\partial}{\partial C_i}\left[f_n - F(x_n;C_o,C_1,C_2)\right]^2 \quad C_i = 0,1,2 \qquad (A.2.5)$$

$$= -2\sum_{n=1}^{N}\left[f_n - F(x_n;C_o,C_1,C_2)\right] \times \frac{\partial}{\partial C_i} F(x_n;C_o,C_1,C_2) \qquad (A.2.6)$$

Since $F(x_n;C_o,C_1,C_2)$ is a second order polynomial of the form given in Equation (A.2.2), we get

$$\frac{\partial}{\partial C_i} F(x_n;C_o,C_1,C_2) = \phi_i(x_n)$$

where $\phi_i(x_n) = 1 \quad i=0, \; =x \quad i=1, \; =x^2 \quad i=2.$ (A.2.7)

Using this in Equation (A.2.6) and setting the result to zero, we obtain

$$-2\sum_{n=1}^{N}\left[f_n - F(x_n;C_o^*,C_1^*,C_2^*)\right]\phi_i(x_n) = \frac{\partial}{\partial C_i} E(C_o,C_1,C_2) \quad C_i = C_i^* = 0 \qquad (A.2.8)$$

This system of equations is a necessary condition for C_i^* to minimize $E(C_o,C_1,C_2)$. The equations (A.2.8) are known as the normal equations of the least squares approximation.

On solution of the normal equations the wavelength values f_j of the unknown transitions are given by the values $F(x_j;C_o^*,C_1^*,C_2^*)$. The computer program which was used to perform the least squares fit also calculated the root mean square deviation after the C_i^* had been determined. If this was greater than a tolerance value specified in the input the deviations

$$f_n - F(x_n;\, C_o^*,\, C_1^*,\, C_2^*)$$

which were greater than a value also specified in the input were determined and the corresponding standard lines discarded from the data file. A new polynomial was then computed for the remaining set.

APPENDIX 3

Values of the Integrals $F^k(n_i\ell_i,n_j\ell_j)$ and $G^k(n_i\ell_i,n_j\ell_j)$ computed by the Froese-Fischer Program

TABLE A.3.1

O I ground state $1s^2\ 2s^2\ 2p^4$

$F^0(1s,1s) = 4.7413297$

$F^0(1s,2s) = 1.1353696$ $G^0(1s,2s) = 0.0774915$

$F^0(2s,2s) = 0.7987610$

$F^0(1s,2p) = 1.0946956$

$F^0(2s,2p) = 0.7723363$

$F^0(2p,2p) = 0.7511656$

$G^1(1s,2p) = 0.1049987$

$G^1(2s,2p) = 0.4707341$

$F^2(2p,2p) = 0.3338934$

TABLE A.3.2

O I configuration $1s^2\ 2s\ \ 2p^5$

$F^0(1s,1s) = 4.7357375$

$F^0(1s,2s) = 1.1497056$ $G^0(1s,2s) = 0.0809236$

$F^0(2s,2s) = 0.8096694$

$F^0(1s,2p) = 1.0894843$

$F^0(2s,2p) = 0.7745509$

$F^0(2p,2p) = 0.7457266$

$G^1(1s,2p) = 0.1050027$

$G^1(2s,2p) = 0.4703575$

$F^2(2p,2p) = 0.3304965$

TABLE A.3.3

O I configuration $1s^2\ 2s\ 2p^4\ 3p$

$F^0(1s,1s)$ = 4.7368405	
$F^0(1s,2s)$ = 1.1890610	$G^0(1s,2s)$ = 0.0869738
$F^0(2s,2s)$ = 0.8421653	
$F^0(1s,2p)$ = 1.1860378	
$F^0(2s,2p)$ = 0.8335423	
$F^0(2p,2p)$ = 0.8305969	
$F^0(1s,3p)$ = 0.1819183	
$F^0(2s,3p)$ = 0.1770142	
$F^0(2p,3p)$ = 0.1770108	$G^0(2p,3p)$ = 0.0041199
$F^0(3p,3p)$ = 0.1346334	
	$G^1(1s,2p)$ = 0.1259956
	$G^1(2s,2p)$ = 0.5103531
	$G^1(1s,3p)$ = 0.0019148
	$G^1(2s,3p)$ = 0.0037355
$F^2(2p,2p)$ = 0.3775125	
$F^2(2p,3p)$ = 0.0152804	$G^2(2p,3p)$ = 0.0039414
$F^2(3p,3p)$ = 0.0707350	

TABLE A.3.4

O I configuration $1s^2\ 2s\ 2p^4\ 4p$

$F^0(1s,1s)$ = 4.7369048	
$F^0(1s,2s)$ = 1.1895807	$G^0(1s,2s)$ = 0.0870548
$F^0(2s,2s)$ = 0.8425839	
$F^0(1s,2p)$ = 1.1861896	
$F^0(2s,2p)$ = 0.8337598	
$F^0(2p,2p)$ = 0.8306224	
$F^0(1s,4p)$ = 0.0883936	
$F^0(2s,4p)$ = 0.0867007	
$F^0(2p,4p)$ = 0.0866988	$G^0(2p,4p)$ = 0.0013773
$F^0(4p,4p)$ = 0.0595228	
	$G^1(1s,2p)$ = 0.1260633
	$G^1(2s,2p)$ = 0.5104386
	$G^1(1s,4p)$ = 0.0006649
	$G^1(2s,4p)$ = 0.0012545
$F^2(2p,2p)$ = 0.3774897	
$F^2(2p,4p)$ = 0.0045442	$G^2(2p,4p)$ = 0.0013462
$F^2(4p,4p)$ = 0.0308077	

TABLE A.3.5

O I configuration $1s^2\ 2s\ 2p^4\ 5p$

$F^0(1s,1s) = 4.7369229$

$F^0(1s,2s) = 1.1897258$

$G^0(1s,2s) = 0.0870774$

$F^0(2s,2s) = 0.8427012$

$F^0(1s,2p) = 1.1862473$

$F^0(2s,2p) = 0.8338303$

$F^0(2p,2p) = 0.8306487$

$F^0(1s,5p) = 0.0523751$

$F^0(2s,5p) = 0.0516024$

$F^0(2p,5p) = 0.516015$

$G^0(2p,5p) = 0.0006217$

$F^0(5p,5p) = 0.0339048$

$G^1(1s,2p) = 0.1260841$

$G^1(2s,2p) = 0.5104704$

$G^1(1s,5p) = 0.0003041$

$G^1(2s,5p) = 0.0005670$

$F^2(2p,2p) = 0.3774948$

$F^2(2p,5p) = 0.0019638$

$G^2(2p,5p) = 0.0006111$

$F^2(5p,5p) = 0.176262$

TABLE A.3.6

O I Configuration $1s^2\ 2s\ 2p^4\ 6p$

$F^0(1s, 1s) = 4.7369300$

$F^0(1s, 2s) = 1.1897817$

$G^0(1s, 2s) = 0.0870861$

$F^0(2s, 2s) = 0.8427464$

$F^0(1s, 2p) = 1.1862718$

$F^0(2s, 2p) = 0.8338589$

$F^0(2p, 2p) = 0.8306617$

$F^0(1s, 6p) = 0.0346490$

$F^0(2s, 6p) = 0.0342343$

$F^0(2p, 6p) = 0.0342338$

$G^0(2p, 6p) = 0.0003319$

$F^0(6p, 6p) = 0.0219568$

$G^1(1s, 2p) = 0.1260925$

$G^1(2s, 2p) = 0.5104839$

$G^1(1s, 6p) = 0.0001634$

$G^1(2s, 6p) = 0.0003029$

$F^2(2p, 2p) = 0.3774985$

$F^2(2p, 6p) = 0.0010267$

$G^2(2p, 6p) = 0.0003271$

$F^2(6p, 6p) = 0.0114667$

TABLE A.3.7

O I Configuration $1s^2\ 2s\ 2p^4\ 7p$

$F^0(1s, 1s) = 4.7369332$

$F^0(1s, 2s) = 1.1898076$

$F^0(2s, 2s) = 0.8427674$

$F^0(1s, 2p) = 1.1862838$

$F^0(2s, 2p) = 0.8338726$

$F^0(2p, 2p) = 0.8306684$

$F^0(1s, 7p) = 0.0246167$

$F^0(2s, 7p) = 0.0243691$

$F^0(2p, 7p) = 0.0243688$

$F^0(7p, 7p) = 0.0153953$

$F^2(2p, 2p) = 0.3775007$

$F^2(2p, 7p) = 0.0006041$

$F^2(7p, 7p) = 0.0080671$

$G^0(1s, 2s) = 0.0870901$

$G^0(2p, 7p) = 0.0001976$

$G^1(1s, 2p) = 0.1260965$

$G^1(2s, 2p) = 0.5104904$

$G^1(1s, 7p) = 0.0000976$

$G^1(2s, 7p) = 0.0001804$

$G^2(2p, 7p) = 0.0001950$

TABLE A.3.8

O I Configuration $1s^2\ 2s\ 2p^4\ 8p$

$F^0(1s, 1s)$ = 4.7369350

$F^0(1s, 2s)$ = 1.1898213

$G^0(1s, 2s)$ = 0.0870923

$F^0(2s, 2s)$ = 0.8427784

$F^0(1s, 2p)$ = 1.1862903

$F^0(2s, 2p)$ = 0.8338799

$F^0(2p, 2p)$ = 0.8306721

$F^0(1s, 8p)$ = 0.0183885

$F^0(2s, 8p)$ = 0.0182291

$F^0(2p, 8p)$ = 0.0182289

$G^0(2p, 8p)$ = 0.0001270

$F^0(8p, 8p)$ = 0.0113989

$G^1(1s, 2p)$ = 0.1260986

$G^1(2s, 2p)$ = 0.5104940

$G^1(1s, 8p)$ = 0.0000629

$G^1(2s, 8p)$ = 0.0001160

$F^2(2p, 2p)$ = 0.3775019

$F^2(2p, 8p)$ = 0.0003854

$G^2(8p, 8p)$ = 0.0001254

$F^2(8p, 8p)$ = 0.0059873

TABLE A.3.9

O I Configuration $1s^2\ 2s\ 2p^4\ 9p$

$F^0(1s, 1s)$ = 4.7369360	
$F^0(1s, 2s)$ = 1.1898291	$G^0(1s, 2s)$ = 0.0870935
$F^0(2s, 2s)$ = 0.8427848	
$F^0(1s, 2p)$ = 1.1862941	
$F^0(2s, 2p)$ = 0.8338841	
$F^0(2p, 2p)$ = 0.8306743	
$F^0(1s, 9p)$ = 0.0142575	
$F^0(2s, 9p)$ = 0.0141489	
$F^0(2p, 9p)$ = 0.0141488	$G^0(2p, 9p)$ = 0.0000864
$F^0(9p, 9p)$ = 0.0087824	
	$G^1(1s, 2p)$ = 0.1260998
	$G^1(2s, 2p)$ = 0.5104960
	$G^1(1s, 9p)$ = 0.0000428
	$G^1(2s, 9p)$ = 0.0000789
$F^2(2p, 2p)$ = 0.3775027	
$F^2(2p, 9p)$ = 0.0002609	$G^2(2p, 9p)$ = 0.0000853
$F^2(9p, 9p)$ = 0.0046211	

TABLE A.3.10

O I Configuration $1s^2\ 2s\ 2p^4\ 10p$

$F^0(1s, 1s) = 4.7369366$

$F^0(1s, 2s) = 1.1898339$

$F^0(2s, 2s) = 0.8427887$

$F^0(1s, 2p) = 1.1862965$

$F^0(2s, 2p) = 0.8338867$

$F^0(2p, 2p) = 0.8306757$

$F^0(1s, 10p) = 0.0113774$

$F^0(2s, 10p) = 0.0113002$

$F^0(2p, 10p) = 0.0113001$

$F^0(10p, 10p) = 0.0069753$

$F^2(2p, 2p) = 0.3775032$

$F^2(2p, 10p) = 0.0001848$

$F^2(10p, 10p) = 0.0036751$

$G^0(1s, 2s) = 0.0870942$

$G^0(2p, 10p) = 0.0000614$

$G^1(1s, 2p) = 0.1261005$

$G^1(2s, 2p) = 0.5104973$

$G^1(1s, 10p) = 0.0000305$

$G^1(2s, 10p) = 0.0000561$

$G^2(2p, 10p) = 0.0000607$

APPENDIX 4

INPUT DATA FOR THE MULTICONFIGURATION HARTREE-FOCK PROGRAM

The data requirements for the Froese Fischer program are described in references 23 and 24. Values specified for the calculation on atomic oxygen are given in this appendix. The straightforward data (such as the principal and angular momentum quantum numbers for each electron) is omitted.

CARD 2 CONFIG. Identifying label for the configuration

$1s^2 2s^2 2p^4$, $1s^2 2s 2p^5$ or $1s^2 2s 2p^4 np$ $n = 3,\ldots,10$

WT The weight of the configuration

All cases	1

CARD 3

s	Estimated screening number for the electrons
1s	0.4
2s	1.50
2p	3.00
np	7.00

METH Method to be used for solving the differential equation

All cases	Method 1

ACC Accelerating factor for wavefunction

All cases	0.0

IND Indicator specifying type of initial estimate for wavefunction.

All cases	Screened hydrogenic function.

REFERENCES

1. R.B. CAIRNS and J.A.R. SAMSON, PHYSICAL REVIEW 139, A1403 (1965).
2. F.J. COMES, F. SPEIER and A. ELZER, Z.NATURFORSCH 23a, 125 (1968).
3. J.L. KOHL, G.P. LAFYATIS, H.P. PALENIUS and W.H. PARKINSON, preprint.
4. R.E. HUFFMAN, J.C. LARRABEE and Y. TANAKA, THE JOURNAL OF CHEMICAL PHYSICS 46, 2213 (1967).
5. R.E. HUFFMAN, J.C. LARRABEE and Y. TANAKA, THE JOURNAL OF CHEMICAL PHYSICS 47, 4462 (1967).
6. P.M. DEHMER, J. BERKOWITZ and W.A. CHUPKA, THE JOURNAL OF CHEMICAL PHYSICS 59, 5777 (1973).
7. J.A.R. SAMSON and V.E. PETROSKY, THE JOURNAL OF ELECTRON SPECTROSCOPY AND RELATED PHENOMENA 3, 461 (1974).
8. W. DEL BIANCO and E. BORIDY, NUCLEAR INSTRUMENTS AND METHODS 92, 111 (1971).
9. G. BALLOFFET, J. ROMAND and B. VODAR, C.R. ACAD. SCI. PARIS 252, 4139 (1961).
10. J.N. FOX and J.E.G. WHEATON, JOURNAL OF PHYSICS E: SCIENTIFIC INSTRUMENTS 6, 655 (1973).
11. K. CODLING and R.P. MADDEN, THE JOURNAL OF CHEMICAL PHYSICS 42, 3935 (1965).
12. W.S. WATSON, J. LANG and D.T. STEWART, PHYSICS LETTERS 44A, 293 (1973).
13. C.E. MOORE, 'ATOMIC ENERGY LEVELS', CIRCULAR OF THE NATIONAL BUREAU OF STANDARDS 467, VOLUME I, Pages 35-37 and 47-49 (1949).
14. K.B.S. ERIKSSON and H.B.S. ISBERG, ARKIV FOR FYSIK 24, 549 (1963).
15. K.B.S. ERIKSSON, ARKIV FOR FYSIK 30, 199 (1965).
16. 'RYDBERG INTERPOLATION TABLE', DEPARTMENTS OF PHYSICS AND ASTRONOMY, PRINCETON UNIVERSITY, (1934).
17. H.B.S. ISBERG, ARKIV FOR FYSIK 35, 495 (1967).

References (Continued)

18. U. FANO, PHYSICAL REVIEW 124, 1866 (1961).

19. U. FANO and J.W. COOPER, PHYSICAL REVIEW 137, A1364 (1965).

20. J.E.G. WHEATON, APPLIED OPTICS 3, 1247 (1964).

21. J.C. SLATER, 'QUANTUM THEORY OF ATOMIC STRUCTURE', VOLUME I, McGRAW-HILL, (1960) as follows:
    (a) SECTION 14-2.
    (b) SECTION 13-3.

22. J.C. SLATER, 'QUANTUM THEORY OF ATOMIC STRUCTURE', VOLUME II, McGRAW-HILL, (1960) as follows:
    (a) APPENDIX 21.
    (b) SECTION 17-7.

23. C. FROESE FISCHER, COMPUTER PHYSICS COMMUNICATIONS 1, 151 (1969).

24. C. FROESE FISCHER, COMPUTER PHYSICS COMMUNICATIONS 4, 107 (1972).

25. R.L. KELLY and L.J. PALUMBO, 'ATOMIC AND IONIC EMISSION LINES BELOW 2000 ANGSTROMS - HYDROGEN THROUGH KRYPTON', Pages 47-48, (1973).

26. P.K. CARROLL, R.E. HUFFMAN, J.C. LARRABEE and Y. TANAKA, ASTROPHYSICS JOURNAL 146, 553 (1966).

27. R.E. HUFFMAN, Y. TANAKA and J.C. LARRABEE, THE JOURNAL OF CHEMICAL PHYSICS 39, 910 (1963).

28. J.J. HOPFIELD, PHYSICAL REVIEW 36, 789 (1930).

29. K. CODLING, ASTROPHYSICS JOURNAL 143, 552 (1965).

30. W.M. BURTON, A.T. HATTER and A. RIDGELEY, APPLIED OPTICS 12, 1851 (1973).

31. R.E. HUFFMAN, J.C. LARRABEE and Y. TANAKA, THE JOURNAL OF CHEMICAL PHYSICS 40, 356 (1964).

32. H.E. HINTEREGGER, ANNALES DE GEOPHYSIQUE 26, 547 (1970).

33. R.E. HUFFMAN, CANADIAN JOURNAL OF CHEMISTRY 47, 1823 (1969).